Instabilities in non-linear wave systems in optics

Marin Soljačić

A DISSERTATION

PRESENTED TO THE FACULTY

OF PRINCETON UNIVERSITY

IN CANDIDACY FOR THE DEGREE

OF DOCTOR OF PHILOSOPHY

RECOMMENDED FOR ACCEPTANCE

BY THE DEPARTMENT OF PHYSICS

May 2000

ABSTRACT

When a very broad wave-packet propagates in non-linear media, small perturbations sometimes grow on top of such a beam, modulating its shape. These kinds of instabilities are very common for non-linear wave propagation. My research investigates non-linear wave systems in several physical systems, with one unifying theme: instabilities. All of these studies relate to universal phenomena that are not material-specific, but apply to many non-linear wave systems in nature, beyond optics and electromagnetism.

In the first two chapters, we present the first stable bright self-trapped beams in (2+1)D Kerr media, so called necklace beams. We study numerically stability of necklace beams with respect to noise. We follow up with an analytical study of the dynamics of necklace beams, and show how one can understand analytically, and control experimentally their radial dynamics. Building on our work on necklace beams, we propose necklace beams that carry angular momentum. We study their various properties including: the allowed angular velocities, the underlying centrifugal force, the slowing-down of angular velocity due to the increase of moment of inertia, etc. In addition, we propose the first self-trapped beams in optics that carry a non-integer per-photon angular momentum.

In a following chapter, we explore various kinds of non-linear instabilities to show theoretically that one can construct fractals in almost any solitonic system in nature. We demonstrate numerically the generation of statistical fractals in examples of typical physical systems in optics. Moreover, we demonstrate numerically how one can also use our principle to

generate exact fractals, which are extremely rare in nature. Finally, we also present experiments demonstrating our ideas.

In the last part of the dissertation, we demonstrate theoretically the existence of modulation instability in incoherent wave-systems in non-instantaneous non-linear materials. We study its properties analytically, and numerically. We show that, in contrast to the well-known modulation instabilities in all loss-less coherent wave systems, one needs to have non-linearity above a certain threshold in order to observe the instability. This threshold is specified by the degree of coherence of the incident waves. Finally, we show first experiments with incoherent modulation instability which confirm our theoretical predictions.

This dissertation is dedicated to all the victims of the military aggression against the Republic of Croatia (1991-1995).

ACKNOWLEDGEMENTS

First, I would like to thank my PhD advisor, Prof. Mordechai Segev for these years of exciting research, and for his invaluable guidance during my graduate study; he made my experience at Princeton everything I was hoping it would be, and even much more.

Second, I would like to especially thank Suzanne Sears for countless inspiring discussions, and numerous fun research projects we worked on together. Furthermore, I would like to express my gratitude for all the exciting conversations I had with my fellow graduate students: Ashvin Vishwanath, Ziad Musslimani, Song Lan, Charalambos Anastassiou, Ming Shih, and many others.

Next, I would like to thank all the incredible professors I met at Princeton; discussions with them contributed greatly to my understanding of physics. I would especially like to thank Prof. Frank Wilczek for all the stimulating discussions about physics. I would also like to thank Prof. Joe Giordmaine, Prof. Keren Bergman, Prof. Ken Stieglitz, Prof. Duncan Haldane, Prof. Peter Meyers, and many others. I am grateful to Prof. Curtis Callan for his useful advice and for taking the time to read my thesis.

Finally, I would like to thank my family and my friends for their support; without them, this dissertation would not be possible.

CONTENTS

LIST OF FIGURES

CHAPTER 1: INTRODUCTION

1.1. SOLITONS

In linear media, localized wavepackets typically spread as they propagate. However, in some non-linear materials, non-linearity can under proper conditions stop the spreading, and such wavepackets do not change their shapes at all as they propagate. These wavepackets are then called solitons. In 1834, a Scottish scientist John S. Russell observed a "rounded smooth and well defined heap of water" propagating in a narrow and shallow canal "without change of form or diminution of speed" [2]. This was the first scientifically documented observation of solitons in nature. Nevertheless, solitons are quite general non-linear phenomena, and they have so far been described on surface of black holes [3], plasma waves [4], sound waves in He^3 [4], etc.

1.2. OPTICAL SOLITONS

In optics, the best-studied solitons are temporal and spatial solitons. In temporal solitons, the linear spreading is in temporal domain (dispersion), while in spatial solitons, the spreading is in space (diffraction). If one launches a localized pulse into a linear fiber, after some propagation distance, the temporal width of the pulse is significantly larger than at the input. However, in some non-linear fibers, if the conditions are just right, the non-linearity can stop the dispersion, and the pulse propagates without changing its shape. Such temporal solitons are considered as a main candidate for the next generation optical fiber communications. In spatial solitons, the beams are not localized in time; instead, it is their linear diffraction that is balanced by the non-linearity. High intensity light locally increases the index of refraction, and then this modulation in the index of refraction acts as a waveguide, guiding the beam that created the modulation itself. In quite a few cases this self-consistent self-trapping also turns out to be stable, and such a beam is called an "optical spatial soliton". If the self-trapping occurs both in a spatial, and in the temporal domain, such pulses are called spatio-temporal solitons.

1.3. OPTICAL SPATIAL SOLITON SPECIES

I briefly review various kinds of optical spatial solitons that have been demonstrated experimentally [5].

The first spatial soliton was suggested in nonlinear Kerr media in the 1960s [6]. In Kerr nonlinearities, the index change is given by $\Delta n = n_2 I$ where I is the local intensity, and n_2 is a real constant. Typical Δn's are of order of 10^{-4} or smaller. Soon after the theoretical prediction, it became clear that all bright solitons are unstable in bulk Kerr media [8]. Consequently, spatial Kerr solitons can be observed only in slab waveguides, and it wasn’t until the mid 1980s that such solitons were first observed [9]. Thus far, Kerr solitons have been observed in CS_2 [9], glass [10], semiconductor [11] and polymer waveguides [12]. All these experiments were performed in planar waveguides, which are inherently two-dimensional systems (one direction of propagation and one direction transverse to it in which the beam self-traps). In bulk (3D) media, although there are self-trapped solutions to the underlying equations, any perturbations of these solutions make the beam either shrink to a point or diffract to infinity [7].

Kerr non-linearity is only one of many different types of nonlinearities known today. As one increases the intensity, most nonlinearities include some form of saturation of the nonlinear change in the refractive index, Δn. An example that captures this physics is $\Delta n(I) = \Delta n_{sat}/[1+I/I_{sat}] = \Delta n_{sat} + n_2 I - n_3 I^2 + \ldots$, which is applicable, e.g., in a homogeneously broadened 2-level system. It turns out that this saturable nonlinearity supports stable self-trapping in bulk (3D) media. Although the term "soliton" was originally used only associated with a special class of so-called integrable systems, modern nomenclature now identifies all self-trapped beams as solitons [1]. In 1974 Bjorkholm and Ashkin demonstrated the first spatial solitons in bulk media [13], in the close vicinity of an electronic resonant transition of atomic (sodium) vapor. Very recently, bulk spatial solitons were also observed in semiconductor gain media [14] and polymers [15].

Another soliton species, appearing in photorefractive materials, was proposed in 1992 [16] and observed experimentally a year later [17]. Photorefractive materials exhibit great richness of non-linear phenomena, and many diverse nonlinear forms of the intensity-dependent index changes are observed [18]. For example, in the case of *screening solitons* [19-22], there are multiple physical effects involved. These include the liberation of carriers from traps by the absorption of a photon, the subsequent redistribution of these charges under the influence of internal and external fields, and finally, generation of self-trapping index changes in response to the local electric field via the electro-optic effect. Since there is always a limit to the number of carriers, nonlinearities supporting all photorefractive solitons are saturable and these solitons are stable in both slab waveguides [22] and in bulk media [18].

I also need to mention "quadratic solitons", consisting of multi-frequency waves coupled via a second order nonlinearity; these were predicted in the mid-1970s [23] and observed in the

1990s [24]. In these solitons, self-trapping occurs due to the rapid exchange of energy between the multi-frequency waves. This exchange keeps the powers and spatial widths of the two beams mutually stabilized. The net result effectively resembles a saturating nonlinearity and quadratic solitons are stable in both waveguides and bulk media [24]. The simplest example of quadratic solitons is second harmonic generation, for which there is a fundamental wave and a second harmonic wave. Both of these waves are locked together in space, propagating without diffraction. Quadratic solitons due to three wave interactions have also been demonstrated [25].

In all the cases so far described, the time-scale of the nonlinear response of the medium was not an important consideration. However, many nonlinearities are really non-instantaneous compared to the relevant time-scales of the system [26]. In some cases, the response to the time-dependence of a field can be extremely slow (e.g., photorefractive and thermal nonlinearities). In such media, incoherent solitons have been observed. A necessary prerequisite for incoherent solitons is that the medium responds only to the time-averaged intensity of the optical fields. Incoherent solitons are self-trapped wave-packets within which the phase varies randomly as a function of coordinates. In contrast, in coherent solitons the phase varies in unison with time everywhere on the beam. Incoherent solitons were first demonstrated in photorefractives, with monochromatic incoherent light [27]. Recently, they were also observed using incoherent white light (from an incandescent light bulb) [28].

1.4. OUTLINE OF THE THESIS

If a very broad beam propagates in a sufficiently highly non-linear media, small perturbations grow on top of the beam as the beam propagates; eventually, the beam disintegrates. These kinds of instabilities are very common in non-linear media; they are called

"Modulation Instabilities". During my PhD research, I was interested in the generic properties of such instabilities; my interest resulted in three separate, mutually related projects. In the first project, I was interested in suppressing these kinds of instabilities in order to create stable self-trapped beams (called necklace beams), in a media where they were previously thought not to exist. In another project, I was interested how such kind of instabilities can be used to create new, rich, fractal structures. Finally, I was also interested whether these kinds of instabilities can be observed in incoherent wave systems, that is, in weakly correlated many-particle systems.

In chapter 2, I present the first ever described stable self-trapped bright beams in (2+1)D Kerr media, so-called "necklace solitons" [8]. Next, I present analytical studies of various properties of necklace beams. I also show how one can control radial dynamics of necklace beams [29].

In chapter 3, I describe how one can add angular momentum to necklace beams that makes them a very interesting physical system to study [30]. Finally, I also demonstrate self-trapped necklace beams that carry angular momentum per-photon which is a non-integer multiple of $\hbar$. These are first such self-trapped beams in optics. The ideas presented in that chapter are not restricted to Kerr non-linearity, and are easily generalizable to other forms of non-linearities.

In chapter 4, I present a general principle that allows one to observe fractals in almost any soliton-supporting system in nature [31]. For definiteness, I concentrate my attention on a few examples of solitons typical in optics. In general, especially in the presence of significant noise, the process I describe results in random (statistical) fractals. In addition, I show that the principle I describe can also be used to generate exact (regular) fractals [32], which are extremely rare in nature.

In chapter 5, I demonstrate for the first time [33] modulation instability in systems of incoherent waves. Modulation instability is a very general and very well understood phenomena in non-linear systems of coherent waves. Modulation instability can be regarded as being a precursor of solitons. Thus, the observation of incoherent solitons [28] led us to believe that one should be able to observe modulation instability in non-linear systems of incoherent waves. This intuition proved to be correct. Incoherent modulation instability demonstrates some quite interesting new physical properties, and it conceptually bridges systems as far remote as gravitational instabilities with modulation instabilities of perfectly coherent light.

In chapter 6, I conclude, and discuss the avenues of further research.

CHAPTER 2: NECKLACE BEAMS

In this chapter, we present self-trapped bright "necklace"-ring beams that exhibit stable propagation for very large distances (> 50 diffraction lengths) in Kerr media (for an explanation of Kerr media, see section 1.3). Material presented in sections 2.1-2.5 appeared in [8], while the material presented in section 2.6 has been submitted to [29].

The necklace beams are ring-shaped beams whose intensities are azimuthally periodically modulated (in the form of "pearls"), and their widths are very narrow compared to their radia. A necklace beam is actually a ring array of (2+1)D quasi-solitons (pearls,) which we find to be stable for very large distances whenever the azimuthal period length of the ring is smaller or equal to the width of the ring. Computer simulations indicate that this necklace-ring is stable in the absolute sense, although we cannot prove this analytically. Preliminary experiments with self-trapped necklaces have already been reported [34]. The necklace-ring slowly expands, with a rate of expansion dependent on the number of "pearls" in the ring, the width of the ring, the initial peak intensity, and ring's diameter. When the number of "pearls" is large, holding the other parameters of each pearl fixed, the beams are almost fully stationary. In some cases, one can find approximate analytic solutions for necklace beams. The radial dynamics can be understood analytically, and controlled experimentally.

In section 2.1, we explain why necklace beams are potentially important. In section 2.2, we provide some physical intuition helpful for understanding physics of the system we study. In section 2.3, we describe necklace beams, and explain the intuition that led us to discovery of necklace beams. In section 2.4, we describe in detail the results of our numerical simulations of necklace beams. In section 2.5, we compare necklace beams with other similar creatures in non-linear optics. In section 2.6, we present detailed analytical study of necklace beams, and their radial dynamics; further, we describe a procedure that allows one to control the radial dynamics of necklace beams. We conclude this chapter in section 2.7.

2.1. MOTIVATION FOR NECKLACE BEAMS

Solitons in Kerr media are the most studied solitons in nature. The reason for that is two fold. First, the Kerr nonlinearity can be found in many systems: it represents a weak symmetric anaharmonicity, which is equivalent to a weak saturation in a simple harmonic oscillator model. For electromagnetic waves propagating in a weakly nonlinear centrosymmetric dielectric media, the Kerr nonlinearity manifests itself in the cubic NLSE, [6] which also describes the envelope of waves in plasmas, shallow water, deep water, gravity, etc [4]. The second reason is that Kerr solitons are mathematically elegant: the cubic NLSE is integrable in (1+1) dimensions. Its solitons can be found analytically and form a closed set; in their collisions, the total power and momentum in the solitons, and the number of solitons are always conserved [35]. The (2+1)D NLSE, although not integrable, has many conserved quantities, but, in the context of self-focusing, is haunted by stability problems [35]; (2+1) D bright Kerr solitons are unstable and undergo catastrophic collapse [7], and (1+1) D bright Kerr solitons in a 3D medium suffer from transverse instability [36]. These instabilities occur for solitons of all orders, including, e.g., the higher order self-trapped (2+1) D solutions [37]. In optics, bright Kerr solitons are observed only as temporal solitons [38], which are inherently (1+1) D, or as (1+1) D spatial solitons in single mode waveguides [10], for which transverse instability is eliminated by stringent boundary conditions. Thus interactions between bright solitons are restricted to planar systems.

Consequently, much of the beautiful similarity between solitons and particles is lost: e.g., angular momentum has no equivalent in the strictly planar system of bright solitons represented by the (1+1) D NLSE.

2.2. BACKGROUND AND INTUITION

The normalized cubic (2+1) D NLSE in cartesian coordinates is:

$$i\frac{\partial\psi}{\partial z}+\frac{1}{2}\left\{\frac{\partial^2\psi}{\partial x^2}+\frac{\partial^2\psi}{\partial y^2}\right\}+|\psi|^2\psi=0. \tag{2.2-1}$$

One might think that, since omitting the third term in Eq. (2.2-1) reduces it to the (1+1) D NLSE, the solutions should include all those of the (1+1) D NLSE in *x* and *z* that are uniform in *y*. However, such solitons are transversely unstable: large length-scale perturbations in *y* grow with propagation distance, and the soliton disintegrates [36]. In optical systems, this instability can be arrested by spatially modifying the refractive index so that *n(y)* provides waveguiding in the *y*, while the self-trapping occurs in *x* [10]. For this to work, the scale of waveguiding in *y* must be smaller (or equal) than the x-width of the soliton. In fact, the first experimental observation of optical spatial solitons [9] has employed an "effective waveguide", *n(y)*, that was self-induced (via Kerr nonlinearity) by the same beam that was a soliton in *x*. This works when the (1+1) D (*x* and *z*) soliton of Eq. (2.2-1) varies in *y* on a scale smaller than the "wavelength" of perturbations that make the comparable *y*-uniform soliton transversely unstable. The length scale of such perturbations is typically larger or equal to the *x*-width of the soliton. Therefore, periodic modulation in *y* superimposed on a soliton in *x*, arrests the transverse instability, provided that the *y*-period is smaller than the *x*-width of the soliton [9]. Experimentally, two equivalent sheets of light were superimposed, both were very long in *y* and perpendicular to *x*. The sheets propagated mostly along z, with a small angle to one another. The sheets interfered, producing a sinusoidal pattern in y, whose period was smaller than the x-width of each sheet. This superposition was launched into a self-focusing Kerr medium. At a high enough power, the beams evolved into a soliton (in x) while remaining transversely stable (in y.) However, as the two beams were not experimentally infinite in y, they eventually stopped overlapping and the system disintegrated.

2.3. OUR IDEA

Encouraged by Ref. [9], we take a (1+1)D soliton (x and z) whose intensity is periodically modulated in y, and wrap it around its own tail, hoping to find a stable (2+1)D ring array of quasi-solitons in a self-focusing Kerr medium. We start with Eq. (2.2-1) in cylindrical coordinates

$$i\frac{\partial\psi}{\partial z}+\frac{1}{2}\left\{\frac{\partial^2\psi}{\partial r^2}+\frac{1}{r}\frac{\partial\psi}{\partial r}+\frac{1}{r^2}\frac{\partial^2\psi}{\partial\theta^2}\right\}+|\psi|^2\psi=0\,. \tag{2.3-1}$$

Consider ring-like solutions whose ring thickness w is much smaller than the ring radius L, such as those in the first row of Fig. 2.3-1. In this case, the third term in Eq. (2.3-1) can be neglected since it is $O(w/L)$ smaller than the second term. Furthermore, since r varies negligibly over the ring thickness, $1/r^2$ can be replaced by $1/L^2$ in the fourth term. Redefining the variables as $x=r$ and $y=L\theta$ reduces Eq. (2.3-1) to Eq. (2.2-1). Consequently, if the intensity of the beam is periodically modulated in θ, the system looks much like the one in Ref. [9], apart for a small curvature. It is, therefore, reasonable to expect that such ring beams are stable. Physically, if the solitons from Ref. [9] are stable, we do not expect a small curvature to destabilize them; and, the experimental evidence from Ref. [9] certainly shows that these solitons without curvature are stable.

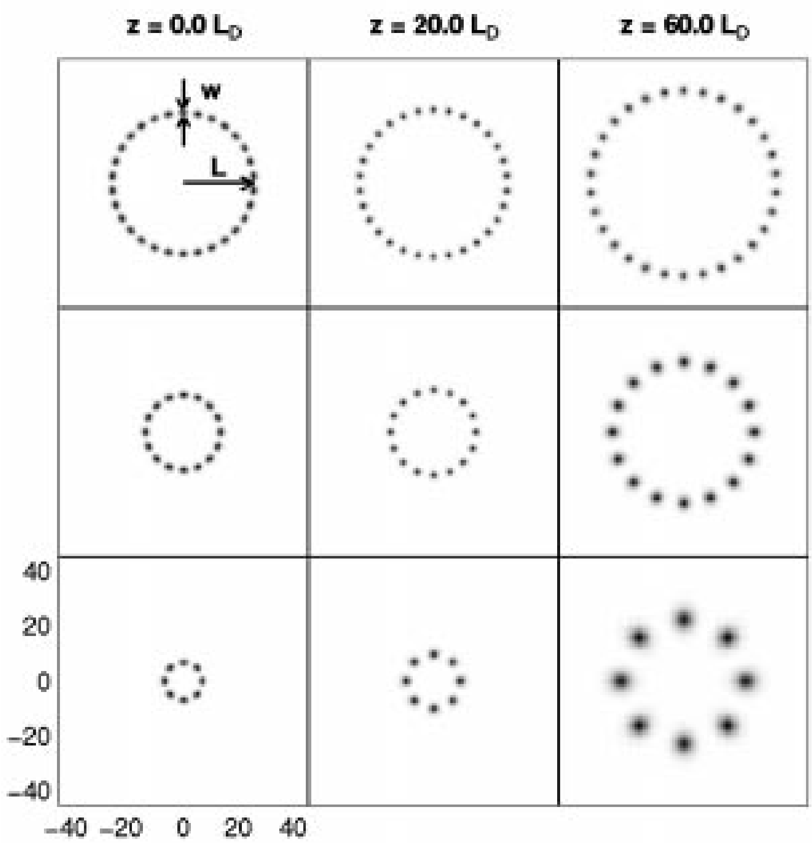

Figure 2.3-1: Examples of evolution of necklace-ring beams with Ω=15, Ω=8, and Ω=4 (first, second and third rows, respectively). In all cases the initial peak intensity is 1, w=1, and L/Ω=1.707. The axes are the same for all plots. Dark color indicates high intensity. In all figures in this thesis, contrast is enhanced for better clarity.

Led by the intuition gained from Ref. [9], we expect that the self-trapped shapes are close to $\alpha\, sech((r-L)/w)\, cos(\Omega\theta)$ for some α's, even as w's become comparable to the corresponding

L's. In this case the radius of our ring should slowly grow with propagation, because adjacent bright "spots" on the ring differ in phase by π, that is, neighboring "pearls" repel each other [1]. In a circularly symmetric ring the net force exerted on each "pearl" is radialy outwards, making the ring expand. However, if we increase L while holding w, α, and L/Ω constant, the net radial force vanishes. In the limit of vanishing curvature of the ring, the ring should not grow at all.

The expansion of the necklace-ring beam brings back the stability issue, because the propagation of the array of (1+1) D solitons in Ref. [9] is stationary, thus different than that of the necklace-ring. However, as we show below, the expanding necklace-ring seems to be stable. The intuitive reason for this is that, if $\psi(r,\theta,z)$ is a solution of Eq. (2.3-1), then $q\psi(qr,\theta,q^2z)$ is also a solution for any real q, and both solutions have exactly the same total power. As the radius of the ring slowly grows, there is always a stable shape reasonably close to the beam's instantaneous shape. If the distance needed for the beam to evolve into a stable shape is smaller than the rate of the expansion, our necklace-ring array of quasi-solitons has a good chance of being stable.

2.4. NUMERICAL SIMULATIONS OF NECKLACE BEAMS

We have simulated numerically (using standard Split Step beam propagation method) the propagation of necklace-ring beams and indeed all the above predictions seem correct. We have checked a large number of case-examples of necklace rings and propagated them over large distances. We find that all the examples with "pearls" of azimuthal width narrower than (or equal to) the radial-width of the ring, and radial width much smaller than ring radius, are stable. Within our computation capability, we find that they remain stable even under fairly large perturbations

(~ 5%) in the initial widths or powers, and at the presence of random noise (e.g., we have injected up to 1% of the total power of white noise in the Fourier space every diffraction length). Typical examples (for Ω = 15, 8, 4) are presented in Fig. 2.3-1, in which the initial shape is $\psi(r,\theta,z=0) = \alpha\ sech[(r-L)/w]\ cos(\Omega\theta)$, where $L>>w$, and $L/\Omega \approx w$. In the cases presented in Fig. 2.3-1, α =1, w=1 and L/Ω =1.707. As a measure for the propagation distance, we define the diffraction length, $L_D = 2\pi n w_0^2/\lambda$, where λ is the carrier wavelength in vacuum, n is the refractive index, and the minimum waist of a (2+1)D Gaussian beam of width 2 $w(z=0)$=2w_0. After a few L_D's, the initial shape evolves into a stable “necklace” of "pearls" which then slowly grows in size, via a uniform expansion (scaling) of the entire necklace-ring. As the necklace-ring beam expands uniformly, the peak intensities of the "pearls" drop roughly with $L^2(z)$. **Therefore, the total power within the necklace-ring beam is conserved and does not "escape" to radiation.** This necklace-ring of quasi-solitons remains stable for the propagation distances of ~100 diffraction lengths. In fact, the only thing that prevents us from stating that these necklace-ring beams are always stable (in the numerical sense), is the fact that, as the necklace-beams expand, they fill up our computational window and are affected by reflections from the window’s boundaries and cause some seemingly-artifacts of instability. Finally, we have tested the stability of these necklace beams under azimuthally-asymmetric variations in input conditions. We launched the input shapes of Fig. 2.3-1 but with a~2% ellipticity, and found that these imperfect rings exhibits stable self-trapping, yet they do not evolve into a circular shape. We conclude that, at least for small azimuthal perturbations, the necklace beam is stable, but its circular shape is not an “attractor”.

When we launch our necklace beams into a linear medium, they simply diffract within $O(1)$ L_D and the necklace structure is not preserved (e.g., see Fig. 2.4-1 for Ω=4). If we launch a single isolated (2+1) D beam with the same dimensions as one of the "pearls" in the necklace-ring, into this self-focusing Kerr medium, the isolated beam undergoes catastrophic collapse and disintegrates after *O(1)* L_D, as expected from a single (2+1)D bright beam propagating in Kerr media [7]. It is precisely the nonlinearity **and** the presence of the other peaks in our necklace-ring beam that keeps the whole configuration stable.

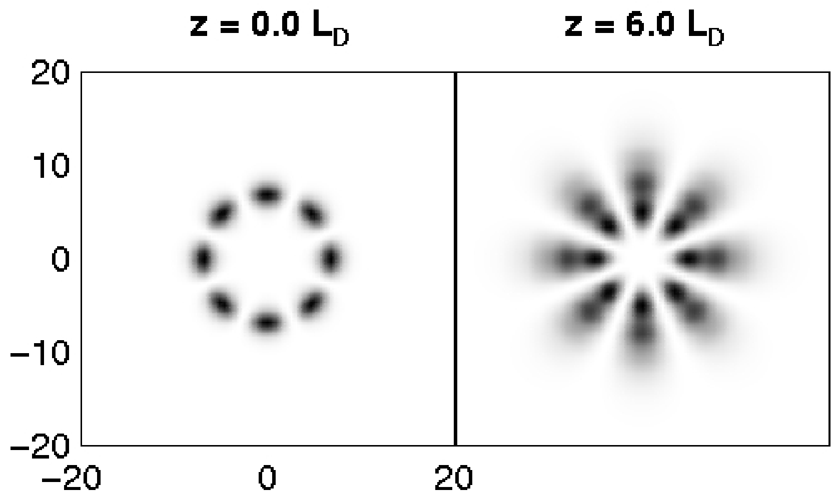

Figure 2.4-1: Evolution of the same initial shape as in the third row of Fig. 2.3-1, with nonlinearity set to zero. The beam diffracts within O(1 LD).

We now investigate the expansion dynamics of our necklace-ring beams. The rates of expansion are much slower for the rings of larger Ω than for the rings of smaller Ω, keeping *w*, L/Ω , and α constant. One might think that increasing Ω, while keeping *w* and *L* constant, would also decrease the expansion rate because the angle that determines the net radial component of the repulsion force gets smaller. But, this is not the case because the force between solitons of the cubic NLSE increase with increasing the gradient of the intensity (or decreasing distance between solitons). The final result is that decreasing Ω while keeping everything else constant typically slows down the ring growth. However, one can not fully stop the expansion by exploiting Ω's that are too low, since the transverse (azimuthal) instability occurs if $L/\Omega >> w$. The expansion dynamics of the relative radii of the necklace beams from Fig. 2.3-1 is shown in Fig. 2.4-2. In the beginning of the expansion there is a short period of acceleration, as the intensity peaks speed up in the radial direction. The acceleration diminishes once the "pearls" are far away from each other since the interaction forces decrease. Eventually, the adjacent peaks interact only very weakly, and the rate of the expansion becomes constant. Very similar features are observed in evolution of a ring of equally charged particles, thereby demonstrating again very picturesquely that solitons indeed behave like particles. Increasing Ω while holding w, L/Ω, and α fixed decreases the growth rate as predicted. As $\Omega \rightarrow \infty$, the beams become fully stationary.

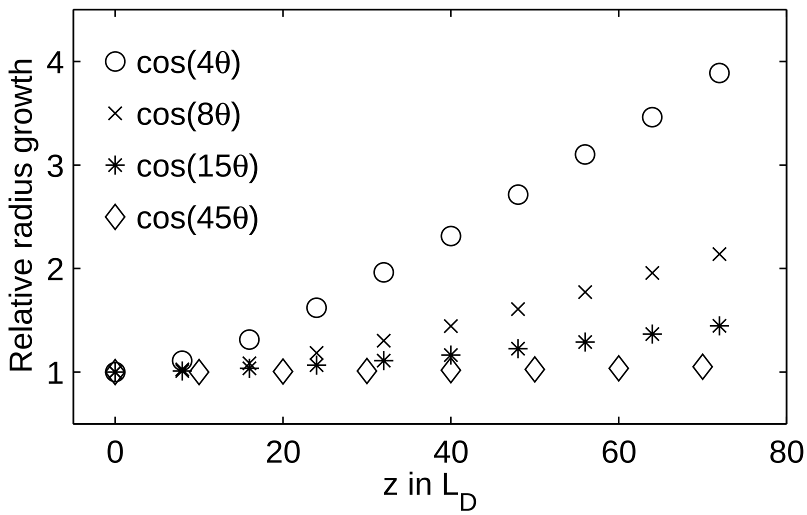

Figure 2.4-2: Growth of ratio (radius)/(initial radius), as a function of propagation distance. In all the cases the initial peak intensity is 1, w=1, and L/Ω=1.707. Holding these parameters fixed, a larger Ω implies slower dynamics.

To put things in a physical perspective, it is useful to note how our necklace-rings would look in a typical experiment. For λ = *500nm*, refractive index $n=1.5$, $w=10\lambda/n$, and $\Omega=45$, one finds $w=3.3\mu m$, $L=0.21mm$, and $60L_D=12.6mm$. Consequently, the necklace-ring solitons should be easily observable experimentally. Within $60L_D$, a necklace-beam with $\Omega=45$ will not change its shape or size almost at all. On the other hand, when the nonlinearity is "off" (or when the peak intensity is very low), the ring will undergo natural diffraction within several L_D's, say, 200 μm.

Because our necklace beams expand, it is not possible to find a stationary solution for them in the r,θ,z frame. However, in the limit $w\Omega/L << L/w$ and $L/\Omega << w$, one can find approximate stationary ring-like solutions to Eq. (2.3-1):

$$\psi(r,\theta,z) = e^{-i\Gamma z}\sum_{n=1}^{\infty}\sum_{m=1}^{\infty}\left\{\alpha_{n,m}\cos[(2n-1)\Omega\theta]\operatorname{sech}^{(2m-1)}[(r-L)/w]\right\}, \qquad (2.4\text{-}1)$$

with $\Gamma(w,L,\Omega)$, $\alpha_{n,m}(w,L,\Omega)$, Ω = integer, where $\alpha_{1,1}$ is of $O[(w\Omega/L)^2]$ larger than any other $\alpha_{n,m}$. In this limit, $\psi(r,\theta,z) \approx \alpha\, sech((r-L)/w)\, cos(\Omega\theta)\, e^{-i\Gamma z}$, with $\alpha^2=4/(3w^2)$, $\Gamma\approx(\Omega/L)^2$. The necklace beam becomes fully stationary as $L\rightarrow\infty$. We compare this solution to our simulations and find that indeed this analytic approximation is excellent. For example, in the case $w\Omega/L=10$ and $L\rightarrow\infty$, the difference between the lowest term in Eq. (2.4-1) and the true numerical self-trapped shape is only $O(1\%)$. This solution also applies to the periodically-modulated (1+1) D soliton stripe in Ref. [9] with r,θ replaced by $x,y/L$. We will have more to say about analytical studies of necklace beams in section 2.6.

One might think that as $w>>L/\Omega$, the beam might become transversely unstable in the radial direction. This does not happen because the intensity is just high enough to cause self-focusing on length scales of w, and not on any smaller scale.

2.5. PERSPECTIVE

It is now instructive to compare our soliton-like necklace beams to other (known) rings beams. As mentioned earlier, higher order (2+1) D solitons in this media are all unstable [37]. It is then interesting to study azimuthally-uniform rings. When $w<<L$, these rings are also transversely (azimuthally) unstable [40], as shown in Fig. 2.5-1. This is expected since the azimuthal length scale is much larger than the thickness of the ring; the instability is of the same origin as in the case of a soliton which is uniform in the y direction. When $w\sim L$ we find (numerically) that uniform rings tend to coalesce (rather than disintegrate) and eventually undergo catastrophic collapse as (2+1) D bright Kerr solitons do. One can also superimpose some radial "velocity" on a bright ring beam [39], which can provide some control over the rate

of the inherent tendency to shrink and collapse, and also convert the dynamics to expansion. In some specific cases the expansion dynamics of such ring can last up to several diffraction lengths before becoming unstable [39].

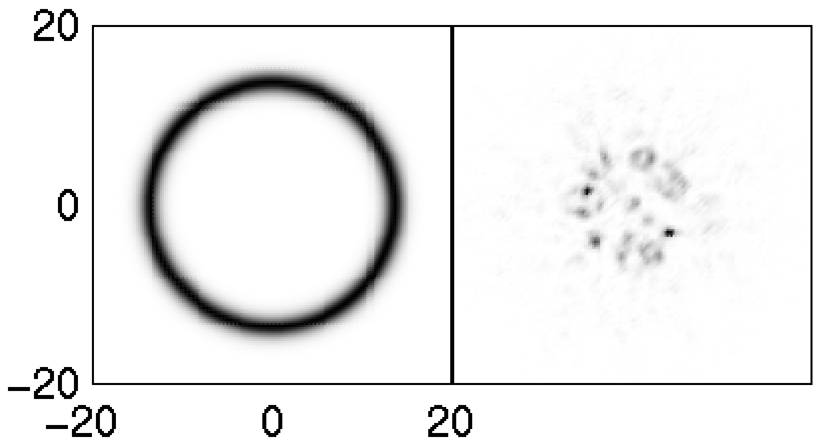

Figure 2.5-1: Propagation of an initially azimuthally-uniform ring beam (with L=13.7, *w*=1, and initial peak intensity of 1) in Kerr media. In this media, the background **numerical noise (only)** destabilizes the ring, and it eventually disintegrates. (a) the initial shape, (b) the shape after $z = 24$ L_D.

Another possibility to seek stable self-trapped ring beams is to multiply an intensity-uniform ring by $e^{i\Omega\theta}$ [instead of $cos(\Omega\theta)$, as we did]. These vortex-rings carry angular momentum [41], in contrast to our necklace-ring beam which is a coherent superposition of two vortex-rings with equal topological charge but opposite handedness; as such **our necklace-ring beam carries no angular momentum**. When launched into a self-focusing Kerr medium, a vortex ($e^{i\Omega\theta}$) ring beam disintegrates into filaments [41], which are themselves unstable and undergo either catastrophic collapse or expansion, as isolated (2+1) D Kerr solitons do [7]. If the self-focusing nonlinearity is saturable, the filaments created after the breakup form stable (2+1)D solitons [41]. Since the initial beam carries angular momentum, after the breakup each of the solitons shoots off tangentially. This transformation of vortex-ring beams into (2+1)D solitons seems universal to all saturable self-focusing nonlinearities, including quadratic [41] and photorefractive [41] media. All of these examples are related to the self-trapped necklace-ring beam we have found, but have important major differences from it. We have discussed them here just to clarify what our self-trapped necklace-ring beam is not.

2.6. DETAILED ANALYTICAL STUDIES OF NECKLACE BEAMS

In this Section, we show analytically how to predict and control the radial dynamics of necklace beams, and present analytic solutions for necklace beams in several parameter regimes. This Section is organized as follows. In Sub-Section 2.6.1, we provide a brief introduction to the radial dynamics of necklace beams. In Sub-Section 2.6.2, we describe a procedure that facilitates control over the instantaneous radial velocity of any necklace. In Sub-Section 2.6.3, we present analytical solutions to necklace beams in some specific regimes of parameters, as a function of the propagation distance. This enables a direct prediction of the radial acceleration of a necklace when its radial velocity is manipulated. However, this solution works well only in a limited range of necklace parameters. Consequently, in Sub-Section 2.6.4, we present a different analytical technique that allows one to predict the dynamics of any necklace as a function of its initial parameters. This technique can also predict what happens with the dynamics of the necklace once we manipulate the necklace's instantaneous radial velocity. However, the technique from Sub-Section 2.6.4 gives us no information whatsoever about the instantaneous necklace shape. In Sub-Section 2.6.5, we conclude this section by summarizing our predictions and propose new experiments.

2.6.1. A few words about radial dynamics of necklace beams

As we have seen in the previous sections, propagation of a necklace beam is in general not stationary: the beams exhibit slow radial expansion as they propagate. The expansion is a result of a net radial "force" that results from the azimuthally alternating phase, and is typically much slower than diffractive expansion. In some cases the nonlinear expansion is even negligible over all propagation distances of physical interest.

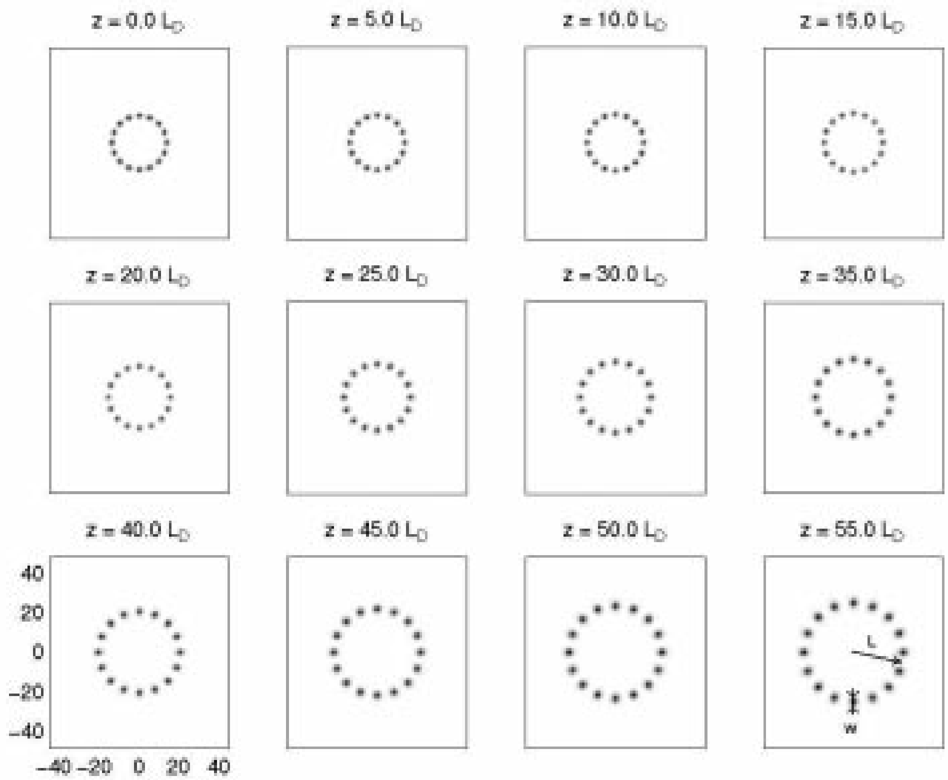

Figure 2.6-1: Example of evolution of a necklace beam with initial shape given by $\psi(r,\theta,z)=\alpha\cos(\Omega\theta)\text{sech}[(r-L)/w]$, where $\alpha=1$, $w=1$, $\Omega=8$, and $L/\Omega=1.707$. The necklace slowly expands as it propagates. The axes are the same for all plots. Dark color indicates high intensity.

The main feature of necklace beams is that the radial dynamics rate of necklaces is typically many orders of magnitude slower than the rate at which each of the pearls of the necklace would suffer catastrophic collapse if it were standing by itself. In other words, the necklace-ring beam exhibits stationary propagation for a very large distance, during which neither the ring diameter nor the width of each spot ("pearl") on the ring change significantly. For, example, consider Figure 2.6-1, where after 55 L_D, the radius of the necklace grew by less than a factor of 2. In contrast, each pearl (if standing by itself) undergoes catastrophic collapse (or diffraction) within only a few L_D. Therefore, with interactions (collisions) between necklace-ring "solitons" in mind, two self-trapped necklaces can mutually interact over a large distance during which they do not change their shapes appreciably. Thereby, one can use necklace-ring self-trapped beams to explore nonlinear interaction phenomena and collisions, (which are the most fascinating features of all solitons), in (2+1)D; this was previously thought to be undoable in (2+1)D self-focusing Kerr media (i.e., in a medium represented by the cubic self-focusing NLSE).

2.6.2. Controlling the Expansion Rate of the Self-Trapped Necklace Beams

As shown in section 2.3, necklaces typically grow as they propagate. The intuition behind this growth is that the amplitudes of the neighboring pearls are π out of phase, thereby repelling each other [1,42]; consequently there is a net radial force outwards on each pearl. For numerous reasons, it is important to have a means to control the expansion of the necklace-ring self-trapped beam. For example, it would be nice to be able to stop the expansion, and perhaps even reverse it, at least for some finite propagation distance. In fact, there is a natural way to obtain precisely this goal. Namely, one can take the necklace at any given propagation distance z, and multiply the whole shape with $exp(-i\Omega r)$, where r is the radial coordinate. Imposing such a radial (transverse) phase influences the radial velocity of each pearl. If the radial velocity of a pearl before applying the radial phase is v, then after the application of the phase, the net radial velocity is roughly v-Ω. Therefore, the instantaneous expansion velocity can be reduced to zero. Furthermore, one can even reverse this velocity so that the necklace immediately after the application of the transverse phase initially shrinks. This tool provides control over the instantaneous necklace radius growth. Such a radial phase structure is trivial to impose experimentally: one just shines a necklace through a "sharpened pencil" phase object, made from glass.

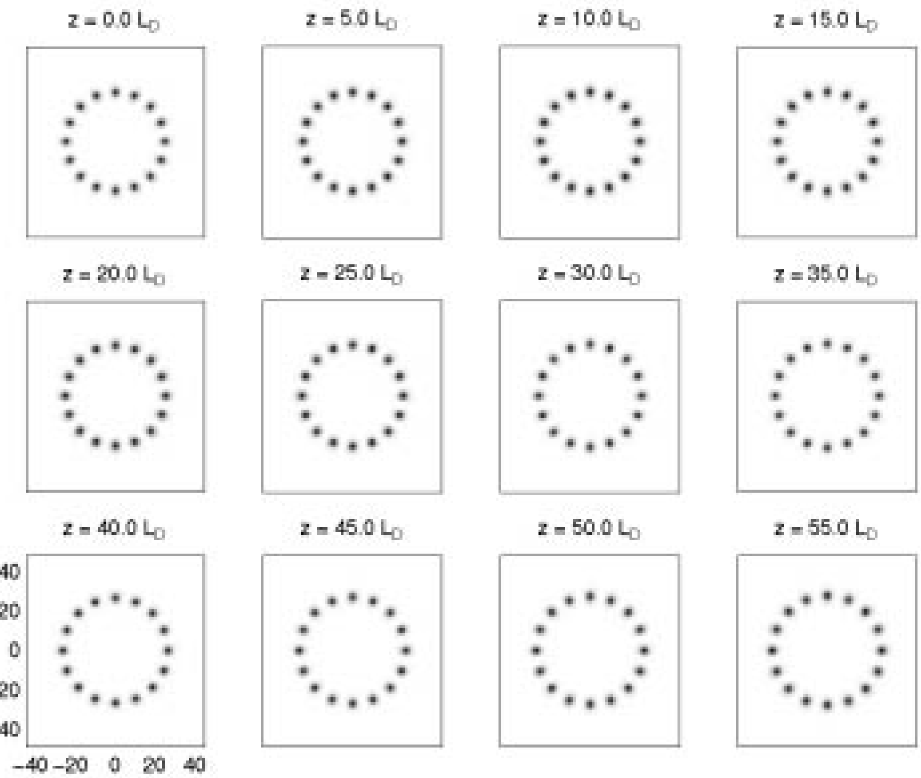

Figure 2.6-2: Stopping the necklace's instantaneous radial velocity. We take the necklace at the output of Figure 2.6-1, and measure its instantaneous radial velocity, v_0. Then, we multiply the whole shape with $exp(-iv_0r)$. The subsequent instantaneous radial velocity drops to 2% of the initial value.

The fact that we can produce a shrinking necklace in this manner is not inconsistent with the intuition that the neighboring pearls should repel each other. The procedure we have just suggested to make a shrinking necklace does not (!) in general make the radial acceleration negative, and thus does not turn the repulsion between adjacent "pearls" into attraction. To illustrate the idea, consider a necklace with 16 pearls, as we show in Figure 2.6-1, and let it propagate for a while. After $55L_D$, we measure its instantaneous radial velocity v_o, and multiply the whole shape with $exp(-iv_o r)$. As one can see in Figure 2.6-2, the instantaneous velocity is significantly reduced. A more careful measurement shows that the reduction in this particular case was from v_o to approximately -2% of v_o. However, the instantaneous radial acceleration stays positive, so the radial velocity of the necklace keeps increasing even after the application of the radial phase, as shown in Figure 2.6-2. In the subsequent sub-sections we analyze analytically what exactly happens with the radial acceleration as a result of the application of such a radial phase.

2.6.3. Approximate Analytic Solutions

In this sub-section, we use the action minimization approach in order to obtain an approximate analytical solution to the necklace shape as a function of the propagation distance, z. The solution we find works well only in certain regimes of necklace parameters. However, in these regimes it gives an excellent prediction for the radius of a necklace, the shape of the necklace, and its radial velocity as a function of the propagation distance. It also provides us with a quantitative understanding about what happens with the necklace once we multiply it with a radial phase, as proposed in Sub-Section 2.6.2.

We seek an approximate analytic solution in the regime where the radius of the necklace, L is much larger than its thickness w, as defined in the last plot of Figure 2.6-1. In addition, we consider only the cases where the thickness of the necklace w, is much larger than the rate of the azimuthal variation, $L\pi/4\Omega$. (Note that since we are comparing the width of the typical feature in the azimuthal direction with the thickness in the radial direction, $L\pi/4\Omega$ is the correct measure of the characteristic size of the azimuthal variation.) In this regime, the (2+1)D cubic self-focusing NLSE:

$$i\frac{\partial\psi}{\partial z}+\frac{1}{2}\left\{\frac{\partial^2\psi}{\partial r^2}+\frac{1}{r}\frac{\partial\psi}{\partial r}+\frac{1}{r^2}\frac{\partial^2\psi}{\partial\theta^2}\right\}+|\psi|^2\psi=0\,, \qquad (2.6\text{-}1)$$

can be approximated as:

$$i\frac{\partial\psi}{\partial z}+\frac{1}{2}\left\{\frac{\partial^2\psi}{\partial r^2}+\frac{1}{L^2}\frac{\partial^2\psi}{\partial\theta^2}\right\}+|\psi|^2\psi=0\,. \qquad (2.6\text{-}2)$$

Thus, one can attempt to write a solution to Eq. (2.6-2) as:

$$\psi(r,\theta,z)=e^{-i\Gamma z}\sum_{n=1}^{\infty}\sum_{m=1}^{\infty}\left\{\alpha_{n,m}\cos[(2n-1)\Omega\theta]*\sec h^{2m-1}[(r-L)/w]\right\}, \qquad (2.6\text{-}3)$$

with $\Gamma(w,L,\Omega)$, $\alpha_{n,m}(w,L,\Omega)$, and Ω is an integer. In this case, there exists a solution like Eq.(2.6-3) that has $\alpha_{1,1}$ of $O[(4w\Omega/L\pi)^2]$ larger than any other $\alpha_{n,m}$, and $(\alpha_{1,1})^2\approx 4/(3w^2)$. Consequently, our intuition tells us that the real solution can probably be well described by:

$$\psi(r,\theta,z)=\alpha(z)\cos(\Omega\theta)\sec h\{a(z)[r-L(z)]\}\exp[-i\Gamma(z)z+iv(z)r], \qquad (2.6\text{-}4)$$

provided that $\alpha^2(z=0)=4a^2(z=0)/3$, $v(z=0)=0$, $w/L<<1$, and $w>>L\pi/4\Omega$. We intend to look for $\alpha(z)$, $a(z)$, $L(z)$, $\Gamma(z)$, and $v(z)$ using the action minimization approach. Before proceeding, we emphasize that Eq. (2.6-4), when substituted into Eq. (2.6-1), produces an undesired singularity at the origin. Consequently, in our simulations, we actually multiply Eq.(2.6-4) at the input $(z=0)$ with a smoothly varying function that behaves $\propto r^2$ close to the origin, but assumes values close to unity in the regions where most of the energy of Eq. (2.6-4) is concentrated. An example of such a function is $\sin^2(r\pi/2L)$. Expanding this function around $r=L(z)$, we conclude that this function's presence influences our action integrals by $O((w/L)^2)$, so we are justified in ignoring its presence when evaluating our integrals; the only place where it actually matters is close to $r=0$, and its only purpose there is to eliminate the singularity. Therefore, when evaluating the action integrals in cylindrical coordinates below, we first integrate over θ, and when integrating over r, we keep in mind that the only important contributions to the integral are close to $r=L(z)$, while the contributions of the regions close to $r=0$ are negligible.

Our Lagrangian density therefore becomes:

$$L = i\left\{\psi\frac{\partial\psi^*}{\partial r} - \psi^*\frac{\partial\psi}{\partial r}\right\} + \left(\frac{\partial\psi}{\partial r}\right)\left(\frac{\partial\psi^*}{\partial r}\right) + \frac{1}{r^2}\left(\frac{\partial\psi}{\partial\theta}\right)\left(\frac{\partial\psi^*}{\partial\theta}\right) - |\psi|^4, \qquad (2.6\text{-}5)$$

Using the Lagrangian Equations of Motion:

$$\frac{\partial}{\partial z}\left[\frac{\partial L}{\partial\psi_z^*}\right] + \frac{1}{r}\frac{\partial}{\partial r}\left[r\frac{\partial L}{\partial\psi_r^*}\right] + \frac{\partial}{\partial\theta}\left[\frac{\partial L}{\partial\psi_\theta^*}\right] - \frac{\partial L}{\partial\psi^*} = 0, \qquad (2.6\text{-}6)$$

one can obtain Eq. (2.6-1) from Eq. (2.6-5). In the notation we are doing it, the action is given by:

$$S = \int_{-\infty}^{\infty} dz \int_{o}^{2\pi} d\theta \int_{0}^{\infty} r dr L \,. \qquad (2.6\text{-}7)$$

In order to evaluate the action, we need to evaluate a few integrals. To illustrate how we deal with the singularity at the origin, we present some of the integrals here. For example:

$$\int_0^\infty r \times \mathrm{sec}h^2[a(r-L)]dr \cong \int_{-\infty}^{\infty}(r-L)\mathrm{sec}h^2[a(r-L)]dr + \int_{-\infty}^{\infty} L \times \mathrm{sec}\,h^2[a(r-L)]dr = \frac{2L}{a},$$

since the first integrand is odd around $r=L$. Similarly, in the integral $\int_0^\infty \frac{dr}{r}\operatorname{sech}^2[a(r-L)]$, we can replace $\frac{1}{r}=\frac{1}{L}\left\{1-\frac{r-L}{L}+O\left[\left(\frac{w}{L}\right)^2\right]\right\}$, and integrate from -∞ to ∞ instead, not worrying about what happens at the origin because of the presence of the modulating function which annihilates the singularity, as explained above. The other integrals are evaluated in a similar manner. After a few additional lines of algebra, we obtain:

$$S=\pi\int_{-\infty}^{\infty}dz\left\{\frac{4v_z\alpha^2L^2}{a}-\frac{4L\alpha^2}{a}\frac{\partial}{\partial z}[\Gamma z]+\frac{2a\alpha^2L}{3}+\frac{2\alpha^2v^2L}{a}+\frac{2\Omega^2\alpha^2}{aL}-\frac{4L\alpha^4}{3a}\right\}. \qquad (2.6\text{-}8)$$

In order to save ourselves some algebra, we also impose energy conservation for the ansatz in Eq. (2.6-4). $E=\iint|\psi|^2d^2r\cong 2\pi\alpha^2L/a$. We can use this to eliminate *a(z)* from Eq. (2.6-8) in terms of the other variables. We substitute $a=2\pi\alpha^2L/E$ in Eq. (2.6-8), where E is a constant. Finally, we require the minimization of the action in Eq. (2.6-8) as:

$$\frac{\delta S}{\delta\Gamma(\xi)}=\frac{\delta S}{\delta L(\xi)}=\frac{\delta S}{\delta\alpha(\xi)}=\frac{\delta S}{\delta v(\xi)}=0, \qquad (2.6\text{-}9)$$

thereby obtaining: $2\pi\alpha L/E=1$, $L_z=v$, and $v_z=(\Omega^2-E^2/12\pi^2)/L^3$, (the subscripts z denote derivatives with respect to z) while the minimization with respect to $\Gamma(\xi)$ does not yield any useful result. From these equations we also obtain $a=E/2L\pi$. Integrating these ODEs we obtain:

$$L(z)=\sqrt{\left[\frac{1}{L_0^2}\left(\Omega^2-\frac{E^2}{12\pi^2}\right)+v_0^2\right]z^2+2L_0v_0z+L_0^2}, \qquad (2.6\text{-}10)$$

where the subscript zero denotes the initial conditions, at $z=0$.

Note that our ansatz therefore describes a solution whose intensity, and shape scale simply as a function of *z*, preserving the total energy as the necklace expands, which is consistent with our intuition from section 2.3.

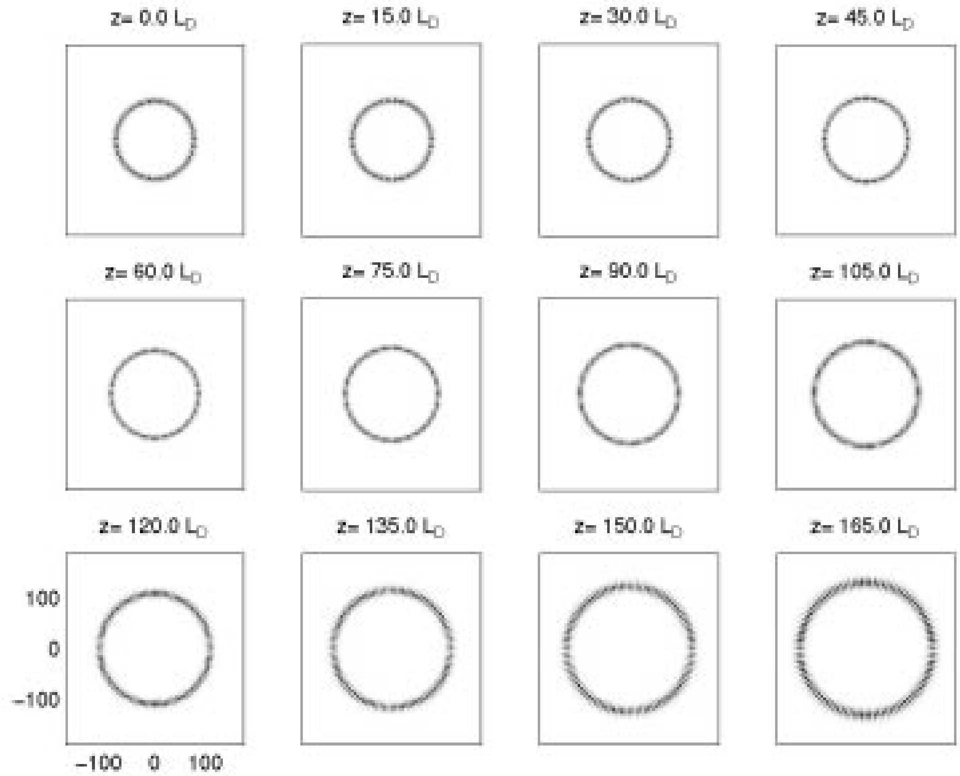

Figure 2.6-3: A necklace whose parameters are in the regime that can be analyzed by the least action principle. At the input of this necklace, w=5, L=76.8, Ω=50, and $\alpha^2=4/(3w^2)$. The analytical solutions we find approximate the subsequent evolution of the shape of this necklace to within a few percent. The regime that can be understood analytically is described by the parameters that satisfy: $\alpha^2=4/(3w^2)$, w/L<<1, and Lπ/4Ω<<w.

To test our analytical results, we simulate the evolution of a few necklaces using split-step Fourier method and compare the necklace beams evolving (expanding) during propagation with the approximate analytic solution presented in Eq. (2.6-4). Given the insight provided by Eq. (2.6-3), we expect to obtain the best results when our input conditions were:

$$\psi(r,\theta,z=0)=\alpha\cos(\Omega\theta)\sec h\{[r-L]/w\}, \tag{2.6-11}$$

where $\alpha^2=4/(3w^2)$, $w/L<<1$, and $L\pi/4\Omega<<w$. Note that the solution from Eq. (2.6-4) satisfies Eq. (2.6-1) best if the initial radial velocity, $v(z=0)=0$, so we take it to be zero. Further, in the simulations, the input waveform given by Eq. (2.6-11) is multiplied by $sin^2(\pi r/2L)$ in order to eliminate the singularity at the origin. Nevertheless, as explained above, this modulation to a very good approximation has no other influence on subsequent dynamics or necklace shape. For the example presented in Figure 2.6-3, $L=76.8$, $w=5$, and $\Omega=50$. At the output of the propagation, after $z=165$, the width of the necklace is $L=130.04$. The intensity overlap of the final necklace (which evolved throughout propagation) with the approximate necklace solution given by Eq. (2.6-4) that had $L=130.04$ was approximately 97%. In other words, if we denote the final necklace with ψ_1, and the approximate necklace solution with ψ_2, we get that the overlap is:

$$\frac{\iint d^2r\left||\psi_1|^2-|\psi_2|^2\right|}{\iint d^2r\left\{|\psi_1|^2+|\psi_2|^2\right\}}\approx 0.03. \tag{2.6-12}$$

Furthermore, we check our prediction for $L(z)$ as given by Eq. (2.6-10) against our numerical simulations. The result presented in Figure 2.6-4 shows a very good agreement between the analytic (approximate) prediction and direct simulation.

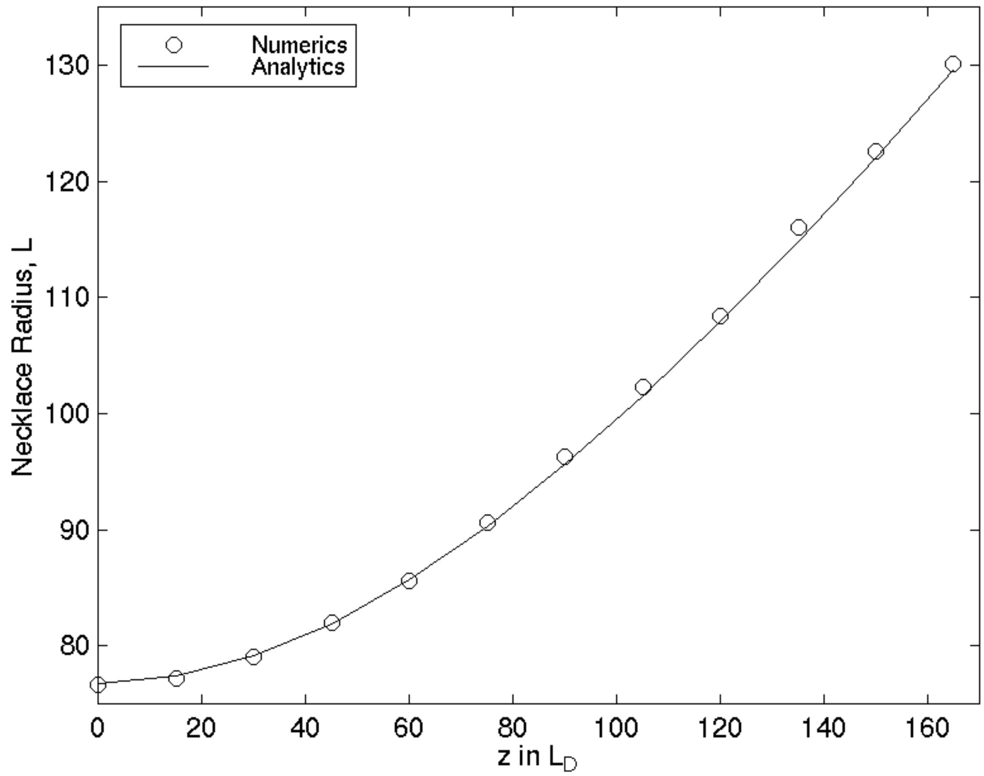

Figure 2.6-4: Predicting the instantaneous necklace radius, of the necklace from Figure 2.6-3, using the least action principle.

In addition to these excellent agreements (between the analytics and the numerics) in the shape and the radius of the necklaces, we measure the radial velocity *v(z=165)* of the necklace at the output, and find that it disagrees with the prediction given by Eq. (2.6-10) by less than 3%. Furthermore, we take the output at *z=165*, and multiply the whole shape with *exp{-iv(z=165)r}*. According to our analytical predictions, this should have reduced the instantaneous radial velocity of the necklace to zero. Indeed, it reduced the instantaneous radial velocity to less than 2.5% of its initial value.

To conclude this sub-section, the agreement between the analytical theory and the numerical results is very good. Since we expect our results to be valid only to $O[(L\pi/4\Omega w)^2]$, or $O[(w/L)^2]$, one should not have expected the agreement to be better than $O(few\%)$ for the particular necklace presented in Figure 2.6-3.

Unfortunately, our analytical solution works only when the required smallness parameters are truly small. In particular, $(L\pi/4\Omega w)^2=1/17.18$, and $(w/L)^2=1/236$ for the necklace of Figure 2.6-3. When the required smallness parameters are closer to unity, one can probably still obtain reasonable analytical solutions by including more terms from the expansion in Eq. (2.6-3) (rather than including only the lowest order terms) into the ansatz of Eq. (2.6-4). However, one of the requirements for the stability of any necklace beam is that the azimuthal width of the pearls has to be of the same order or smaller than the radial width of the pearl. In addition, the radius of any necklace should be significantly larger than its thickness. Therefore, typical stable necklace-ring beams that we expect to be stable in self-focusing Kerr media naturally have the required parameters small, which makes the proposed expansion seem promising. Extending the regime of validity of our approximate method by including higher order terms is beyond the scope of this thesis, and we leave it to future research.

2.6.4. Predicting and Controlling the Expansion Rates of Arbitrary Self-Trapped Necklaces

As shown in the previous sub-section, an excellent analytical solution for self-trapped necklace beams can be found in certain regimes of parameters. However, the approach of the previous sub-section does not work in some rather interesting regimes of necklace parameters; consequently we are not able to write down the explicit analytical solution in those regimes. In this sub-section, we present another analytical approach that gives a good prediction for the radius of the necklace as a function of the initial necklace shape and the propagation distance. This approach works even though one does not know the instantaneous analytical solution for the necklace shape. It can also be used to predict the dynamics of a necklace after multiplication with an arbitrary radial phase. But, this approach below works **only** for the (2+1)D self-focusing cubic NLSE, whereas the approach from Sub-Section 2.6.3 seems to be adaptable for any number of dimensions, and for any form of nonlinearity. In any case, it is worthwhile to present both approaches in this section, and also to use them as a mutual check on each other.

We follow the approach given in [43,39] to derive the instantaneous radius of the necklace radius as a function of the propagation distance, and the initial necklace shape. First, we need to define the energy:

$$E = \iint_{SPACE} d^2x \left|\psi(z=0)\right|^2 , \qquad (2.6\text{-}13)$$

and also the Hamiltonian:

$$H = \iint d^2x \left\{ \left(\nabla \psi(z=0)\right) \bullet \left(\nabla \psi^*(z=0)\right) - \left|\psi(z=0)\right|^4 \right\}. \qquad (2.6\text{-}14)$$

Both E, and H are conserved. Energy is conserved because of the symmetry of Eq. (2.6-1) with respect to a phase shift. Hamiltonian is conserved because of the invariance of Eq. (2.6-1) with respect to a shift in z. Therefore, using Noether's theorem one can prove that E and H as defined in Eq (2.6-13) and Eq. (2.6-14) are conserved (alternatively, one can use the method given in Ref. [35] to show this). Defining:

$$R^2(z) \equiv \frac{1}{E} \iint d^2x \left\{ \left|\psi(z)\right|^2 r^2 \right\}, \qquad (2.6\text{-}15)$$

after a few lines of algebra, one can show:

$$\frac{d^2\left[R^2(z)\right]}{dz^2} = 2\frac{H}{E}, \qquad (2.6\text{-}16)$$

which thus provides us with another very useful conserved quantity. Defining the local current in the usual way:

$$\mathbf{j}(r,\theta,z) \equiv \frac{i}{2}\left\{\psi(r,\theta,z)\nabla\psi^*(r,\theta,z) - \psi^*(r,\theta,z)\nabla\psi(r,\theta,z)\right\}, \qquad (2.6\text{-}17)$$

one can show that:

$$\frac{d\left[R^2(z)\right]}{dz} = \frac{2}{E}\iint_{SPACE} d^2x\left\{\mathbf{j}(r,\theta,z)\bullet\mathbf{r}\right\}. \qquad (2.6\text{-}18)$$

Therefore, given the initial condition $\psi(r,\theta,z=0)$, we can integrate the Eq. (2.6-16) to obtain:

$$R^2(z) = \frac{H}{E}z^2 + \frac{2z}{E}\iint_{SPACE} d^2x\left\{\mathbf{j}(r,\theta,z=0)\bullet\mathbf{r}\right\} + R^2(z=0)\,. \qquad (2.6\text{-}19)$$

How can we use this result? Well, if it is a valid assumption that most of the initial necklace energy stays bound to the necklace as the necklace propagates, (i.e. only a negligible amount of E and H are carried away from the necklace as the necklace propagates, as we fully expect from self-trapped propagation and as we have found numerically in section 2.4 and in the examples in that section), then Eq. (2.6-19) lets us predict the instantaneous necklace radius $L(z)$. (By $L(z)$ we mean the distance from the origin where $|\psi(r,\theta,z)|$ is largest; See Figure 2.6-1) This is because it is trivial to show that for typical necklaces $L(z) \approx \sqrt{R^2(z)}$ up to $O(w^2/L^2)$ as long as w/L is small, which is naturally satisfied by all self-trapped necklaces of interest (i.e., those that propagate in a stable fashion in Kerr media).

It is now instructive to compare the prediction from Eq. (2.6-19) with the prediction we obtained using the action minimization approach in Sub-Section 2.6.3, like Eq. (2.6-10). Adapting Eq. (2.6-19) for the necklace of Figure 2.6-3, we find

$$L(z) \approx \sqrt{R^2(z)} = \sqrt{\left[\frac{1}{L_0^2}\left(\Omega^2 - \frac{3E^2}{64\pi^2}\right)\right]z^2 + R_0^2}\ . \qquad (2.6\text{-}20)$$

Comparing this with Eq. (2.6-10), after setting $v_o=0$ in that equation, we see that the relative error in the term proportional to z^2 is $7E^2/192\pi^2\Omega^2=7L_o^2/27\Omega^2w^2$, which is tiny for that necklace. Similarly, as we have already shown, the error in the term proportional to z^0 is $O(w^2/L^2)$ which is again negligible. Extending this analysis for the cases where $v_o\neq 0$ is a bit more involved, but the result is again that the two approaches differ only by a tiny amount which is set by the smallness parameters of the necklace.

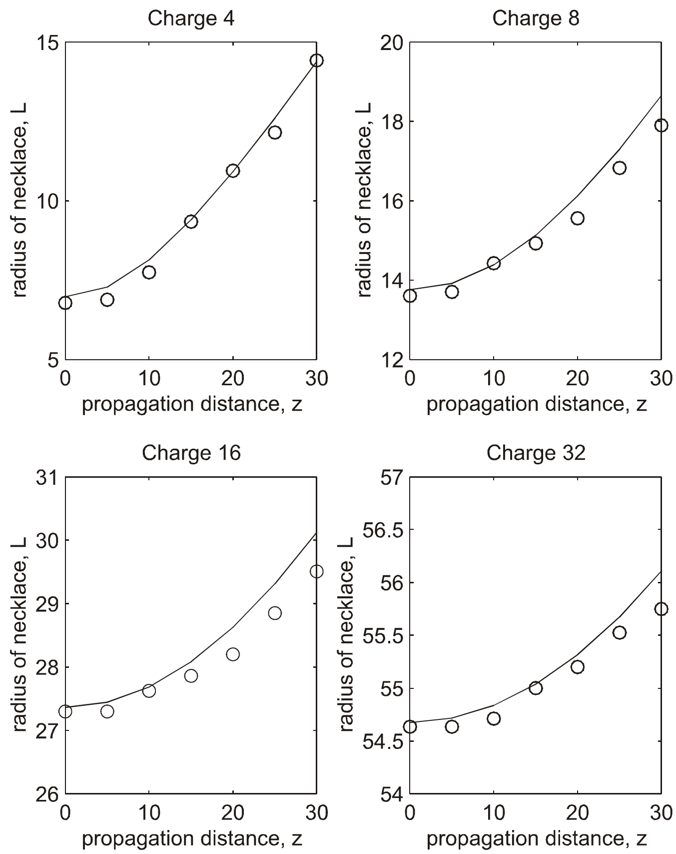

Figure 2.6-5: Predicting the expansion rates of arbitrary self-trapped necklaces: comparison between numerical beam-propagation results and analytical predictions. All necklaces here have $L/\Omega=1.707$, $\alpha=1$, and $w=1$. Their respective charges are $\Omega=4,8,16$, and 32. The analytical approach used here is based on using some conservation laws of the (2+1)D cubic NLSE, in order to find the instantaneous necklace radius directly. This approach works for a necklace of arbitrary parameters as long as most of its initial Energy and Hamiltonian are self-trapped to the necklace as it propagates.

In order to test our results, we simulate numerically several typical examples of self-trapped necklaces and compare them with the prediction given by Eq. (2.6-19). We obtain best results if the initial shapes are as close to the true "equilibrium" shape as possible, because in that case only a negligible amount of energy is carried away with radiation through subsequent breathing of the necklace. (In other cases, some energy is lost to radiation in the formation process of the necklace, as always occurs in the formation of solitons from a non-perfect input). However, since there are no analytical solutions for necklaces in all regimes, a typical necklace at the input is only an approximation to the equilibrium necklace shape. Nevertheless, this technique gives us a good prediction of the subsequent necklace dynamics, provided that not much energy is eventually scattered into radiation. In any case, experimentally, all necklaces are expected to be launched with a $\psi(z=0)$ real, so $L(z) \approx \sqrt{\frac{H}{E} z^2 + L^2(z=0)}$. Our necklaces at the input are given by:

$$\psi(r,\theta,z=0) = \alpha \cos(\Omega\theta) \operatorname{sec}h\left(\frac{r-L}{w}\right) \sin^2\left(\frac{r\pi}{2L}\right), \qquad (2.6\text{-}21)$$

where $L/\Omega=1.7072, w=1$, and $\alpha=1$; according to our experience this input shape is close to the equilibrium necklace shape. As examples, we consider the cases where Ω=4,8,16, and 32. The purpose of the sin^2 term in Eq. (2.6-21) is again only to eliminate the singularity at the origin; we can ignore this term when performing the relevant integrals, as we did in Sub-Section 2.6.3, since the relative mistake is only $O(w^2/L^2)$ which is negligible for our necklaces. All the relevant integrals needed to obtain the Hamiltonian and Energy are evaluated in exactly the same manner as in Sub-Section 2.6.3. Therefore, we obtain:

$$L(z) \approx \sqrt{\left\{\frac{1}{3w^2} + \frac{\Omega^2}{L^2} - \frac{\alpha^2}{2}\right\} z^2 + L^2(z=0)}\,. \qquad (2.6\text{-}22)$$

For each of the necklaces, we compare the prediction given by Eq. (2.6-22), with the actual numerical experiment. The result is shown in Figure 2.6-5. The circles represent numerical data, while the solid lines represent the predictions given by Eq. (2.6-22). As we can see, our analytical prediction is a fairly good approximation for reasonable propagation distances (a few tenths of diffraction lengths). Keeping in mind that the largest propagation distance observed so far for spatial solitons is roughly $20L_D$, being able to make analytical prediction up to a distance of $30L_D$ is very useful. However, the real value of the prediction in Eq. (2.6-22) is that it gives a good estimate for the dynamics even for necklace beams whose shape is not initially very close to the existence curve. For example, we launch a few necklaces that have very similar dimensions to those in Figure 2.6-5, but with a Gaussian, instead of a sech shape at the input. This shape is not close to the equilibrium necklace shape; nevertheless, the agreement between the numerical results and the analytical predictions for the expansion of the Necklace beams is still reasonably good, as shown in Figure 2.6-6.

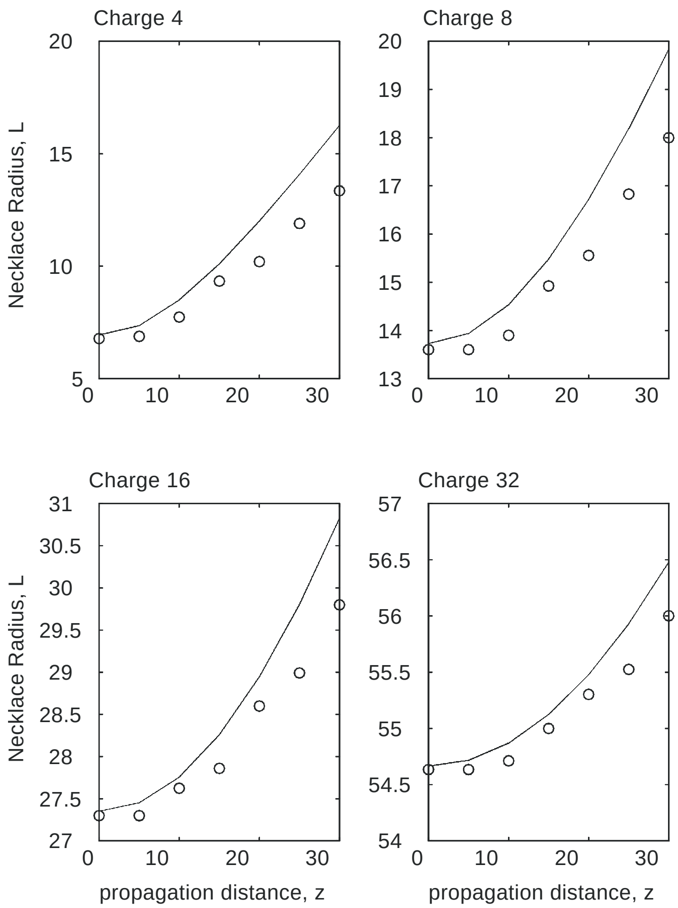

Figure 2.6-6: Predicting the expansion rates of arbitrary necklaces whose shapes are not close to the equilibrium shapes initially. These necklaces have the same FWHMs, radiuses, energies, and Ωs as their counterparts in Figure 2.6-5. But, their radial profiles are initially Gaussian instead of sech shaped. Thus, they are not close to the equilibrium self-trapped shapes. Nevertheless, the analytic approach used in Figure 2.6-5 still gives a useful approximation when predicting the radial necklace dynamics.

Now that we have an analytical expression for the necklace dynamics, as given by Eq. (2.6-22), we can study the feasibility of making a stationary necklace. That is, we would like to know whether it is possible to construct a necklace that would not change its radius at all as it propagates. Looking at Eq. (2.6-22) it seems that all we have to do is construct a necklace whose parameters make the term proportional to z^2 in Eq. (2.6-22) to zero. For example, we can fix $w=\alpha=1$, and pick L that will make the given term zero. However, in that case we conclude that the azimuthal width of each pearl, $L\pi/4\Omega=1.92$, which is bigger than the radial width of the pearl, and therefore such necklace beam is not stable in self-focusing Kerr media. For the given intensity, the pearl will self-focus in the azimuthal direction, and this will eventually destabilize the necklace and disintegrate it. We run the simulation with these precise parameters, and our expectations were confirmed. The radius of the necklace does not change almost at all. However, each pearl keeps shrinking in the azimuthal direction, and the necklace destabilizes within $O(40L_D)$. Therefore, setting $w=\alpha=1$ and choosing an L that eliminates the term proportional to z^2 in Eq. (2.6-22), yields a non-expanding Necklace that is basically unstable but can survive for tens of L_D's. Another option to stop the expansion is to increase only α. We take the necklace from Figure 2.6-1, and keeping all of its other parameters fixed, we increase α till the term proportional to z^2 in Eq. (2.6-22) vanishes. Unfortunately, the necessary α is equal to 1.16, which is too far off the equilibrium necklace shape. As shown in Figure 2.6-7, this alternative also leads to non-stationary propagation because the pearls keep shrinking, even though the necklace radius is largely unchanged till $O(40L_D)$. Thus, choosing parameters so that the term proportional to z^2 in Eq. (2.6-22) is set to zero seems not to be a fully satisfactory method for stopping the necklace expansion.

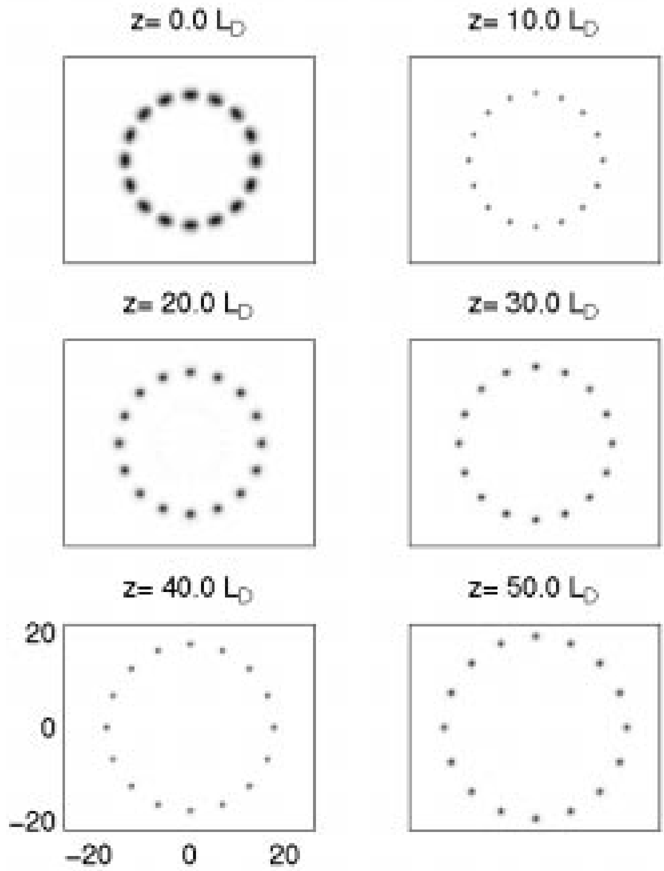

Figure 2.6-7: A Necklace with no radial dynamics. Our analytical understanding of radial dynamics of necklaces lets us design a necklace whose radius is stationary as the necklace propagates. The necklace presented here has α=1.16, w=1, Ω=8, and L/Ω=1.707. Unfortunately, this necklace has α far away from the equilibrium shape. Thus, each pearl has its own dynamics that eventually (after $O(40L_D)$) destabilizes the necklace. Nevertheless, as long as the necklace is stable (till $O(40L_D)$), its radius does not change as was predicted by our analytics.

Even though the structure in Figure 2.6-7 is clearly non-stationary, there are important lessons to be learned from it. The first lesson is that our analytical expression Eq. (2.6-22) seems to work well, giving correct predictions even when the initial shapes are far away from the equilibrium necklace shapes. Furthermore, by increasing the azimuthal width of each pearl a little, and also increasing the peak amplitude slightly, one could produce a necklace beam that would be stable and stationary for a fairly long distance, say $O(40L_D)$. Eventually, the necklace would disintegrate since its initial shape would be too far away from the equilibrium necklace shape [44]. However, the propagation distance during which such a necklace is stable is sufficient for experimental interest and its conditions are not too stringent. Finally, as the result from Figure 2.6-7 clearly demonstrates, our previous intuition, that the force holding the necklace together results from repulsion between adjacent "pearl"-solitons, needs to be reexamined more carefully. In particular, Eq. (2.6-22) implies that by choosing the proper parameters, one can make both the initial radial velocity, and the initial radial acceleration of the necklace to be negative. Sure enough, such a necklace eventually turns out to be unstable, but this fact does not diminish the fact that the necklace is held together by a force that is not net repulsion only. One can think about this force as "surface tension", yet thus far the analogy is not really substantiated.

We now proceed to use the analytical tools from above to analyze what happens if one introduces an arbitrary radial phase to any necklace, at an arbitrary moment z_o. In particular, we assume $\psi(r,\theta,z_{o+})=\psi(r,\theta,z_o)exp(ivr)$, where z_{o+} denotes the moment immediately after imposing the radial phase, and z_o denotes the moment immediately before. After a few lines of algebra, we get $E(z_o)=E(z_{o+})$, and also:

$$\left.\frac{d\left[R^2(z)\right]}{dz}\right|_{Zo+} = \left.\frac{d\left[R^2(z)\right]}{dz}\right|_{Zo} + \frac{2v}{E}\iint_{SPACE} d^2x\left|\psi(z_0)\right|^2 r\,. \qquad (2.6\text{-}23)$$

Note that for typical necklaces the last term in Eq. (2.6-20) is very close to $2vL(z_o)$. Approximating $L^2(z)\approx R^2(z)$ in Eq. (2.6-23), we therefore obtain:

$$\left.\frac{dL(z)}{dz}\right|_{Zo+} = \left.\frac{dL(z)}{dz}\right|_{Zo} + v\,, \tag{2.6-24}$$

which is exactly as expected. Furthermore, we can also find out what happens with the Hamiltonian after imposing this radial phase:

$$H(z_{0+}) = H(z_0) + v^2 E + 2v \iint_{SPACE} d^2x \left\{ \mathbf{j}(r,\theta,z_0) \bullet \hat{\mathbf{r}} \right\}. \tag{2.6-25}$$

Since the last term in Eq. (2.6-25) is negative for a negative radial phase, it is not clear whether imposing a radial phase in order to stop the instantaneous radial expansion would typically decrease, or increase the Hamiltonian. Thus, we do not know how would it influence the term proportional to z^2 in Eq. (2.6-19). Note that this term is related (but not equal) to the instantaneous radial acceleration of each pearl. To proceed with our analysis, we assume that at the input *(z=0)* we start with a necklace beam that has zero radial velocity. Then, we propagate the necklace for some z_o, at which point according to our analysis in Eq. (2.6-19), its radial velocity should be given by approximately $v_o=Hz_o/EL(z_o)$. Therefore, we multiply the whole shape with $exp(-iv_o r)$. Then, we notice the similarity between the last term in Eq. (2.6-25), and the Eq. (2.6-18) to conclude:

$$H(z_{0+}) = H(z_0)\frac{L^2(z=0)}{L^2(z=z_0)}\,. \tag{2.6-26}$$

This is telling us that after imposing the radial phase, the necklace will have the same dynamics as the scaled-up version of the necklace we started with at *z=0*. This is consistent with our picture from section 2.3 that the intensity of the necklace to a good approximation simply scales as the necklace propagates, according to the rescaling properties of Eq. (2.6-1) which conserve the energy in the beam. Notice that in addition to extinguishing the instantaneous radial velocity, we have also slowed down the subsequent dynamics, as one can see by comparing Figures 2.6-1 and 2.6-2. In a way, this is expected, because it is natural that a scaled-up necklace would have a slower dynamics, exactly by the factor given in Eq. (2.6-26).

By imposing a large enough negative radial phase, the radial acceleration can in principle be turned into zero, or even negative. But, this is not a stable solution because the radial phase needed to obtain this is huge compared to other necklace parameters, making this proposal infeasible. Also, in that case the necklace would keep contracting till it destroys itself (each pearl undergoes the equivalent of catastrophic collapse). Consequently, in typical experimental realizations, one would probably want to let necklace expand for a while, then impose a large enough negative radial phase to make it contract for a while, till it starts expanding again. Then one would impose a negative radial phase again, etc.

2.6.5. Conclusion of section 2.6

In section 2.6, with collision experiments in mind, we investigate the possibility to control the dynamics of necklace beams. Using the action minimization approach, we find analytical solutions for the necklace shapes in specific regimes of necklace parameters, and present analytical techniques for predicting the radial dynamics of necklace of any arbitrary initial shape, even if the shape is not close to the equilibrium necklace shape. We also present a procedure that enables us to control, and reverse the instantaneous necklace radial dynamics. All the tools that we presented in this section enable us to design many different necklaces that are essentially stationary over most propagation distances of physical interest: tens of diffraction lengths.

2.7. CONCLUSION OF CHAPTER 2

In conclusion, we have presented a new form of a self-trapped beam in self-focusing Kerr media: a necklace-ring beam. Even though we do not know if this necklace beam is stable in the absolute sense, we find numerically that it exhibits stable propagation for at least *O(100)* diffraction lengths, which is more than enough for experimental observations. Such necklace-ring beams slowly expand but fully preserve their structure.

Self-trapped necklace beams resemble solitons in many ways: a Necklace conserves energy and momentum and does not change its shape over the experimentally reachable propagation distances. Therefore, for all practical purposes, we can treat the self-trapped Necklaces as "quasi-solitons" of the (2+1)D self-focusing cubic NLSE. This is in sharp contrast to the previously held belief that this equation does not support solitons. Consequently, as an avenue of further research, we envision studying all solitonic effects with necklaces, both experimentally and theoretically. Furthermore, we propose studying necklace beams in other non-linear media (not just Kerr); in particular, studying necklace interaction in saturable media seems to be a very promising direction for further research.

Finally, we emphasize that the importance of this work lies in the fact that self-trapped Necklace-ring beams should be observable in all nonlinear systems described by the cubic (2+1)D nonlinear Schrodinger equation: practically in almost all centrosymmetric nonlinear systems in nature that describe envelope waves [4].

3. NECKLACES CARRYING ANGULAR MOMENTUM

3.1. INTRODUCTION AND BACKGROUND

In this chapter, we present self-trapped necklace beams that carry angular momentum. In contrast to all known results with bright and dark solitons, the angular momentum borne on such self-trapped entities can be a non-integer multiple of the energy. Furthermore, we demonstrate the effect of slowing-down of angular velocity due to the increase of the moment of inertia of the necklace beams as they propagate. Most of the material presented in this chapter has been submitted for publication [30].

Solitons that carry angular momentum have been well studied in many systems, for example, optical dark vortex solitons [46], 3D spiraling-interaction of bright optical spatial solitons [47], composite spatial solitons [48], quadratic solitons [49], and ring-solitons in a cubic-quintic nonlinearity [50], to name a few. Over the years, several experiments involving transfer of angular momentum (not just of spin) carried by light to other forms of angular momentum have been performed [51]. In particular, the orbital angular momentum of optical beams is most-commonly associated with an azimuthal phase modulation of the EM field by $\exp(iM\theta)$ [52]. Such a phase modulation provides a local angular velocity with respect to the center of the beam to every part of the beam. The EM field of solitons is continuous wherever the amplitude is non-zero, that is, everywhere except for the origin. This fact bears much significance, because a field discontinuity where the amplitude is non-zero renders the soliton highly unstable, even in a self-defocusing medium. For this reason of stability, for all dark vortex solitons (which all have an $\exp(iM\theta)$ phase dependence), M is an integer [53]. For the very same reason, for all other forms of single solitons carrying angular momentum found as of yet [46,48,49,50], M is an integer. In particular, in the (2+1)D cubic (Kerr) self-focusing NLSE

$$i\frac{\partial\psi}{\partial z}+\frac{1}{2}\left\{\frac{\partial^2\psi}{\partial r^2}+\frac{1}{r}\frac{\partial\psi}{\partial r}+\frac{1}{r^2}\frac{\partial^2\psi}{\partial\theta^2}\right\}+|\psi|^2\psi=0\,, \tag{3.1-1}$$

the energy is $E=\iint|\psi|^2dxdy$ and the angular momentum is $\mathbf{L}=\frac{i}{2}\iint\mathbf{r}\times\{\psi\nabla\psi^*-\psi^*\nabla\psi\}dxdy$. It is trivial to show that any beam that can be written as ψ(r,θ)=f(r)exp(iMθ), has L/E=M. Since neither the definition of L, or E depend on the particular non-linearity involved, this result holds for all types of non-linearities. [Similarly, in quantum mechanics (QM), neither the definition of L, or the definition of the total probability depend on the particular form of the potential involved.] Thus, all optical solitons found (theoretically or experimentally) thus far, carry an integer L/E. If one calculates the real, physical angular momentum carried by such a beam, one will conclude that (within the paraxial approximation) the angular momentum (when averaged over the number of photons) is exactly M$\hbar$ per photon [52]. (If the light is circularly polarized, this has to be modified by the spin contribution of $\pm\hbar$ per photon.)

Physically, the fact that L/E is an integer can be intuitively understood by comparison with quantum mechanics. All solitons in optics (within the paraxial or slowly-varying amplitude approximation) are described by a Schrodinger equation. In QM, the solutions of this equation have a quantized angular momentum which has to be an integer multiple of $\hbar$, and $\iint|\psi|^2dxdy$ is normalized to 1 (since it represents the total probability in QM). In contrast, in classical optics $\iint|\psi|^2dxdy$ represents the total power carried upon the beam, which is proportional to the average number of photons (and of course there is no $\hbar$ in classical optics). Thus, the quantization of L in QM (in terms of $\hbar$) resembles the fact that L/E is integer for all **solitons** found thus far of a **classical** (2+1)D normalized NLSE. We emphasize that L/E is an integer not because of quantization reasons, but rather because a non-integer L/E typically leads to a field discontinuity where the intensity is non-zero; such a discontinuity is thought to be unstable in self-focusing/defocusing media. Here we find self-trapped structures which carry non-integer L/E yet propagate in a stable fashion for many diffraction lengths: **quasi-solitons that carry non-integer per-photon angular momentum.** These possess the structure of necklace-ring beams.

3.2. NECKLACE BEAMS CARRYING INTEGER L/E

Consider a necklace beam whose shape at the input to the propagation is approximated by $\psi(r,\theta,z=0)=f(r)\cos(\Omega\theta)$, for some f(r) [54], and add to it the angular momentum with $\exp(iM\theta)$. (Here, Ω, M are integers.) Thus, the input shape is $\psi(r,\theta,z=0)=f(r)\cos(\Omega\theta)\exp(iM\theta)$. As long as M is reasonably smaller than Ω, we find that this necklace is stable in all our simulations, for more than 50 diffraction lengths, L_D [56]. After 50 L_D we reach our computational limitations, so it is very plausible that the necklaces are stable for much larger propagation distances. Such shapes have L/E=M. Since the symmetry between the pearls has to be preserved in a stable necklace rotation, the angular momentum is manifested in a very direct way: the entire necklace rotates as it propagates (Fig. 3.2-1). Quantization of L/E manifests itself in our simulations in the fact that, for a necklace whose all parameters are fixed (except for its M), only certain angular velocities ω are allowed; these ω's are given by approximately M/R^2. The agreement between this analytical prediction for ω, and our numerical simulations is better than 1% typically. Another interesting thing to point out here is the **differential rotation of necklaces**: two necklaces that differ only in their radii (but not in their M's) differ in their ω's by a squared ratio of their radii.

The fact that the allowed ω's are quantized shows a close connection between solitons and bound states in quantum mechanics! Both of these systems are described by very similar wave equations; thus we expect them to display quite a few similar properties. However, the fact that some wave-quantities that relate to the relation between solitons and particles are thus necessarily quantized in optics was not appreciated so far.

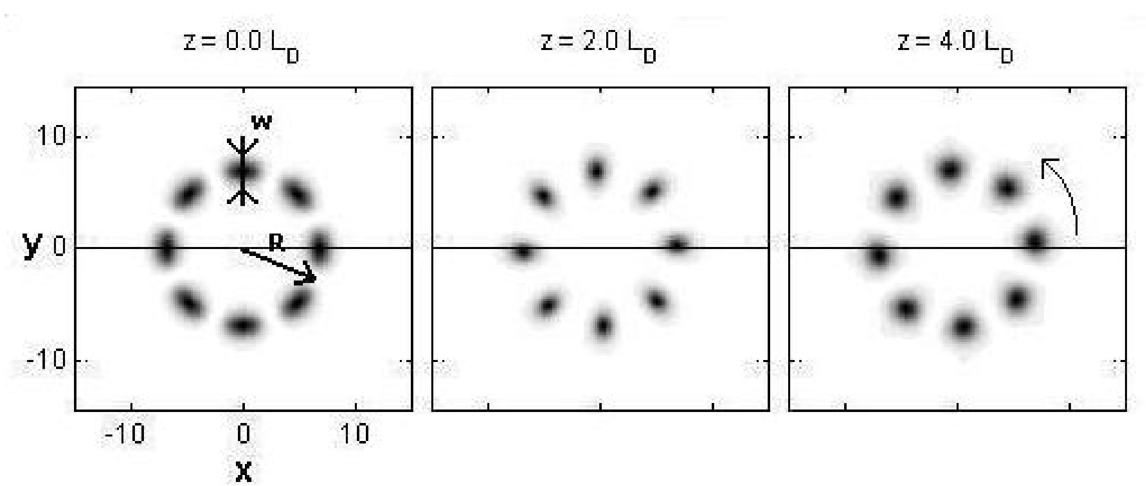

Fig 3.2-1: A rotating necklace with integer L/E. We launch a necklace close to equilibrium self-trapped necklace shape. It "breathes" for a short distance, until it reaches the equilibrium shape. In addition, as it is clear from the figure above, this necklace slowly rotates as it propagates. The input shape (in the regions that contain most of its energy), is $\psi(r,\theta,z=0)=\mathrm{sech}(r-6.83)\cos(4\theta)\exp(i\theta)$. Dark means high intensity.

As described in chapter 2, self-trapped necklace beams typically slowly expand as they propagate. The expansion is a consequence of the net radial force exerted on each of the spots in the necklace. However, even though the necklace beam slowly expands, the expansion is very different (and much slower) than diffractive expansion: it is uniform and it preserves the shape of the necklace. Once angular momentum is added to a self-trapped necklace beam, it expands faster. In other words, for two necklaces that differ only in their M's, the one with larger M expands noticeably faster. Consequently, in our simulations, we observe centrifugal force in a very direct way in a solitonic system. Furthermore, as a necklace beam expands, its L and E are conserved, but this means that ω (the angular velocity) cannot be conserved. This is similar to a skater on ice: if she extends her hands while she rotates, her angular velocity ω decreases. As shown in Fig 3.2-2, we observe this effect with necklace beams. Analytically, angular phase has to be conserved, because in a smooth continuous evolution, the phase would have to discontinuously jump from, say, $\exp(i\theta)$ to $\exp(i2\theta)$, and that is not physical in an adiabatic evolution process. Thus, as the necklace expands, $\omega * R^2$ has to be conserved. Our numerics confirm this prediction. One can also easily develop a moment of inertia formulation for this system. The moment of inertia for necklaces is roughly $I=E*R^2$. Since $L=I\omega$, and both E and L are conserved, ω has to go down with R^2. To our knowledge, this is the first prediction of a "skater on ice" effect, which is so obvious in Newtonian Mechanics, but unobserved yet directly in solitonic systems: the slowing-down of angular velocity due to conservation of energy and angular momentum.

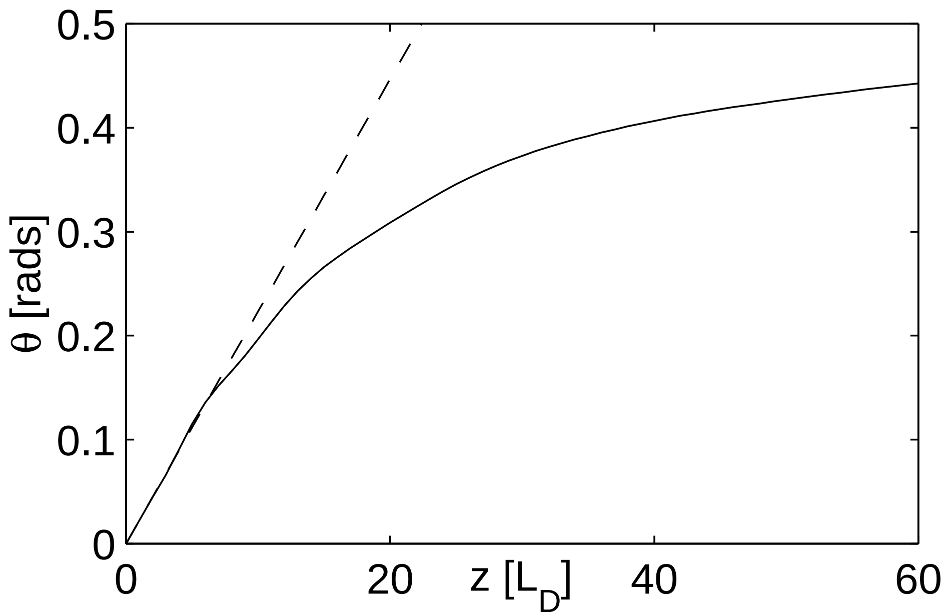

Fig 3.2-2: The rotation angle of the expanding necklace of Fig 3.2-1, as a function of propagation distance, z. This particular necklace expands significantly as it propagates. Since both L and E are conserved, the angular velocity slows down. The solid line represent the true instantaneous angle of rotation of the necklace (as measured numerically at 60 points during the propagation), whereas the dashed line represents what the instantaneous angle of rotation would have been if the angular velocity were a conserved quantity.

3.3. NECKLACES CARRYING NON-INTEGER L/E

As pointed out above, only integer values of L/E are allowed, in an analogy to QM. But we know that there are physical objects that carry spin in multiples of $\hbar/2$ also. However, such spin (e.g., in electrons) is an internal degree of freedom, and cannot be reproduced as a manifestation of a spatial property of a wave function. Nevertheless, even in QM, the expectation value of angular momentum can be a non-integer multiple of $\hbar$. We build on this idea to construct stable self-trapped beams that carry non-integer L/E. The necklaces described above have $\psi(r,\theta,z=0)=f(r)\{\exp(i(\Omega+M)\theta)+\exp(-i(\Omega-M)\theta)\}/2$. To create a necklace carrying non-integer L/E, we launch shapes of the form of $\psi(r,\theta,z=0)=f(r)\{\exp(i(\Omega+M)\theta)+\exp(-i(\Omega)\theta)\}/2$, like in Fig 3.3-1. Such a necklace has L/E=M/2. For an odd M, this necklace has a non-integer L/E! Its intensity is given by $f^2(r)\{1+\cos[(M+2\Omega)\theta]\}/2$. In contrast to the necklaces of chapter 2 that have an even number of spots, a necklace that carries non-integer L/E has an odd number of spots. Furthermore, in a necklace in which L/E is an integer (or zero), adjacent spots are mutually π out of phase (this is why such necklaces expand [8]). Clearly, this can not be the case here since there is an odd number of spots. In order to preserve the symmetry between the pearls, the angular momentum is again manifested in rotation of the necklace, and $\omega=M/(2R^2)$; thus ω is twice slower than for the corresponding necklaces of the previous paragraph, keeping M and other parameters fixed. Our numerics confirm this analytical prediction, and these necklaces seem to be as stable as the usual necklaces: for many tens of L_D's.

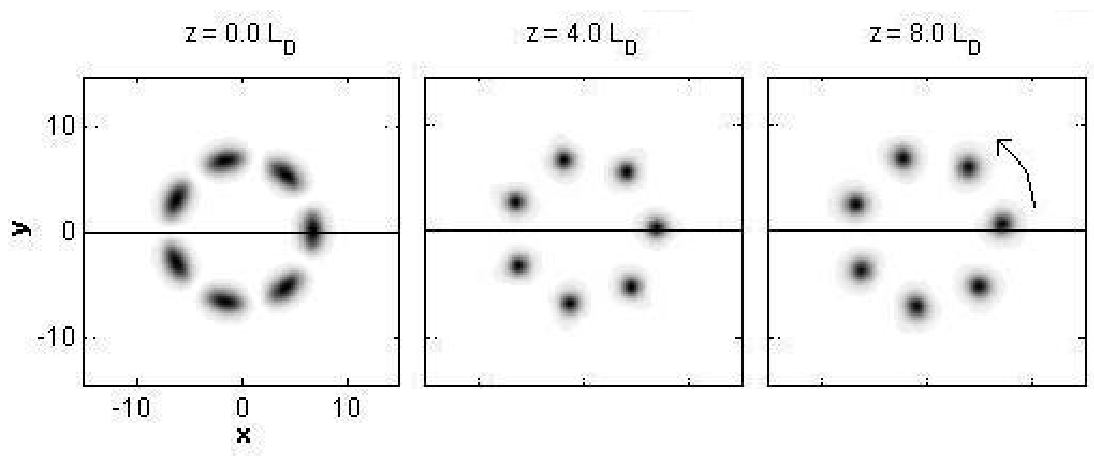

Fig 3.3-1: A necklace with L/E=1/2. We launch a necklace close to the equilibrium self-trapped necklace shape; it "breathes" until it reaches the equilibrium shape (at 3 L_D). As shown here, this necklace slowly rotates as it propagates. The input shape is approximately $\psi(r,\theta,z=0)=\text{sech}(r-6.83)\{\exp(i4\theta)+\exp(-i3\theta)\}/2$.

Another surprising feature of the systems described so far is that a photon, no matter where it is in the beam, carries the same angular momentum [55], although the energy density distribution is so non-uniform! That is, we calculate analytically the local ratio $L(\theta)/E(\theta)$, and find this ratio to be independent of θ, both in the case of the necklace with an even number of pearls (when it equals M), and in the case of a necklace with an odd number of pearls (when it equals M/2). This implies that in a necklace with an odd number of pearls, each photon contributes equally to the total angular momentum, and it contributes with $M\hbar/2$. (One might think that the way we get a non-integer per-photon angular momentum is through the fact that different photons carry different amounts of integer angular momentum with respect to the origin, depending on where they are. But, this is not the case! The photons have identical expectation values of angular momentum.) Since the shape of each pearl is fixed (rigid) as the necklace propagates, each photon (no matter in which part of the necklace it is), has to have the same angular velocity with respect to the center of the necklace.

Finally, we generalize this idea of generating a self-trapped necklace with a non-integer L/E, to a necklace carrying an **arbitrary** real per-photon angular momentum. Consider a necklace of $\psi(r,\theta,z=0) = f(r)$ {a*exp(iMθ) +b*exp(iNθ) + c*exp(-iPθ) + d*exp(-iQθ)}. This necklace has $L/E=(a^2M+b^2N-c^2P-d^2Q)/(a^2+b^2+c^2+d^2)$, which can in principle take **any real value**. Not all such necklaces are stable, but one can construct necklaces that are stable for at least many L_D's. Setting N=P, M and Q to have similar values as N and P, b to be similar to c, and a,d << b,c, the necklace looks like a "usual" necklace (with a radius much larger than its thickness), but with its envelope slightly azimuthally modulated. We know from chapter 2 that small azimuthal perturbations do not destabilize necklaces for long propagation distances. Thus, we expect these necklaces to be stable also, and indeed, we find many such necklaces that are stable for more than $20L_D$, which is plenty for experimental observations. For example, a typically-large experimental propagation distance for (2+1)D spatial solitons observed so far is approximately $20L_D$ [47]. In Fig. 3.3-2, we show a necklace that has d=0, N=P=8, M=15, a=1, b=7, and c=8. Therefore, L/E=-35/38 for this necklace. As can be seen in Fig. 3.3-3, this necklace indeed has a shape similar to a usual necklace, but with a small azimuthal perturbation. It is interesting to note that **in these necklaces the angular momentum is not manifested in rotation of the necklace (!), but instead in circulation of the modulation of the azimuthal envelope**, as shown in Fig 3.3-2; neighboring spots exchange energy and perform a clockwise circulation of energy around the necklace, and this is the primary means of transporting the angular momentum upon the propagating beam. The reason for this distinctly different behavior of a necklace with integer of 1/2 L/E values from a necklace with a non-integer and not 1/2 value of L/E, is symmetry. For the necklace with integer, zero, or 1/2, values of L/E, the symmetry between the pearls is conserved. Thus, if a symmetric necklace is to stay stable, the only way the angular momentum can be manifested in that case is the rotation of the necklace as a whole, as shown in Figs. 3.2-1&3.3-1. In contrast, for a necklace with non-integer (and not 1/2) value of L/E the symmetry between the pearls is broken to start with, as shown in Fig 3.3-2. Thus, the pearls are allowed to exchange energy, and thereby carry the angular momentum without the rotation of the necklace as a whole. Indeed, as shown in Fig. 3.3-2, the frame of the necklace is stationary, yet the spots circulate the energy in a preferential direction corresponding to the sign and the value of L/E.

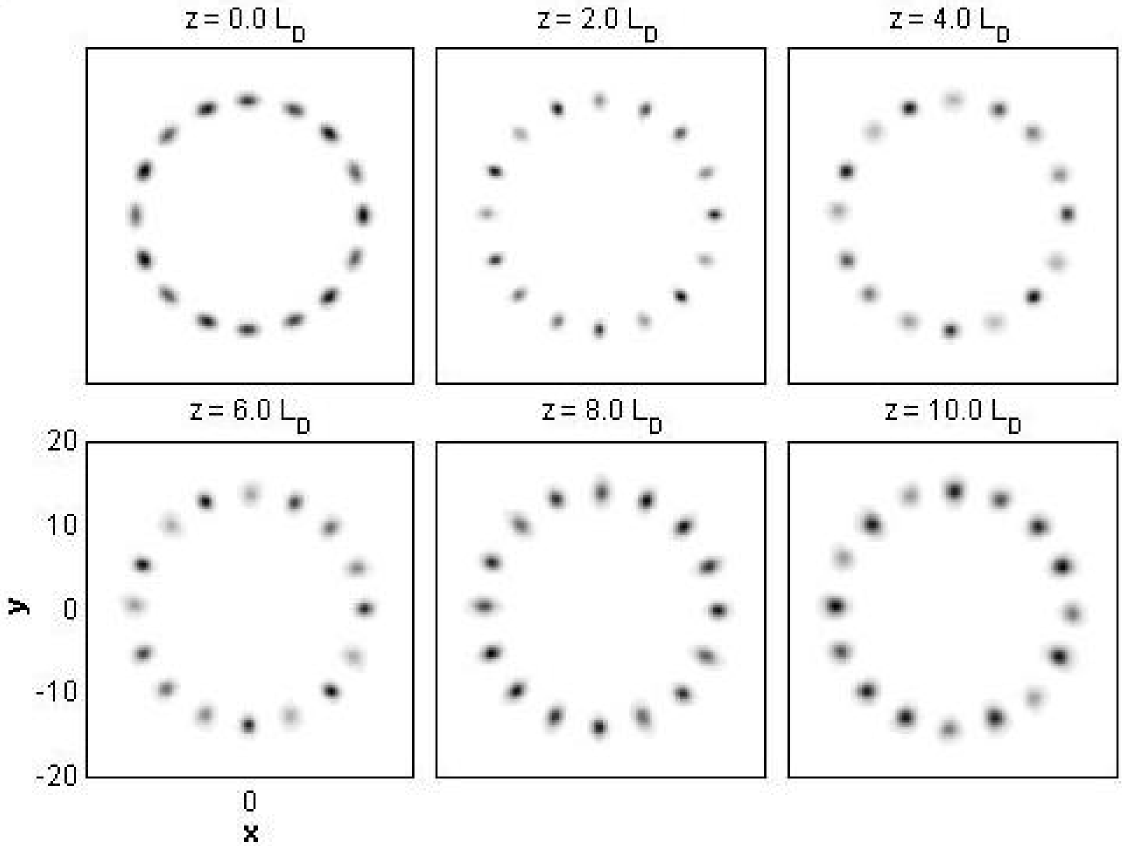

Fig 3.3-2: a necklace with fractional L/E= -35/38. The angular momentum manifests itself in exchange of energy between the spots; this exchange "circulates" around the necklace. Contrast is enhanced for better clarity. This particular necklace is stable only for $8L_D$. Necklaces that have better stability are such that the energy exchange between the spots is slow, so it is not visible in a gray-level figure. For example, one can easily construct a necklace with L/E= 261/ 1634 that is stable (numerically) for at least 50 L_D.

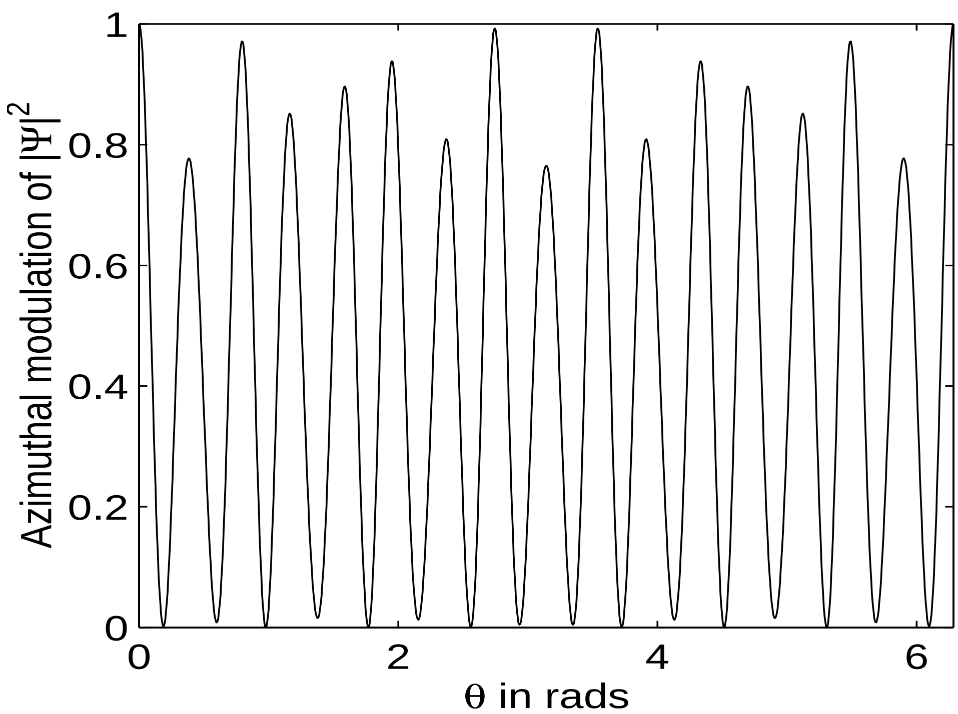

Fig 3.3-3: the azimuthal intensity profile of the necklace from Fig 3.3-2. The input shape was approximately $\psi(r,\theta,z=0)=\text{sech}(r-13.66)\{\exp(i15\theta)+7*\exp(i8\theta)+8*\exp(-i8\theta)\}/16$. Therefore, $|\psi|^2=f(r)Q(\theta)$ at the input; what we plot here is $Q(\theta)$. As can be seen here, the azimuthal profile of this necklace is very similar to the profile of a regular necklace, but with a small azimuthal perturbation. Thus, a necklace like this one is stable for fairly long propagation distances.

The necklace described in Figs. 3.3-2, and 3.3-3 has $L(\theta)/E(\theta)$ which strongly depends on θ. This is easy to understand since in this necklace the pearls are not "rigid" as is the case with the necklaces from Figs. 3.2-1, and 3.3-1; thus photons that are localized in different parts of the necklace can have different angular velocities. Therefore, the non-integer L/E found for these beams does not imply that the angular momentum per photon in them is a non-integer multiple of $\hbar$, because different regions upon the beam carry different angular momentum per photon. This is in sharp contrast with the M/2 case of Fig. 3.3-1 where the angular momentum per photon is indeed M/2 everywhere.

3.4. PERSPECTIVE AND CONCLUSION OF CHAPTER 3

Finally, we emphasize that all necklaces described here are indeed self-trapped. If we start with a shape that is close to the equilibrium necklace shape, as long as this necklace is stable, both L and E are self-trapped to the necklace. The L and E carried away by radiation are negligible compared to the initial L and E values. Furthermore, the self-trapped part of the necklace conserves its initial L/E to even much better accuracy, although a tiny fraction of L and E are carried away through radiation.

To the best of our knowledge the necklaces described here are the only self-trapped shapes found thus far that have a non-integer per-photon angular momentum (in units of $\hbar$). Although our initial motivation (in chapter 2) for constructing necklace beams was to have stable bright self-trapped shapes in (2+1)D cubic NLSE, necklace beams demonstrate interesting physical properties by themselves. Since necklace-like shapes can be most likely constructed in many other non-linear wave-equations, the ideas from this chapter should be extendable to a wide range of physical systems. For example, one might think about converting the fractional angular momentum per particle carried by a necklace with L/E =M/2 into the angular momentum carried by the spin. This will imply rotation of the polarization state in optics, or spin-orbit interaction in a coherent electronic system, such as a Bose-Einstein condensate.

4. FRACTALS FROM SOLITONS

4.1. INTRODUCTION

Fractals are one of the most fundamental concepts in nature [57], characterizing many natural phenomena; they have been described not only in biology, medicine, galactic clusters, material structures, etc., but also in areas as surprising as stock markets [58]. In Optics, Fractals have been identified in conjunction with binary gratings [59] and with unstable cavity modes [60]. Both of these optical fractal systems are fully linear; they respond in a passive manner to illumination by constructing fractals through linear diffraction. In this chapter, we show that nonlinear systems that support solitons can, under proper non-adiabatic conditions, **evolve** and give rise to statistical fractals. Further, our idea can be used to demonstrate exact fractals as well. The principle we describe is universal and seems to hold for most soliton-supporting systems in nature. Just as an illustration of our idea, we present some specific examples that theoretically demonstrate fractals in nonlinear optics. In addition, we discuss possible experimental realizations.

As an example of a soliton-supporting system, consider a system described by the normalized Nonlinear Schrodinger Equation (NLSE:)

$$i\frac{\partial\Psi}{\partial z}+\frac{1}{2}\nabla_T^2\Psi+f(|\Psi|^2)\Psi=0 \qquad (4.1\text{-}1)$$

where the nonlinear term $f(|\Psi|^2)$ is specific to the physical system, and ∇_T^2 is the Laplacian transverse to the propagation direction z. For waves in a single transverse dimension [(1+1)D NLSE], $\nabla_T^2=\partial^2/\partial x^2$. Equation (4.1-1) describes many physical systems, primarily those in which nonlinear waves propagate in isotropic media [4], where Ψ describes the slowly varying envelope that modulates a fast carrier wave. In particular, NLSE describes several optical systems [61,1,5], where Ψ is the slowly varying amplitude of the electric field, superimposed on an single **k** vector carrier plane wave. In our theoretical studies, we focus on the (1+1)D NLSE and on two particular forms of nonlinearity that are common in optics [1,5]: the Kerr-type where $f(|\Psi|^2) = |\Psi|^2$, and the saturable type where $f(|\Psi|^2) = |\Psi|^2/(1+|\Psi|^2)$. Extending our ideas to other forms of nonlinearities is straightforward, and extending them to higher dimensions maintains the main results while adding beauty and complexity to the fractals generated. The particular systems we discuss are just examples of the general principle we propose.

Since $df(|\Psi|^2)/d|\Psi|^2 > 0$, both the Kerr, and the saturable nonlinearity are of the self-focusing type, i.e., the nonlinearity has a tendency to shrink a pulse. In optical systems, this happens because the presence of the light pulse increases the local index of refraction, which, in turn, tends to shrink the pulse. The tendency to shrink competes with diffraction, which tries to expand the pulse, and, for some NLSEs, these two tendencies can exactly cancel each other, producing a localized pulse whose shape is stationary as it propagates: a soliton [62]. The solitons of the particular NLSEs we discuss in this chapter are very robust creatures. Even if one perturbs them slightly from their equilibrium shape, they soon evolve into stable solitons again.

In section 4.2, we provide some background intuition that contributes to the understanding of our idea. In section 4.3, we describe our idea. In section 4.4, we put our idea in perspective of what is already known, and what is yet to be done. In section 4.5, we describe how our idea can be used to create exact fractals also. In section 4.6, we discuss experiments with fractals in photorefractive materials, and in section 4.7, we conclude this chapter. Material presented in section 4.5 appeared in [32], while the rest of material was published in [31,63]; material from section 4.6 was not published.

4.2. INVARIANCE ACROSS THE SCALES

Consider first the (1+1)D Kerr NLSE, of which a fundamental soliton solution is $\Psi(x,z)$. One can obtain a whole family of solitons of Eq. (4.1-1) by a simple re-scaling: $\Psi(x,z) \to q\Psi(qx,q^2 z)$ for any real q. According to the definition of self-similarity, this means that all solitons of the same order of this equation are self-similar to each other [64]. This property, in fact, holds for solitons of any order N: if Ψ(x,z=0) is a soliton of order 1, then NΨ(x,z=0) is a soliton of order N. Furthermore, because the generic waveform of solitons of all orders is hyperbolic secant, then solitons of different orders are also self-similar to one another, at least at some points in their propagation (although their propagation dynamics differs from one order to another). The physical basis for this self-similarity is the fact that the (1+1)D Kerr NLSE does not have any natural scale built into it, so the physics of this equation looks the same on all scales.

In contrast with the Kerr nonlinearity, the (1+1)D saturable NLSE does have a natural scale, given by the number 1 in the denominator of the nonlinear term. However, for $|\Psi|^2 << 1$, the nonlinearity reduces to the Kerr nonlinearity, so self-similarity exists in the saturable case also. Furthermore, if a soliton of (1+1)D saturable NLSE satisfies $|\Psi(x=0,z)|^2 >> 1$ in the regions where most of the energy of the soliton is contained, $|\Psi|^2/(1+|\Psi|^2) \approx 1-(1/|\Psi|^2)$. Of course, this approximation does not hold at the tails of the soliton. Still, most of the interesting properties can be captured by studying (1+1)D NLSE with a nonlinearity given by $1-(1/|\Psi|^2)$; we call this nonlinearity the “deep-saturation nonlinearity”. We have checked numerically that if the condition $|\Psi(x=0,z)|^2 >> 1$ is satisfied, then indeed most of the soliton’s physics is captured by studying the (1+1)D Deep-saturation NLSE. If $\Psi(x,z)$ is a solution of the (1+1)D deep-saturation NLSE, then a whole family of solutions can be obtained by re-scaling $\Psi(x,z) \to e^{iz(1-q^2)}\Psi(qx,q^2z)/q$, for any real q. Therefore, all solitons of the same order of (1+1)D saturable NLSE are related by this simple re-scaling, as long as most of the energy of the solitons is in the regions where $|\Psi|^2 >> 1$; all of these solitons are self-similar to one another in their physical properties, such as intensity shape etc. This is because the natural scale in the saturable NLSE is visible only in the margins of the intensity profile of the soliton, and its effect on the shape is tiny.

We now introduce the concept of the soliton existence curve [65], a two-dimensional curve that gives the FWHM of the soliton intensity in normalized units, as a function of the peak amplitude of the corresponding soliton, $\Psi_0 \equiv \Psi(x=0,z)$. The curve is drawn for the set of all solitons of the same order of a given NLSE, where each soliton is represented by a point on the graph. Different NLSEs have different existence curves, and solitons of different orders of the same NLSE lie on different existence curves. According to the scaling relation described above, all existence curves (of solitons of all orders) of Kerr NLSEs are parallel lines of slope -1 on a log-log plot. The existence curves of saturable NLSEs are also parallel lines of slope -1 on a log-log plot (which coincide with the Kerr curves) in the region $\Psi_0 << 1$. On the other hand, in deep-saturation where $\Psi_0 >> 1$, the existence curves are parallel lines of slope 1 on a log-log plot like in Fig. 4.2-1. The region in between these two regimes, i.e., where $\Psi_0 \sim 1$, we call the valley. All solitons of the same order of a saturable NLSE are to a large extent self-similar to each other as long as they are all on the same side of the valley.

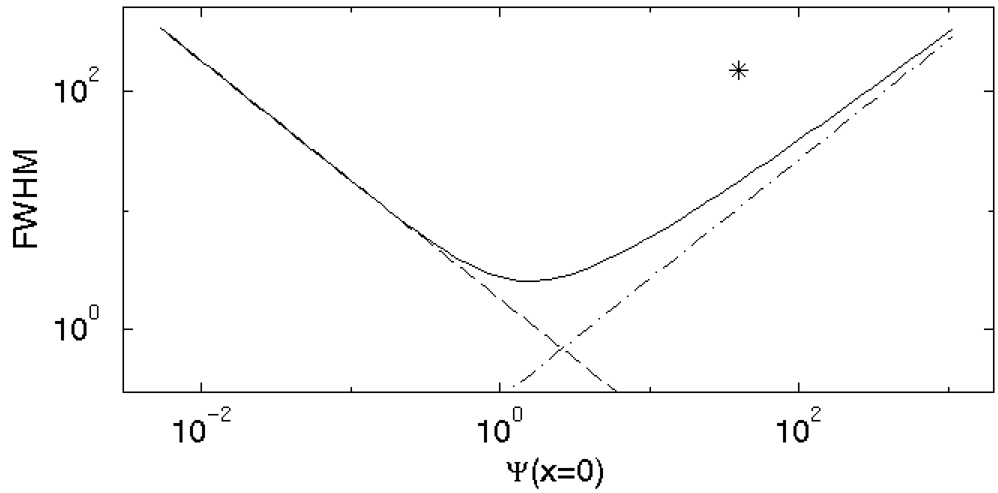

Figure 4.2-1: Existence Curves of Kerr-type solitons (dashed line), solitons in a saturable nonlinear medium (solid curve), and deep-saturation solitons (dashed-dotted line), all in (1+1) D. The vertical axis gives the normalized width of the intensity of the soliton, in the *x*-units of Eq. (4.1-1). The point indicated by * describes the input pulse to the fractal-generating process of Fig. 4.3-2.

The existence curves can provide information about the evolution of arbitrary input pulses into solitons. Consider a pulse of width w and peak amplitude Ψ_0, and assume that this pulse does not have the stationary soliton shape. This pulse is represented by a point with coordinates (Ψ_o,w) on the existence curve plot. If this point is close to the curve, then the pulse soon evolves into a stable soliton shape (while shedding some power in the form of radiation modes or smaller scale solitons). Since the solitons of the NLSEs we study here are stable, this happens even though their initial shape only approximates a soliton.

4.3. OUR IDEA ON HOW TO OBSERVE FRACTALS

Having established that Kerr solitons are exactly self-similar, and that deep-saturation solitons are approximately self-similar, it is now compelling to ask: "Can solitons of various scales coexist in the same nonlinear medium simultaneously?" If the answer is positive, can they coexist within one another in a fractal structure? And, if the answer to this question is also positive, then how can a nonlinear system be driven to generate solitons organized in a fractal structure? The answers to all of these questions are in the response of the nonlinear system to a non-adiabatic change in one (or more) of its properties. As described below, an abrupt change in the nonlinear coefficient, or in the saturation coefficient (in saturable systems), or in the dispersion coefficient (for temporal solitons), or in almost any parameter that leads to a large deviation of the pulse from the soliton existence curve, will lead to the appearance of a fractal structure driven by soliton dynamics. In our simulations, we observe self-similarity and fractals both in the Kerr regime, and in the deep-saturation regime of Eq. (4.1-1).

Our goal is to design a physical system that can support many solitons all of different sizes simultaneously. If one starts with a pulse whose shape is very far off the existence curve, this pulse is not able to evolve smoothly into a soliton. Under proper conditions, it breaks up into smaller pieces and radiation. Quite often, the pieces resulting from this "explosion" include many small solitons, all of different sizes. If the nonlinearity is such that these solitons are self-similar to each other, one can claim to have observed self-similarity.

We distinguish between two scenarios that produce such breakup. The first is driven by noise and is easier to realize experimentally. Consider a pulse whose initial width is far above the existence curve launched into a nonlinear medium in the regime that can support self-similar solitons (as in Fig. 4.2-1). Therefore, small perturbations (initiated by noise) of large wavelengths will grow on top of the pulse as it propagates. After some distance, the energy in these perturbations becomes significant, and the pulse breaks up into smaller pulses. This phenomena is known [61] as Modulational Instability (MI). In many physical systems, the products of this breakup include many solitons of different sizes. We call it “MI-induced breakup”. An example of such a breakup in saturable NLSE is given in Figure 4.3-1.

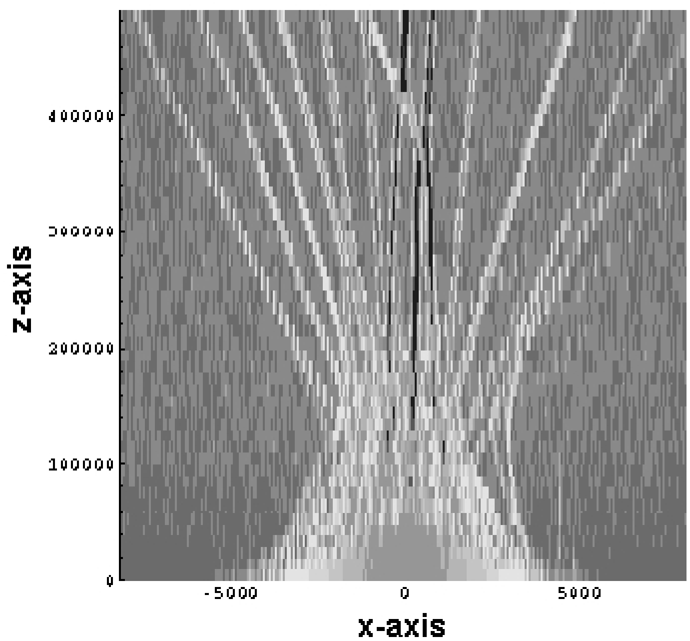

Figure 4.3-1: An example of an MI driven breakup, starting in the deep-saturation regime of (1+1)D saturable NLSE. The initial pulse was 80 times wider than the soliton of the same peak amplitude, and there was a significant amount of background noise.

The second breakup scenario is "Dynamics-induced breakup". It is observable in numerical calculations that inherently have no or very little noise. It is also observable in “clean” experimental systems, like temporal solitons in optical fibers [81]. Consider a pulse above the existence curve launched into a self-focusing medium. The local intensity increases the local index of refraction, thereby creating a waveguide structure that attracts light to the center of the induced waveguide. If the initial width of the pulse is much larger than the width of the lowest guided mode of this induced waveguide, the light coalesces towards the center trying to reach the solitonic shape, in which diffraction is exactly balanced by self-focusing. However, once the equilibrium is reached the pulse keeps shrinking because of its inertia. Since the equilibrium could not have been reached smoothly (the pulse is initially far above the existence curve), the pulse explodes into smaller pieces, which form smaller solitons of different sizes. For an example in saturable NLSE, please see the top plot of Fig. 4.3-2. Since both the underlying equation and the initial pulse obey left-right symmetry, the output multi-soliton pulses also obey this symmetry (in contrast with an MI-induced breakup, since noise obeys no symmetry). At any rate, Fig. 4.3-1, and the top plot in Fig. 4.3-2 clearly demonstrate self-similarity in systems that allow for existence of solitons.

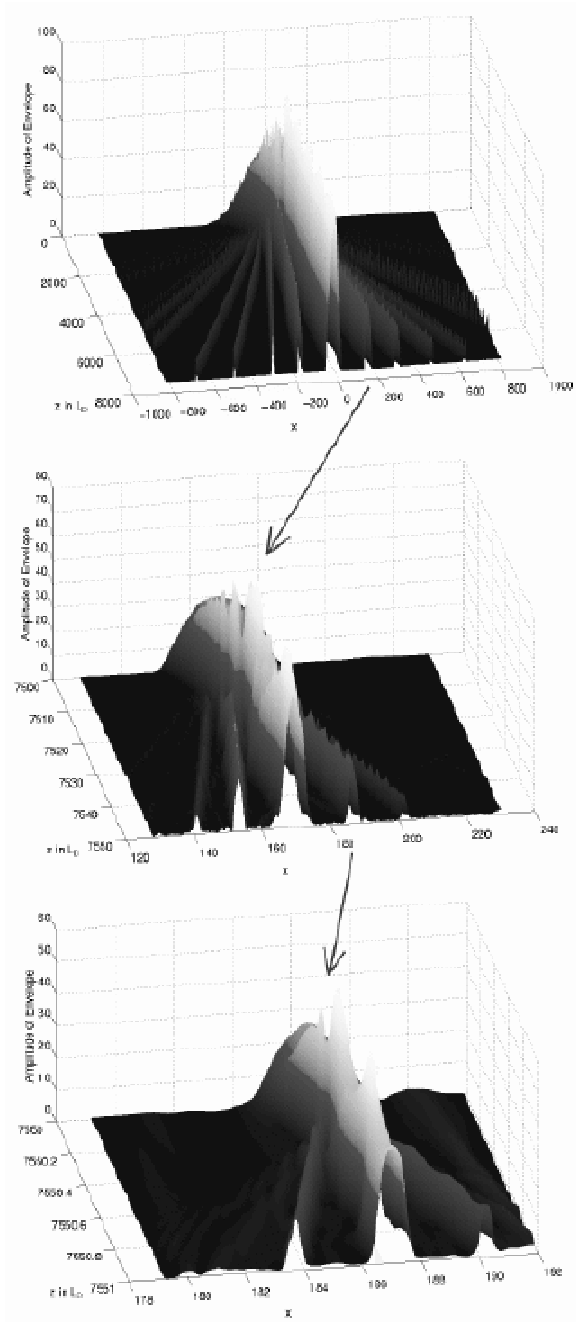

Figure 4.3-2: A 3-stage self-similar dynamics-driven breakup creating a fractal structure **starting** in the deep-saturation regime of the (1+1)D saturable NLSE. The initial pulse is given by point * in Fig. 4.2-1. The 1st stage is given in the top plot. A detail of the 2nd stage is given in the middle plot. Finally, a detail of the 3rd stage is given in the bottom plot.

In order to create fractals, one can apply the logic that has caused such breakups in a repetitive manner. The breakups into self-similar solitons were caused by an abrupt change from a medium in which the input pulse was stable into a second medium that tried to force the pulse to be much narrower. In the above examples, the initial medium is free space and the second medium is a self-focusing medium that supports solitons that are much narrower than the input pulse, when both have the same peak intensity. The same logic can be applied when the initial medium is nonlinear, when the abrupt transition is from a medium in which the input pulse is a stable soliton into a medium that breaks it up into much narrower solitons. In other words, if after the abrupt transition, the pulse is much wider than the soliton of the same intensity (i.e., the pulse is far above the existence curve), it cannot evolve smoothly into a single soliton. Instead, it explodes into solitons of different scales. In this spirit one can take the output "daughter solitons" at the end of the top plot in Fig. 4.3-2, and make an abrupt change in the nonlinear medium in which they propagate, and force each one of the "daughter solitons" to break up into a train of smaller solitons. This happens if the change moves the position of the "daughter-solitons" far above the existence curve. Such a change in the nonlinear medium can be realized either by altering the intensity of the pulses abruptly, or by changing the coefficient in front of ∇_T^2 in Eq. (4.1-1), or by changing the properties of the nonlinearity (magnitude, saturation, etc.). It is important that the change in the conditions is abrupt; an adiabatic change does not cause a breakup, but instead the pulse adapts and evolves smoothly into a narrower soliton, as shown in Fig. 4.3-4. When the change is abrupt and large enough, each of the pulses undergoes a self-similar breakup as illustrated in the middle plot of Fig. 4.3-2, or top plot of Fig. 4.3-3. This process can be repeated, in principle, an infinite number of times, thereby creating a fractal structure. Of course, all the resulting solitons after each breakup have to be in the regime where they are all self-similar to each other.

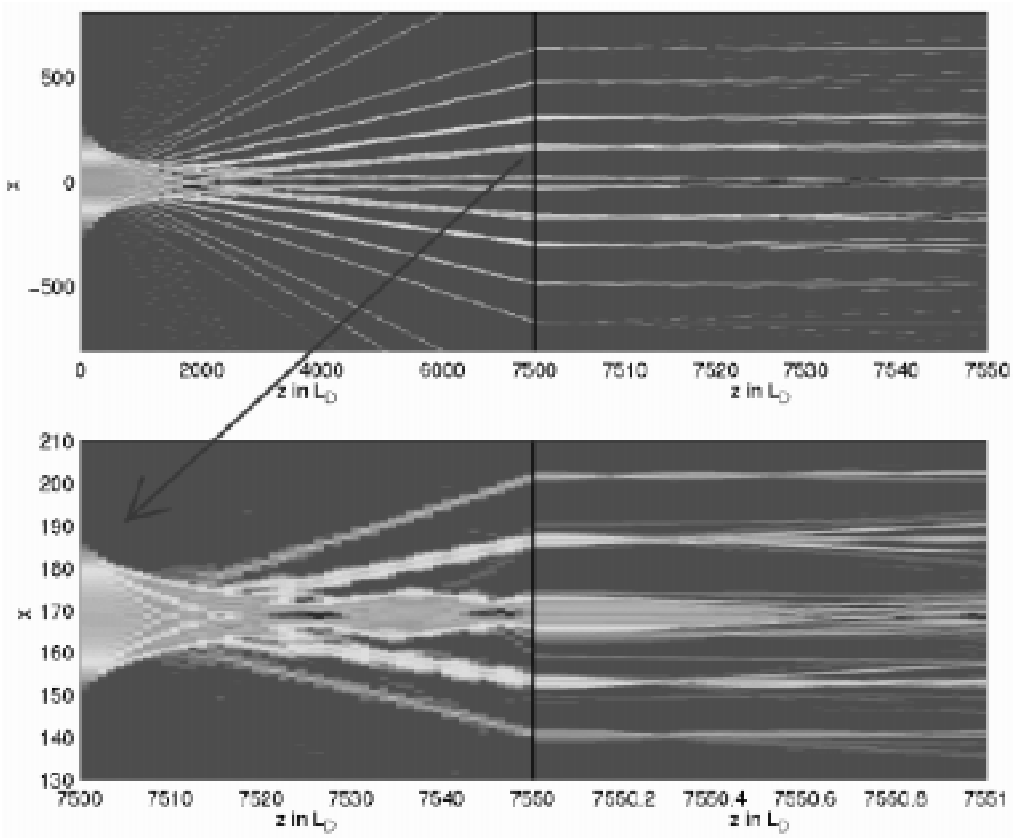

Figure 4.3-3: Top view of a 3-stage self-similar breakup creating a fractal structure **starting** in the deep-saturation regime of the (1+1)D saturable NLSE. The 1st stage is given in the upper-left plot. The 2nd stage is given in the upper-right plot. A magnified detail of the 2nd stage is shown in the lower-left plot. The continuation of evolution of that detail into the 3rd stage is given in the lower-right plot.

A three stage fractal is presented in Figs. 4.3-2, and 4.3-3. These breakups are dynamics-induced. At the input, self-focusing is much stronger than diffraction for a pulse of that width, so the pulse contracts and eventually breaks up into many self-similar solitons observed at the output of the upper-left figure. At the plane of the output of the upper-left figure, we change the denominator in the nonlinear term from $1+|\psi|^2$ to $1+(|\psi|^2/8)$. This makes all the pulses at the output of the upper-left figure have amplitude 8 times smaller than solitons of the same widths have. Then, we propagate the output of the upper-left figure for a few more diffraction lengths, resulting in a self-similar breakup of every pulse, as shown in the middle plot of Fig 4.3-2. At the output of the middle plot of Fig. 4.3-2, we change the nonlinear term into $1+(|\psi|^2/64)$, and propagate the pulse further. As shown in the bottom plot of Fig. 4.3-2, we observe one more stage of self-similar breakup. In these simulations, we use the saturable $\frac{|\psi|^2}{1+|\psi|^2}$ nonlinearity, to show when we expect the fractal generation process to end in a real system. In this case, the third stage shown by bottom plot is the final breakup, because most of the end solitons at this stage are of peak intensities on the order of unity, which cease to be self-similar. As for the other end of this process, i.e., the first breakup, there is no upper limit: one can start this fractal generation process by literally breaking up plane waves.

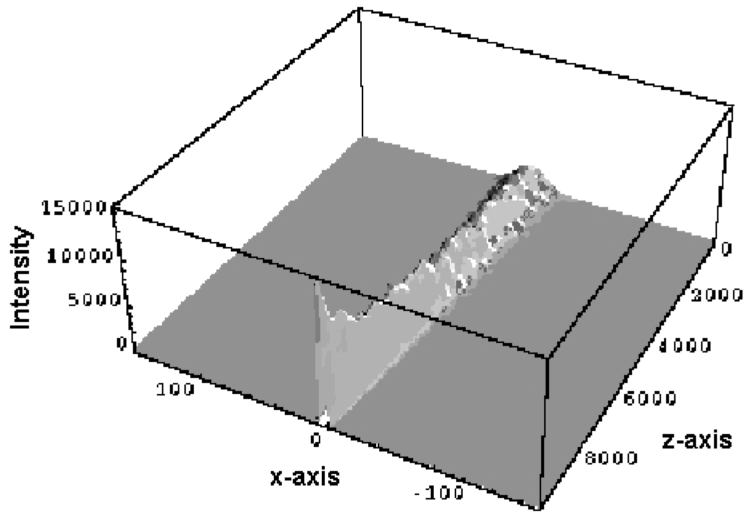

Figure 4.3-4: An adiabatic change of the physical system in which the pulse propagates does not cause the required breakup. We start with a pulse that is initially a soliton of the (1+1)D cubic NLSE, and vary the saturation coefficient **adiabatically** (i.e. the characteristic propagation length scale on which the coefficient varies is much longer than the characteristic length scale of the pulse propagation given by the diffraction length of the pulse at any given moment.) Instead of breaking up, the soliton keeps evolving smoothly into whatever the instantaneous solitonic shape is. Physically this is expected because solitons of (1+1)D cubic NLSE are very stable creatures.

To have a real fractal in mathematical sense, one should have an infinite number of stages in this process. However, as is the case with all other physical fractals, the number of stages is limited, thus resulting in a pre-fractal, rather than a fractal. The reason why all physical fractals live in only a limited regime of scales is easy to understand. Both at large, but primarily at small scales, sooner or later the scale of the fractal in question becomes comparable to some other relevant physical scale. Such scale then modifies the physics of the system, and the equation representing the system is modified, typically to an equation that does not display self-similarity anymore. For example, at small scales, at least the atomic scale presents a lower bound to fractal generation. Specifically for optical spatial solitons, the number of breakup stages is limited by the ratio between the beam width (of any of the daughters solitons in a particular stage) and the optical wavelength in the medium. When this ratio is smaller than, say, 5, the beam is no longer paraxial and one has to add other terms to the equation (and for ratio ~1 the underlying equation becomes vectorial). For optical temporal solitons in fibers, the limiting factors are third order dispersion, and additional nonlinear processes (e.g., Raman scattering). In both cases, we realistically expect to observe 3-4 stages of breakup.

Let us go back now to the definition of a fractal [58] as "an object which appears self-similar under varying degrees of magnification. In effect, possessing symmetry across scale, with each small part replicating the structure of the whole". It is obvious that the structures described in Fig. 4.3-2 are fractals: they are self-similar **within** each scale (i.e., the "daughter solitons" after each breakup), and they are also self-similar over at least three widely separated scales. Also, as we show by the increasing magnification (Fig. 4.3-2), each part breaks up again and again in a structure replicating the whole. It is obvious that we have found a way to generate fractals, which are driven by soliton dynamics.

4.4. PERSPECTIVE

Several topics merit discussion. We want to emphasize the resemblance of our fractals to Cantor Sets [58]. This fractal structure (after several breakup processes) is actually a ***Randomized Cantor Set***, because at any given stage self-similar structures (soliton-like pulses) of various scales coexist, with the distances between these pulses varying in what looks like a random manner, especially in the presence of significant noise. Furthermore, the process we described is pretty robust; in our simulations we did not have to be particularly careful about when to start each particular stage in order for our final creatures to be fractals. The presence of the noise does not harm the fractal generation either; in fact, as we explained above, one can use this idea to build random fractals that are in fact **noise-driven**. This brings in another point: the **fractal dimensions**. The fractal dimension can be estimated using box-counting method, and it is obvious that this dimension is (in general) not an integer. In any case, the fractal dimension is specific to the system and the initial conditions used. Another topic has to do with **fractals in higher Euclidian dimensions**, e.g., in full 3D. Since *the ideas presented are not restricted by dimensionality,* they should be easy to translate into higher dimensions and we envision fractals that have two different transverse scales, that is, when the width of every pulse in x is much different than that in y. However, caution must be taken to make sure that the system can support (2+1)D soliton structures first. The saturable NLSE can support stable bright (2+1)D solitons [66], so we expect it to support 2D fractals as well. There are many other new ideas under research, but the main challenge is experimental: to demonstrate fractals.

4.5. EXACT FRACTALS FROM SOLITONS

4.5.1. Introduction

Fractals can be classified in numerous manners, of which one stands out rather distinctly: **Exact** (regular) **Fractals** versus **Statistical** (random) **Fractals**. An exact fractal is an "object which appears self-similar under varying degrees of magnification … in effect, possessing symmetry across scale, with each small part replicating the structure of the whole" [58]. Taken literally, when the same object replicates itself on successively smaller (or larger) scales, even though the number of scales in the physical world is never infinite, we call this object an "**exact fractal**". When, on the other hand, the object replicates itself in its statistical properties only, it is defined as a "**statistical fractal**". Statistical fractals have been observed in many physical systems, ranging from material structures [e.g., polymers, aggregation, interfaces, etc.], to biology, medicine, electric circuits, computer interconnects, galactic clusters, and many other non-related and surprising areas, including stock market price fluctuations [58]. Exact fractals, on the other hand, such as the Cantor Set, occur rarely in nature except as mathematical constructs. In this section 4.5, we describe how a Cantor Set of exact fractals can be constructed, under proper nonadiabatic conditions, in systems described by the (1+1)D cubic self-focusing Non-Linear Schroedinger Equation (NLSE). We demonstrate exact Cantor Set fractals of temporal light pulses in a sequence of nonlinear optical fibers. We calculate their fractal similarity dimensions and explain how these results can be produced experimentally. This work was done in collaboration with Suzanne Sears et al. [32].

A Cantor Set is best characterized by describing its generation [58]. Starting with a single line segment, the middle third is removed to leave behind two line segments, each with length one third of the original. From each of these line segments, the middle third is again removed, and so on, ad infinitum. At every stage of the process, the result is ***self-similar*** to the previous stage; i.e., identical upon rescaling. This "triplet set" is not the only possible Cantor Set: in general, any arbitrary "cascaded" removal of portions of the line segment may form the repetitive structure.

The fractals we propose should be observable in many systems in nature, and their existence depends on two requirements: (I) the system does not possess a natural length scale, i.e., the physics is the same on all scales (or, any natural scale is invisible in the parameter range of interest) and (II) the system undergoes abrupt, non-adiabatic changes in at least one of its properties (as seen in section 4.3).

In the most general case, our method of generating fractals from solitons gives rise to statistical fractals. In the fractal which results from each breakup, the amplitudes of the individual solitons, the distances between them, and their relation to the solitons of a different "layer" are random. Thus, the self-similarity between the structures at different scales is only in their statistical properties. In this section, we show that the principle of "fractals from solitons" can be applied to create Exact (regular) fractals, in the form of an exact Cantor Set. The underlying requirement is that after every breakup stage, all of the "daughter pulses" must be identical to one another. In this case, **ALL** the daughter pulses can be rescaled from one breakup stage to the next by the same constant, and the entire propagation dynamics repeats itself in an exact rescaled fashion. Additionally, if we prepare a sequence of breakups in which the scaling constant between each successive breakup is the same, then the cascade of breakups will create solitons in precisely self-similar formation. The resulting scaling on all length scales constitutes an exact Cantor Set. (Recall that in an exact Cantor Set fractal, all the re-scaled structure must have the same scaling constant between every pair of consecutive stages). **We show below that in this manner, one can obtain exact Cantor Set fractals from solitons**. This represents one of the rare examples of a physical system that supports Exact (regular), as opposed to Statistical (random) fractals [58].

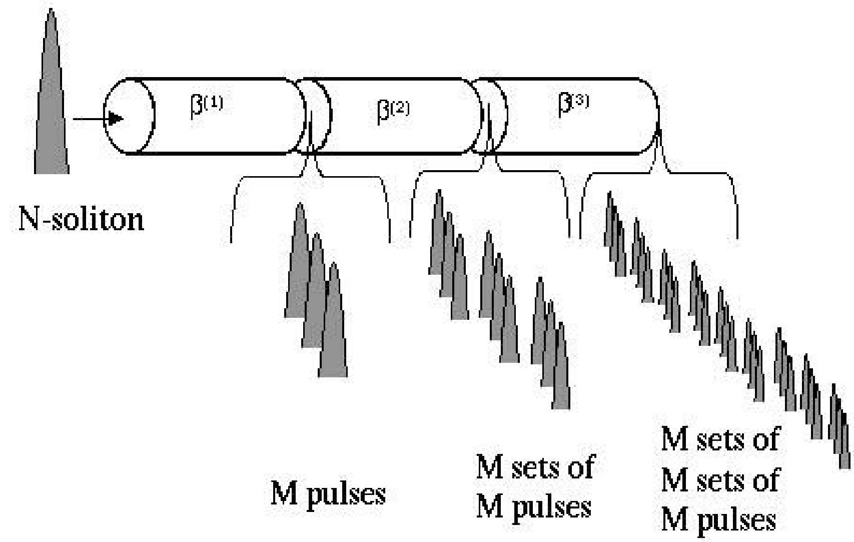

Figure 4.5-1: Illustration of a sequence of nonlinear optical fiber segments with their dispersion constants and lengths specifically chosen to generate exact Cantor Set fractals.

To illustrate the idea of generating Cantor Set fractals from solitons, we analyze the propagation of a temporal optical pulse in a sequence of nonlinear fiber stages with dispersion coefficients and lengths specifically chosen to impose a constant rescaling factor between consecutive breakup products. We numerically solve the (1+1)D cubic self-focusing NLSE, vary the dispersion coefficient in a manner designed to generate Doublet- and Quadruplet- Cantor Set fractals, and show the formation of temporal optical soliton Cantor Set fractals (see Fig. 4.5-1).

4.5.2. Theoretical description of the process

The nonlinear propagation and breakup process in fiber segment "i" is described by the (1+1)D self-focusing cubic NLSE:

$$i\frac{\partial\psi}{\partial z} - \frac{\beta^{(i)}}{2}\frac{\partial^2\psi}{\partial T^2} + \gamma|\psi|^2\psi = 0 \ , \qquad (4.5\text{-}1)$$

where $\psi(z,T)$ is the slowly varying electric field envelope of the optical pulse, $T = t - z/v_g$, is the time coordinate shifted to the propagation frame, v_g is the group velocity, $\beta^{(i)}<0$ the (anomalous) group velocity dispersion coefficient of fiber segment i, and $\gamma>0$ is proportional to the fiber nonlinearity ($n_2>0$); z is the spatial variable along the direction of propagation and t is time. Equation 4.5-1 has a fundamental soliton solution of the form:

$$\psi(z,T) = \sqrt{\frac{|\beta^{(i)}|}{\gamma (T_0^{(i)})^2}}\, Sech\ \left(T/T_0^{(i)}\right) Exp[iz|\beta^{(i)}|/(2(T_0^{(i)})^2)], \qquad (4.5\text{-}2)$$

where, 1.76274 $T_0^{(i)}$ is the temporal full width half maximum of $|\psi(z,T)|^2$, and $z_0^{(i)} = \pi(T_0^{(i)})^2/(2|\beta^{(i)}|)$ is the soliton period for fiber segment i. The N-order soliton (at z=0) of Eq.(4.5-1) can be obtained by multiplying $\psi(z,T=0)$ from Eq.(4.5-2) by a factor of N. A higher order soliton of a given N>1 propagates in a periodic fashion. In the first half of the soliton period ($z_0^{(i)}/2$), the pulse splits into two pulses, then into three, then into four, etc. up to N - 1 pulses [61]. In the second half of the period the process reverses itself until all the pulses have recombined into a single pulse identical to the original one. While attempting to generate Cantor Set fractals from solitons, we observed that, if we start with an N-order soliton, it splits into M<N pulses, each of which reaches an approximately hyperbolic secant shape. Furthermore, there is always a region in the evolution where all the M "daughter-pulses" are almost fully

identical and possess the same height. The breakup can be reproduced if we cut the fiber at this point and couple the pulses into a new fiber with a dispersion coefficient chosen such that each of the pulses launched into the second fiber is an N-order soliton. Each of the daughter-pulses generated in the first fiber exactly replicates the breakup of the "mother-soliton", on a smaller scale. Because the physics of Eq.(4.5-1) is the same on all scales, the entire 2nd breakup process of each daughter-pulse is a rescaled replica of the initial mother-pulse breakup. In fact, we can redefine the coordinates in the second fiber by simple rescaling, so that in the new coordinates the equation is identical to the equation (including all coefficients) describing the pulse dynamics in the first fiber. In this manner, we can continue the process recursively many times, resulting in an exact fractal structure that reproduces, on successively smaller scales, not only the final "product" (the pulses emerging from each fiber segment), but also the entire breakup evolution.

What remains to be specified is how we choose the sequence of fibers and the relations between their dispersion coefficients and lengths. Consider a sequence of fibers in which the ratio between the dispersion coefficients of every pair of consecutive segments is fixed $\beta^{(i+1)}/\beta^{(i)} = \eta$, where η is real and smaller than unity. This implies that the periods of the fundamental solitons in consecutive segments are related through $z_0^{(i+1)}/z_0^{(i)} = [\left(T_0^{(i+1)}\right)^2/\left(T_0^{(i)}\right)^2][1/\eta]$.

4.5.3. Numerical simulations

Numerically, we launch an N-order soliton into the first fiber segment and let it propagate until it breaks into M hyperbolic-secant-like pulses of almost identical heights and widths. At this location we terminate the first fiber section. We label the distance propagated in the first fiber segment $L^{(1)}$. From the simulations we find the peak power $P_M^{(1)}$ and the temporal width $T_M^{(1)}$ of the M almost-identical pulses emerging from the first segment. The M pulses are then launched into the second segment. Our goal is to have, in the second segment, a rescaled replica of the evolution in the first segment. To achieve this, we require that each of these M pulses will become an N-order soliton in the second segment. Thus we equate the peak power in each of the M pulses in the first fiber to the peak power of an N-order soliton in the second fiber:

$$P_M^{(1)} = P_N^{(2)} = \frac{\left|\beta^{(2)}\right|}{\gamma (T_0^{(2)})^2} N^2, \qquad (4.5\text{-}3)$$

where $T_M^{(1)} = T_0^{(2)}$ since it is the width of the input pulse to the second fiber. From Eq. (4.5-3) we find the dispersion coefficient in the second fiber, $\beta^{(2)}$. The ratio η between the dispersion coefficients in consecutive fibers determines the scaling of the similarity transformation. Using η and $T_0^{(2)}$ we calculate the period, $z_0^{(2)}$. Requiring that the evolution in the second fiber is a rescaled replica of that in the first fiber, we get $L^{(2)} / z_0^{(2)} = L^{(1)} / z_0^{(1)}$. Each of the M pulses in the second fiber exactly reproduces the dynamics of the original soliton in the first fiber but on a smaller scale. At the end of the second stage, each of the M pulses transforms into M pulses, resulting in M sets of M pulses. The logic used to calculate the second stage parameters is used repeatedly to create many successive stages, each producing a factor of M pulses more than the previous stage.

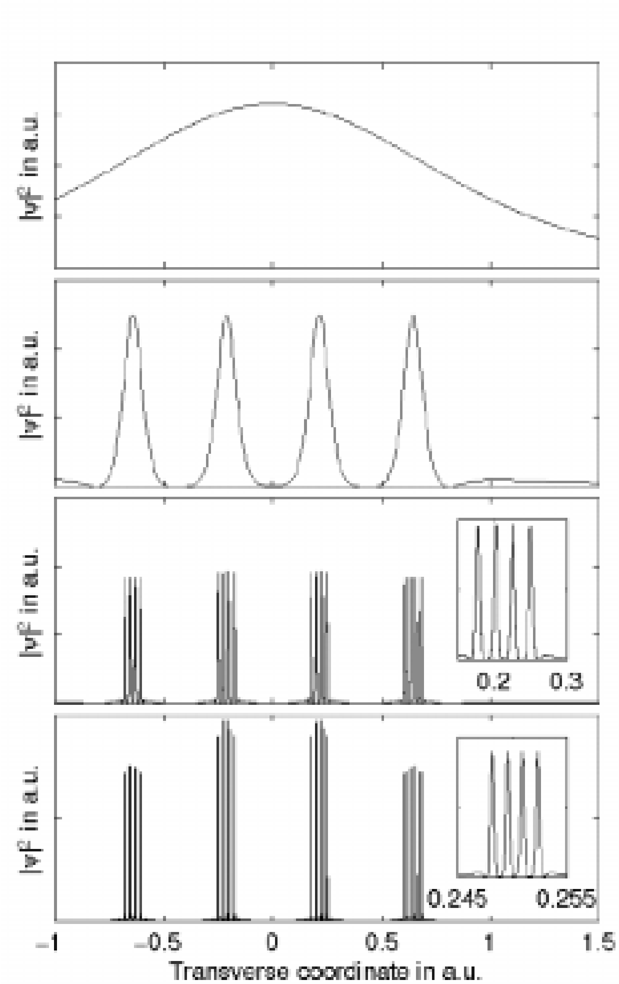

Figure 4.5-2: The figure represent exact (regular) Cantor set fractal generation for a particular case in the (1+1)D cubic self-focusing NLSE. We start with a sech-shaped pulse that is significantly higher than the soliton of the same width, as shown in the first row. The pulse starts breaking up, as shown in the second row. When it acquires the shape depicted in the second row, we abruptly significantly decrease the dispersion coefficient in the underlying equation. This induces the second stage of the breakup and results in the shape shown in the third row. Then, once again we decrease the diffraction coefficient abruptly, and induce the third stage of the breakup shown in the fourth row. In some cases, the pulses were too tiny to see at the given magnification, so the insets in the plots show magnified details of their corresponding plots.

We provide examples of Cantor Set fractals from solitons by numerically solving Eq.(4.5-1). The order of the soliton used and the fraction of a soliton period propagated vary depending on the desired number of pulses, M. Figure 4.5-2 shows a Quadruplet Cantor Set fractal. We launch an N=8 soliton into the first fiber characterized by γ =1 and $\beta^{(1)}$ = -1 and let it propagate for 0.1261 $z_0^{(1)}$. At this point the pulse has separated into four nearly identical hyperbolic secant shaped pulses. We launch the emerging four pulses into the next fiber, characterized by $\beta^{(2)}$ = -0.01285 and γ = 1. Each of the four solitons is an N=8 soliton in the second fiber. We let the four soliton set propagate for 0.1261 $z_0^{(2)}$, which is identical to 0.03290 $z_0^{(1)}$. The scaling factor η is 0.01285. We repeat this procedure with the third fiber, and let the four sets of four solitons propagate for 0.1261 $z_0^{(3)}$, so that there are three stages total. The output consists of four sets of four sets of four solitons.

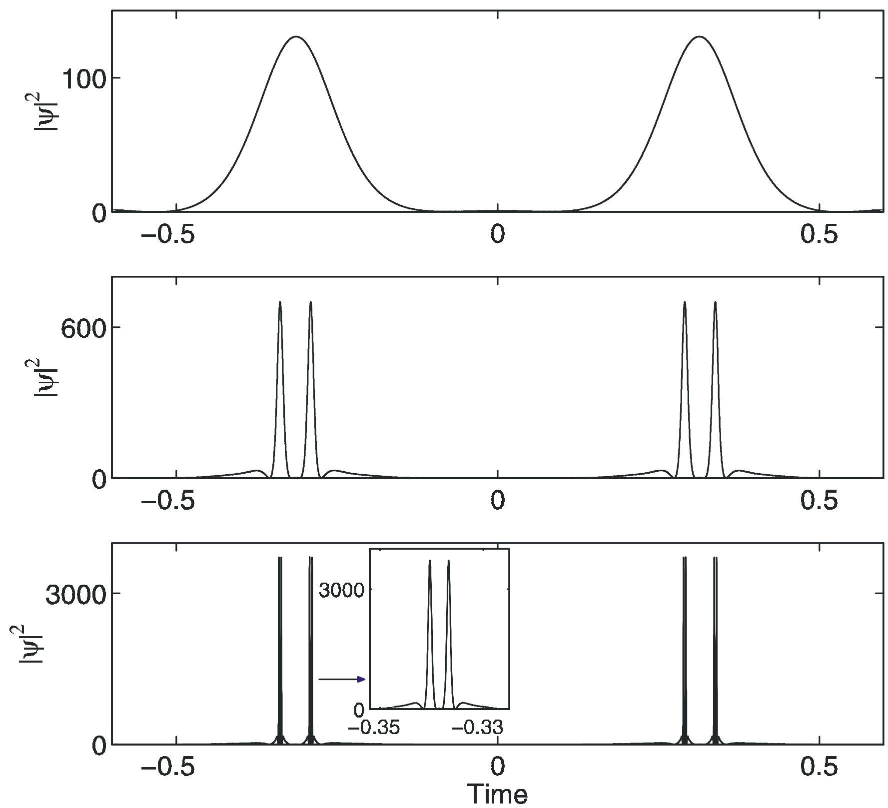

Figure 4.5-3: Temporal pulse envelope after each of the three stages for Doublet Cantor Set. The bottom figure shows two sets of two sets of two. The inset in the bottom panel shows a magnification of one of the four sets of two. Units are normalized so that T_0 =1, peak power = 1, and 1 unit of distance = $T_0^2/|\beta^{(i)}|$.

The same method is used to generate the Doublet Cantor Set fractals in Fig. 4.5-3, where an N =5 soliton is propagated for 0.1623 $z_0^{(i)}$ in each fiber segment. Figure 4.5-3a shows the two output pulses emerging from the first segment. The two pulses are then fed into the rescaled environment, where they mimic the original N=5 soliton, each breaking up into two more pulses (Fig. 4.5-3b). Figure 4.5-3c shows the output after the third segment. At this stage we have two sets of two sets of two pulses, which is a Cantor Set pre-fractal. If one could construct an infinite number of fiber segments, then it would be an exact regular Cantor Set fractal in the mathematical sense. In physical systems, however, limitations such as high order dispersion, dissipation, and Raman scattering place a bound on the number of stages. As with any physical fractal, the breakups are pre-fractals rather than fractals; yet, we expect at least three stages in a real physical fiber sequence. To prove the generation of an exact Cantor Set fractal, we choose random selections from each of the three panels of Fig. 4.5-3 and plot them on the same scale as displayed in Fig. 4.5-4: they fully coincide with one another. The exactness of the overlap in Fig. 4.5-4 indicates that this indeed is an exact Cantor Set fractal. Similarly, we verify that the Quadruplet fractals from Fig. 4.5-2 are exact. We have also generated a Triplet Cantor Set fractal from an N=6 soliton, propagated for 0.1649 $z_0^{(i)}$.

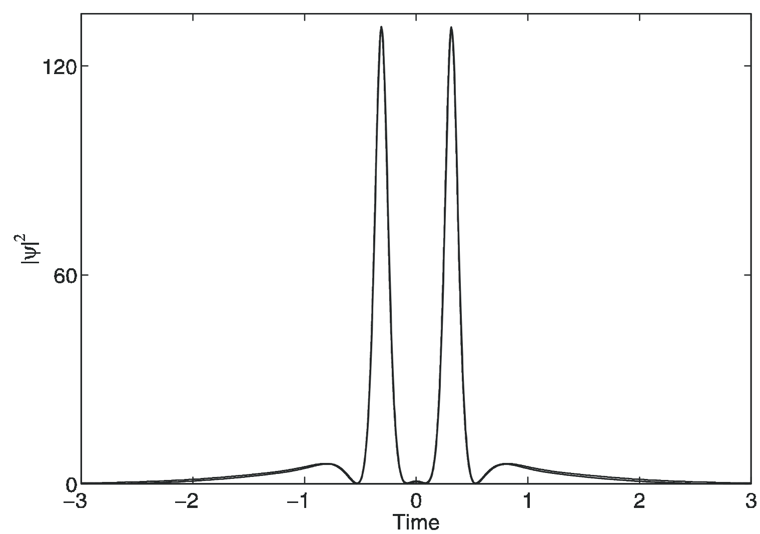

Figure 4.5-4: Illustration of exact self-similarity of pulse envelopes after each of the stages of the Doublet Cantor Set. The three panels shown in Figure 4.5-3 have been appropriately rescaled, shifted, and overlapped. Units are T_0 =1, peak power = 1, and 1 unit of distance = $T_0^2/|\beta^{(i)}|$.

4.5.4. Experimental proposal for observing exact fractals

One can design a simple experimental implementation of Cantor Set fractals in a fiber optic propagation system. For example, a Doublet Cantor Set can be generated from the breakup of an N=3 soliton. In the first stage a 50 ps FWHM pulse of 0.88 Watt peak power is launched into a 6 km long fiber with $\beta^{(1)}=-127.6$ ps^2/km (assuming a nonlinear factor, $\gamma = 1.62$ Watt^{-1} km^{-1} for all fibers.) At the end of this fiber, which corresponds to the midpoint of the soliton period, the input pulse has broken into two pulses of peak power 1.2 Watts and width 13.2 ps spaced 42 ps apart.. These two pulses are then coupled into a second, 4.1 km long fiber characterized by a dispersion parameter of $\beta^{(2)}=-12.2$ ps^2/km. The pulses exiting this second stage are each 3.3 ps in duration and peak power 1.9 Watts. They are grouped in pairs separated by 9.9 ps. Finally, the pulses are propagated in a third 2.7 km long stage with $\beta^{(3)}=-1.2$ ps^2/km. This results in 2 sets of 2 sets of 2 pulses, each of width 816 fs and peak power 3 Watts, grouped in pairs separated by 2.4 ps. These results have been confirmed through numerical simulations including third order dispersion, fiber loss, and Raman scattering. The inclusion of these additional terms in Eq. (4.5-1) limits the number of stages which may be realistically obtained experimentally. The example system given above is consistent with readily available fibers. One may use specialty fibers (e.g., dispersion flattened fibers or fibers with exponentially decreasing dispersion) to further combat effects of third order dispersion and loss and to expand the number of experimentally realizable stages.

The Cantor Set fractals generated in the fiber optic system are robust to a variety of perturbations in the fiber parameters and variations in the initial pulse conditions. We simulated the evolution of the Cantor Set fractals under 5% deviations in the pulse peak power, pulse width, fiber length and dispersion. In addition we added 2% (of the power) of excess gaussian white noise and launched a gaussian initial pulse shape. Under all these variations in the physical parameters, the resulting Cantor Set fractals exhibit excellent similarity to the ideal case.

4.5.5. Fractal dimensions

Although we only generate pre-fractals, we can calculate the fractal dimension for an equivalent infinite number of stages. There are various definitions of fractal dimensions; here we calculate the **similarity dimension**, D_S. In the construction of a fractal structure an original object is replicated into many rescaled copies. If the length of the original object is defined as unity, the parameter ε is defined as the length of each new copy, and N is the number of copies. The similarity dimension is then [58]: $D_S = \log(N)/\log(1/\varepsilon)$. For the Doublet Cantor Set fractal from Fig. 4.5-3, D_S = 0.2702, and for the Quadruplet Cantor Set fractal from Fig. 4.5-2, D_S = 0.4318.

4.5.6. Conclusion of section 4.5

We have shown how a nonlinear soliton-supporting system can be driven to generate Exact (regular) Cantor Set fractals, and demonstrated theoretically optical temporal Cantor Set fractals in a sequence of nonlinear optical fibers. The next challenge is to observe these Cantor Set fractals experimentally.

4.6. EXPERIMENTS IN PHOTOREFRACTIVE MATERIALS

Most experiments in our laboratory are done in photorefractive materials. Consequently, I tried to do statistical fractal experiments with photorefractive materials in (2+1)D. The extra dimensionality was supposed to give additional richness to the system. The purpose of the experiment was also to provide additional insight and intuition about the process of fractal generation. The beam we typically started with was a circular beam of radius approximately 160μm. I was hoping that in the first stage, the beam would split into smaller circular beams of approximately 40μm radia. Then, in the second stage, I was hoping to induce a breakup of each of these beams into even smaller circular beams of radia approximately 10μm. Unfortunately, the non-linearity in the photorefractive materials we use (SBN60, and SBN75) is highly anisotropic. Consequently, during the first stage, the beam broke up in one of the transverse directions, creating "rolls", as seen in Figures 4.6-1a, and 4.6-1b. In the second stage however, instead of each roll breaking up further into more narrow features, the rolls broke up in the other transverse direction, thereby creating 2D filaments, as seen in Figure 4.6-1c. Therefore, the final result was not really a fractal (although the breakup process does have many features of statistical fractals). We conclude that fractals of our kind should be much easier to observe in isotropic non-linear materials, or else in (1+1)D.

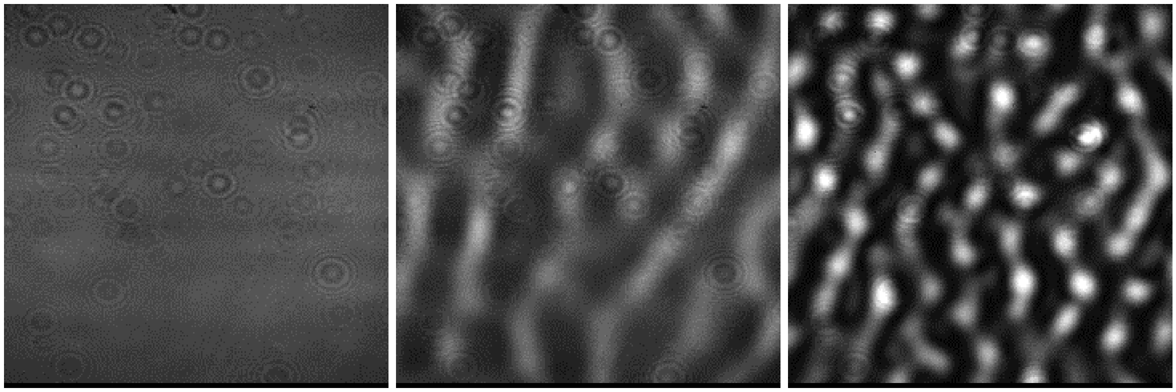

(a) (b) (c)

Figure 4.6-1: Experiments demonstrating that anisotropy significantly hinders observing statistical fractals in photorefractive materials. The material used was SBN60. At the input of the first stage, the beam is very broad (app. 160μm), as seen in (a). By the output of the first stage, because of high anisotropy of the non-linearity in SBN60, the beam breaks up in the x-direction first, as seen in (b). This is used as the input to the second stage. By the output of the second stage, the beam breaks up in the y-direction, as seen in (c).

4.7. CONCLUSION OF CHAPTER 4

In conclusion, we have proposed a general scheme of generating fractals by the dynamics of solitons that undergo abrupt changes along their propagation paths. This method of fractal generation is universal and should exist in many nonlinear system that can support solitons. Interestingly, this is one of the very few cases in which one can generate fractals experimentally and investigate them theoretically knowing all the physics involved. Furthermore, this is one of very rare physical systems that can support exact fractals as well.

Nevertheless, there is one more issue that needs to be addressed; one might argue that the process we describe is a "prepared process" and unlikely to occur naturally in soliton-supporting systems in nature. This is because one always needs to have an abrupt change in at least one parameter of the system. Clearly, it would be very nice to have a cascaded breakup process that occurs naturally. As an avenue of further research, we propose studying a system that exhibits a first order phase transition, which is driven by light. In such a system, the nonlinear evolution process can trigger the next stage of breakup. We have been thinking about several examples of such processes. One example has to do actually with spatial (not temporal) solitons that follow the same equations and can give rise to fractals as well. A nonlinear system in which the EM field, through the nonlinearity, induces a first order (paraelectric to ferroelectric) phase transition has recently been found [67]. We are thinking about a homogeneous crystal like that, in which the optically-driven photorefractive diffusion fields induce the phase transition and cause crystallization. This process starts at the input and progresses (in time) from the input forward, and each narrow beam forms a soliton through the interaction at the phase transition. Now those diffusion fields are always proportional to the gradient of the optical intensity. Thus, narrower solitons will generate larger fields that will overcome the diffusion fields that survived from the previous layer and take over. This is the general idea. In Ref. [67], one can find a list of similar effects in numerous other material systems, so one might be able to find an even more suitable system.

CHAPTER 5: MODULATION INSTABILITY OF INCOHERENT WAVES

5.1. INTRODUCTION

Modulation instability (MI) is a non-linear process closely related to soliton formation. During MI, small amplitude and phase perturbations tend to grow exponentially as a result of the combined effects of nonlinearity and diffraction/dispersion. Because of this, a broad optical beam or a quasi-CW pulse tends to disintegrate during propagation [68,69]. Since MI typically occurs in the same parameter region where bright solitons are observed, it can be loosely considered as a precursor to soliton formation. Until recently, optical spatial solitons were solely coherent entities. However, a recent series of experimental [27,28] and theoretical [70-74] works has demonstrated solitons made of partially-incoherent light: Incoherent Solitons. They exist in non-instantaneous nonlinear media, when the average phase fluctuation time across the beam (or between modal constituents) is much shorter than the response time of the medium. In this case, the nonlinear change in the refractive index depends only on the time average of the light intensity [27,28,71]. The existence of incoherent solitons proves that self-focusing is possible not only for coherent wave-packets but also for partially-spatially/temporally-incoherent light [27,28]. In other words, incoherent solitons are self-trapped envelope wave-particles of weakly-correlated many-particle systems. Now, since MI appears in all systems that support bright solitons, it is natural to wander whether it also exists for incoherent light beams.

In this chapter, we demonstrate, analytically and numerically, the existence of incoherent MI, that is, modulation instability of incoherent wave-packets. Incoherent MI occurs when the value of the nonlinearity exceeds a threshold imposed by the degree of spatial coherence. We use analytical and numerical methods to study the properties of incoherent MI in a general self-focusing non-instantaneous medium. We solve for incoherent MI in closed form for input beams with Lorentzian angular power spectra, and illustrate it with Kerr and saturable nonlinearities; this is presented in section 5.2. In section 5.3, we confirm our results with numerical simulations, and further study general cases of input beams along with propagation-evolution effects. In section 5.4, we put our results in perspective with other work in related areas of physics. Finally, in section 5.5, we present preliminary experimental results on incoherent MI. We conclude this chapter in section 5.6. Most material presented in this chapter appeared in [33], except for section 5.5, which is yet to be submitted [76].

5.2. THEORETICAL ANALYSIS

The incoherent light we analyze propagates in the z-direction, with its spatial coherence length being much smaller than its temporal coherence length; i.e., the beam is a partially-spatially-incoherent and quasi-monochromatic (the wavelength of light λ is much smaller than each of these coherence lengths). The nonlinear material is non-instantaneous, that is, the nonlinear index change is a function of the optical intensity, time-averaged over the response time of the medium, τ, which is much longer than the coherence time of the light, t_c. Assuming the light is linearly polarized and $E(r,z,t)$ is its slowly varying amplitude, we define $B(r_1,r_2,z) = \langle E^*(r_2,z,t)E(r_1,z,t)\rangle$ where the brackets denote the time average (taken over τ). The equation for B, as derived from paraxial wave equation, is [73]:

$$\frac{\partial B}{\partial z} - \frac{i}{k}\frac{\partial^2 B}{\partial r \partial \rho} = \frac{in_0}{k}\left(\frac{\omega}{c}\right)^2 \{\delta n(r_1,z) - \delta n(r_2,z)\}B, \qquad (5.2\text{-}1)$$

where ω is the carrier frequency, k is the carrier wave-vector, n_0 is the index of refraction without light present, δn is the tiny nonlinear modification to the refractive index, $r=(r_1+r_2)/2$ is the middle point coordinate, and $\rho=r_1-r_2$ is the difference coordinate. $B(r,\rho,z)$ is the spatial correlation function, and $I(r,z)=B(r,\rho=0,z)$ is the time-averaged light intensity. The definition of B yields $B(r,\rho,z)=B^*(r,-\rho,z)$.

To study MI, we assume the incident light to have a uniform intensity, except for small intensity perturbations that depend on r and z. Thus, B can be written as $B(r,\rho,z)=B_0(\rho)+B_1(r,\rho,z)$, where $B_1 \ll B_0$, $B_0(\rho)$ representing the background of a uniform intensity $I_0=B_0(\rho=0)$. The dependence of δn on r comes from B_1, so to the lowest order in B_1, $\{\delta n(r_1,z)-\delta n(r_2,z)\}=\kappa\{B_1(r_1,\rho=0,z)-B_1(r_2,\rho=0,z)\}$, where $\kappa=d[\delta n(I)]/dI$ evaluated at I_0 is the marginal nonlinear index. In the Kerr case ($\delta n=\gamma I$), so $\kappa=\gamma$. Because of the time-averaging properties of the material, any random time-dependent perturbation, no matter how large, if it occurs on a time scale shorter than τ, averages to zero; only time-independent perturbations lead to MI in our system. Therefore, linearizing Eq.(5.2-1) in B_1 produces:

$$\frac{\partial B_1}{\partial z}-\frac{i}{k}\frac{\partial^2 B_1}{\partial r\partial \rho}=\frac{in_0}{k}\left(\frac{\omega}{c}\right)^2\kappa\left\{B_1(r+\frac{\rho}{2},\rho=0,z)-B_1(r-\frac{\rho}{2},\rho=0,z)\right\}B_0(\rho). \qquad (5.2\text{-}2)$$

Up to this point, the discussion applies for any correlation function $B_0(\rho)$. In what follows, we assume that $B_0(\rho)$ has a Lorentzian-shaped k-spectrum and obtain closed-form results. Thus, $\hat{B}_0(k_x)=A/[k_x^{\,2}+k_{x0}^2]$, where $\hat{F}(k_x)=\frac{1}{2\pi}\int_{-\infty}^{\infty}d\rho F(\rho)e^{ik_x\rho}$ is the Fourier transform of $F(\rho)$ for any $F(\rho)$. In this case the normalized angular power spectrum [70] is also Lorentzian $(G_N(\theta)=(\theta_0/\pi)(\theta^2+\theta_0^2)^{-1}$ where the angle $\theta=k_x/k$ is in radians. The background intensity is then $I_0=\pi A/k_{x0}$. The physically acceptable eigenmodes of the Eq.(5.2-2) can be written as $B_1(r,\rho,z)=\exp(gz)\exp[i(\alpha r+\phi)]L(\rho) +\exp(g^*z)\exp[-i(\alpha r+\phi)]L^*(-\rho)$, where ϕ is an arbitrary real phase that carries no physical significance, α is real and g is associated with the MI gain. These modes automatically satisfy $B_1(r,\rho,z)=B_1^*(r,-\rho,z)$. For each α one can obtain a set of modes $L(\rho)$ needed to describe any perturbation B_1. Defining $M(\rho)=L(\rho)/L(\rho=0)$, with the boundary condition $M(\rho=0)=1$, we get:

$$gM(\rho)+\frac{\alpha}{k}\frac{dM(\rho)}{d\rho}+\frac{2\omega\kappa}{c}\sin\left(\frac{\rho\alpha}{2}\right)B_0(\rho)=0 \quad . \tag{5.2-3}$$

We are interested in the modes that grow: those with g that is not pure imaginary. We look for the particular and for the homogeneous solutions to Eq.(5.2-3). Since we have a physical constraint that $M(\rho)$ has to be bounded for large $|\rho|$, the homogenous solution has to be zero for the modes that have a real part in g. Therefore, by seeking a particular solution of Eq.(5.2-3), we find

$$\hat{M}(k_x)\left(g-i\frac{\alpha}{k}k_x\right)=\frac{i\omega\kappa}{c}\left[\hat{B}_0\left(k_x+\frac{\alpha}{2}\right)-\hat{B}_0\left(k_x-\frac{\alpha}{2}\right)\right]. \tag{5.2-4}$$

$M(\rho)$ obtained from Eq.(5.2-4) is clearly bounded for large $|\rho|$. Impose $M(\rho=0)=1$, or $\int_{-\infty}^{\infty}\hat{M}(k_x)dk_x=1$:

$$1=-\frac{\omega\kappa}{c}\int_{-\infty}^{\infty}dk_x\left[\hat{B}_0\left(k_x+\frac{\alpha}{2}\right)-\hat{B}_0\left(k_x-\frac{\alpha}{2}\right)\right]\left[\frac{1}{ig+\alpha k_x/k}\right], \tag{5.2-5}$$

which gives us a constraint that determines the dispersion relation $g(\alpha)$ for the modes whose g has a real part, for arbitrary $B_0(\rho)$. Note that $\hat{B}_0(k_x)$ is purely real since $B_0(\rho)=B_0^*(-\rho)$.

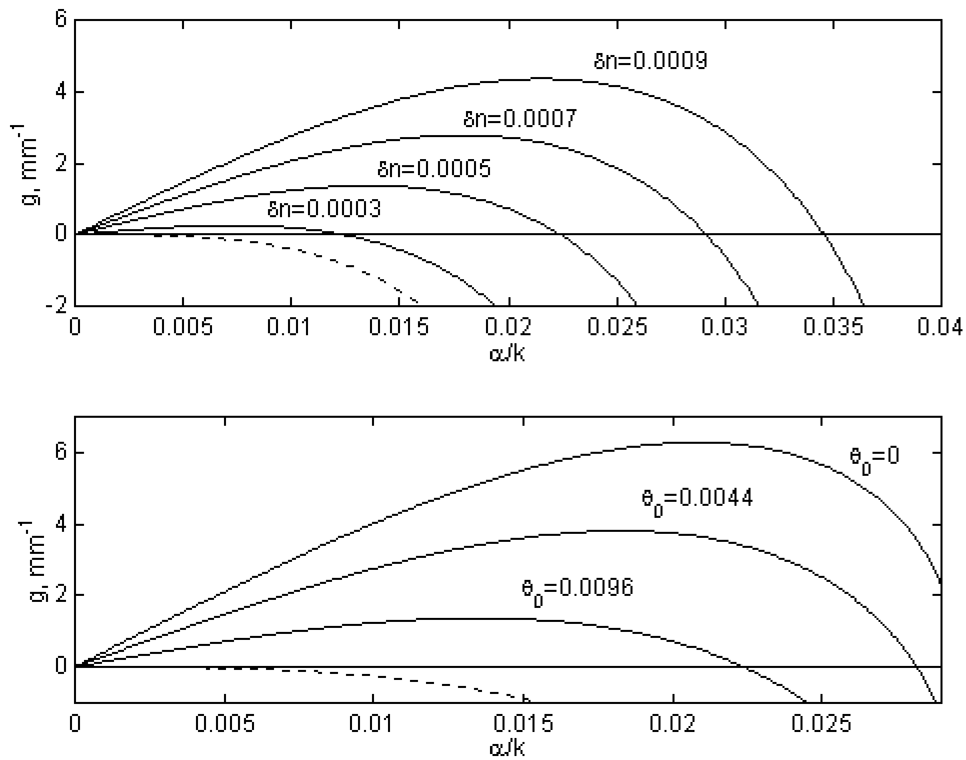

Figure 5.2-1: Incoherent MI for Kerr nonlinearity: growth rate of perturbations vs the perturbation wavelengths. The light wavelength in vacuum is 500nm, and the refractive index n_0=2.3. The background uniform intensity has a Lorentzian shaped angular power spectrum of width θ_0. The nonlinear index change due to the background is given by δn. In the upper plot, we show gain curves for a few δn's, with a fixed θ_0=0.0096 rads; the dashed line in the plot has δn marginally small enough so that MI just disappears. In the lower plot, we show gain curves for a few θ_0's, with a fixed δn=0.0005; the dashed line in the plot has θ_0 marginally large enough so that MI just disappears.

By assuming a Lorentzian k-spectrum $\hat{B}_0(k_x) = A/[k_x^{\ 2} + k_{x0}^2]$ in Eq.(5.2-5), a contour integration yields the following result for the mode that grows, if g is bigger than zero:

$$\frac{g}{k} = -(k_{x0}/k)(|\alpha|/k) + (|\alpha|/k)\sqrt{\frac{\kappa I_0}{n_0} - \left(\frac{\alpha}{2k}\right)^2}\ . \qquad (5.2\text{-}6)$$

where κ represents the marginal nonlinear index change because of the constant background intensity, and $k_{x0}/k = \theta_0$. The result of Eq.(5.2-6) clearly demonstrates that the MI growth rate is substantially affected by the coherence of the source. Moreover, in the limit $k_{x0} \to 0$, it correctly reduces to the well known result of coherent MI [68,69]. Even more importantly, Eq.(5.2-6) indicates that for a given degree of coherence, MI occurs only when the quantity κI_0 exceeds a specific threshold; incoherent MI exists **only if** $\kappa I_0/n_0 > \theta_0^2$, whereas when $\kappa I_0/n_0 < \theta_0^2$, MI is ***entirely eliminated***. Thus, the more incoherent a source is, the larger κI_0 (marginal index change) required to induce MI. Computer simulations suggest that this trend is *universal* and is independent of the angular power. Having found $g(\alpha)$, one can then easily determine the intensity of the perturbation $I_1(r,z) = B_1(r, \rho = 0, z)$.

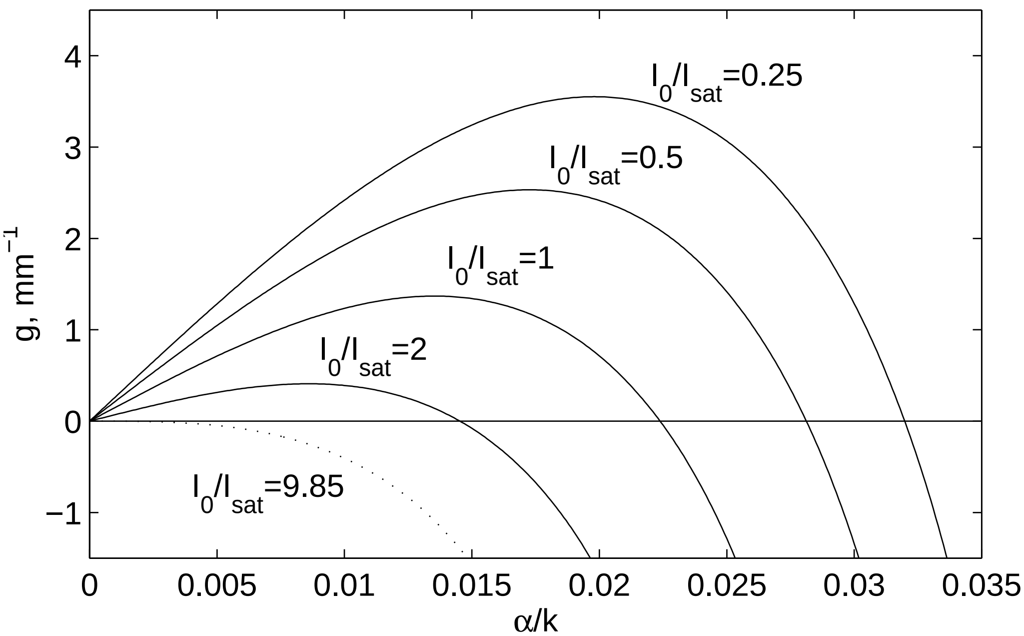

Figure 5.2-2: Incoherent MI for a saturable nonlinearity: growth rate of perturbations vs the perturbation wavelengths. λ in vacuum is 500nm, and the refractive index n_0=2.3. The background uniform intensity has a Lorentzian shaped angular power spectrum of width θ_0=0.0096 rads. The nonlinear index change due to the background is δn=0.001. In the saturable case, there is additional suppression due to the saturation. The gain curves are plotted for various degrees of saturation; the dashed curve presents the case when the saturation is marginally large enough so that MI just disappears.

To apply the result of Eq.(5.2-6) for Kerr nonlinearity $\delta n(r)=\gamma I$, we set $\kappa=\gamma$ and present it graphically in Fig.5.2-1. In this case, $\kappa I_0=\delta n$, so the larger the non-linear index change, the stronger MI. However, the MI growth rate can be analytically determined for any type of nonlinearity. Of particular significance is the saturable nonlinearity which occurs for example in photorefractives [19], and in homogeneously-broadened 2-level systems (atomic rubidium vapor) [66], in which the nonlinear index change is of the form $\delta n(r)=\gamma I(r)/[1+I(r)/I_{sat}]$. For the saturable case, we find that the growth rate is given by Eq.(5.2-6) with $\kappa=\gamma/[1+I_0/I_{sat}]^2$. As with the Kerr nonlinearity, incoherent MI exists, once again, only above a specific threshold for κI_0. From the result, it is apparent that saturation suppresses MI by a factor of $1/[1+I_0/I_{sat}]$. Figure 5.2-2 displays graphically typical results with the saturable nonlinearity.

5.3. NUMERICAL SIMULATIONS

To verify our analytical findings and to further explore incoherent MI, we use computer simulations. In particular, the intensity/correlation MI dynamics of Eq.(5.2-1) are investigated by means of the coherent density approach [70]. The power Fourier spectrum of the intensity fluctuations growing on top of the constant incoherent background is used to identify the spatial frequencies that exhibit maximum gain. Figure 5.2-3(a) shows the evolution of the power spectra of the intensity fluctuation when the angular power spectrum of the source is Lorentzian, and the nonlinearity is Kerr type. In this example, θ_0=9.6 mrads, $\gamma I_0=5*10^{-4}$, $n_0 = 2.3$, λ=0.5 μm in vacuum. These results indicate that maximum MI gain is attained at a spatial frequency $\alpha/k \approx 0.0135$, with a peak value of $g=1.37mm^{-1}$, both in an excellent agreement with that predicted from Eq.(5.2-6) as also depicted in Fig.5.2-1 for the same set of parameters. Note that in this case the spatial frequency where maximum MI gain occurs remains invariant during propagation. After a certain distance (in this example after 9 mm) additional sub-bands emerge as in the case of coherent MI [75]. This is "secondary" MI: modulation instability for which the first amplified instability peak acts as a "pump" and plays the role of B_0. Numerical simulations confirm another prediction of the analytic result: **the existence of a threshold for incoherent MI**. The numerical study also provide information about the evolution of incoherent MI from input beam of angular power spectra different than the Lorentzian shape. For example, Fig. 5.2-3(b) depicts information similar to Fig. 5.2-3(a) when the source angular power spectrum is

Gaussian ($G_N(\theta) = (1/\pi^{1/2}\theta_0)\exp(-\theta^2/\theta_0^2)$). In this case θ_0=9.6 mrads, γI_0=2.5x10^{-4}, $n_0 = 2.3$, and λ=0.5 μm. The MI spectra initially evolve in a fashion similar to the Lorentzian case, but, after some propagation distance the perturbation grew substantially, (and our analytic approximation $B_1 \ll B_0$ no longer holds), and the MI spectrum does not exhibit a clear peak but broadens with propagation. As observed from Eq.(5.2-5), the MI growth highly depends on the shape of the angular power spectrum of the source.

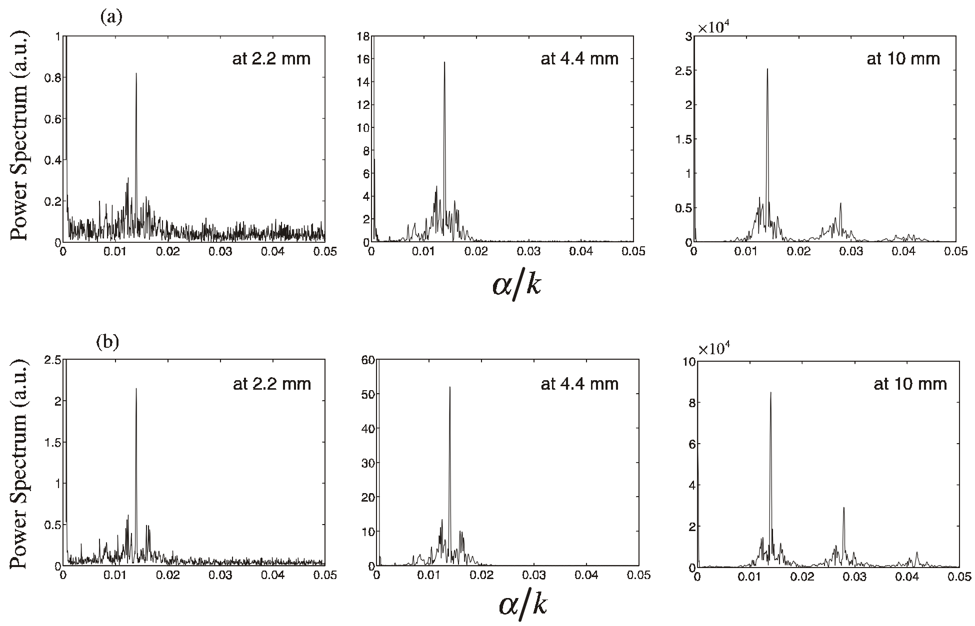

Figure 5.2-3: Power spectrum of an incoherent beam during propagation in Kerr nonlinearity when (a) the source power spectrum is Lorentzian with θ_0=0.0096rads and δn=0.0005; (b) the source power spectrum is Gaussian with θ_0=0.0096rads and δn=0.00025.

5.4. PERSPECTIVE

We emphasize that one can use our logic up to Eq.(5.2-6) in order to obtain analytical understanding of MI with an arbitrarily shaped angular power spectrum, where one needs to solve the integral in Eq.(5.2-5) numerically (except for the Lorentzian case, where one can obtain closed-form solutions as we did). When we apply this idea for an input beam of a Gaussian power spectrum [Fig. 5.2-3(b)], we obtain an excellent agreement between our analytic and numeric results. The analytic expansion also captures the fact that there always exists a threshold κI_0 for incoherent MI to occur.

We also wish to emphasize that our MI results cannot be obtained using a ray optics (transport) approach [72], which assumes that the source is fully incoherent (or the period of the perturbation is much larger than the transverse coherence length). In this picture, each ray behaves like a particle that follows a trajectory determined by the local index of refraction, which has a role of potential. The local index of refraction is in turn determined by the local density of the rays. Therefore, this picture is very similar to a gravitational system of many particles. Unfortunately, for partially spatially-incoherent optical beams, the spatial frequency that grows fastest is beyond this regime. Nevertheless, studying this approach is instructive because it connects the incoherent MI system with systems as different as galaxy formation, and one can use it to predict driven MI (induced-MI).

5.5 EXPERIMENTS ON INCOHERENT MI

At the moment of writing this thesis, the experiments are being performed in our laboratory, trying to confirm the predictions of the theory of incoherent MI presented in this chapter. These experiments are done in collaboration with Dr. Detlef Kip [76], who is currently a research fellow in our group. In this section, we present preliminary results of incoherent MI experiments that already confirm some of the predictions of the theory.

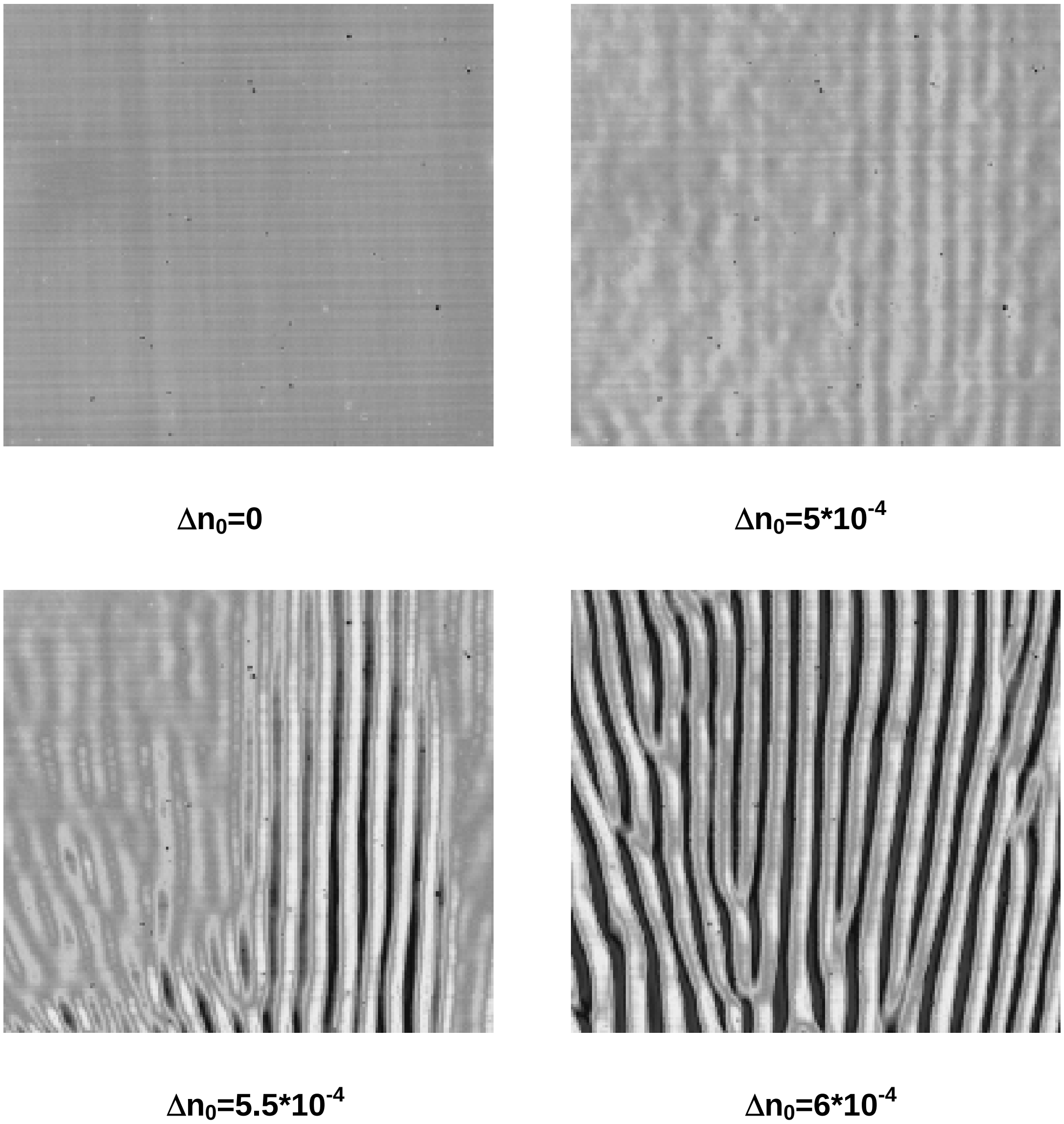

Figure 5.5-1: Experiments with incoherent MI in photorefractive materials. For a fixed coherence length, $l_C=8\mu m$, we varied the light intensity induced change in the index of refraction, Δn_0. As we can see, there is no MI just below $\Delta n_0=5.5*10^{-4}$, and it clearly appears just above this Δn_0; this clearly demonstrates existence of a threshold in incoherent MI. Existence of such a threshold was predicted by the theory presented in this chapter.

The experiments we perform are in (2+1)D, since they are done in photorefractive materials, while our current theory is for (1+1)D. Furthermore, the exact shape of the correlation function is very difficult to measure; the only quantity experimentally accessible to us at this point is the correlation length, l_C (up to a constant factor, this is an inverse of the parameter θ_0, used above). Consequently, at this point, we are able to do only qualitative comparison with the theory. Nevertheless, the qualitative predictions of the theory are very nicely confirmed by the experiment. In Figures 5.5-1, and 5.5-2, we present some representative examples that demonstrate the agreement of the theory with the experiment.

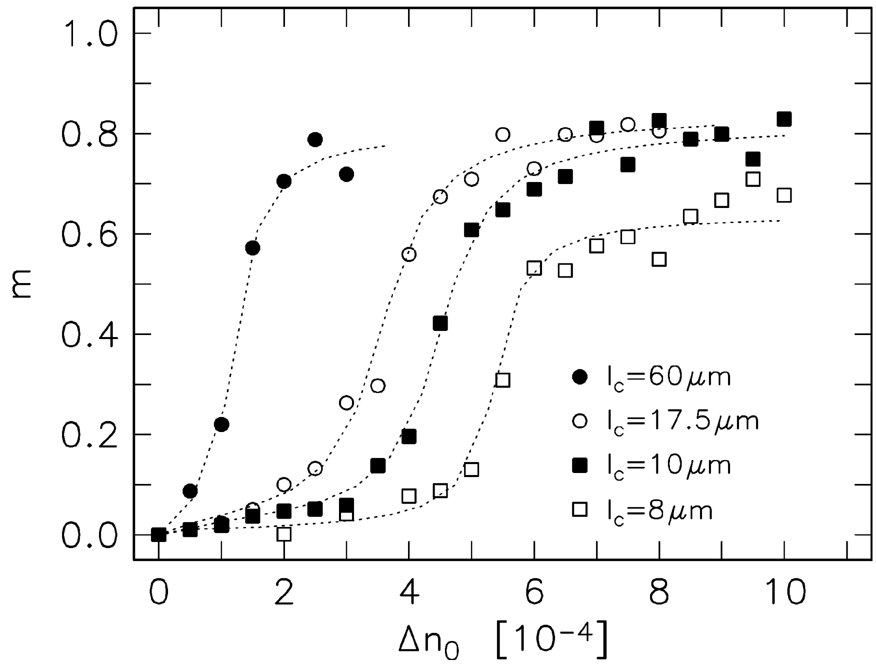

Figure 5.5-2: Relative modulation depth vs. the non-linear change in the index of refraction, for a few different coherence lengths. Modulation depth m=0 denotes uniform intensity, while m=1 denotes non-uniform intensity which oscillates between zero and maximum intensity. This figure clearly demonstrates existence of a rather sharp threshold for every fixed coherence length. Furthermore, it also demonstrates that for smaller coherence lengths (larger incoherence), larger non-linear changes to the index of refraction are needed to overcome the threshold. This feature is also predicted by our theory when applied for the particular non-linearity used in this experiment.

5.6. CONCLUSION OF CHAPTER 5

To conclude, we have shown that modulation instability exists in partially incoherent systems, and that its existence requires the marginal nonlinear index change times the background intensity, κI_0 to be above a well-defined threshold. This is in a marked difference with coherent MI, since there does not exist a similar threshold for coherent MI. The κI_0 is determined by the spatial degree of coherence (angular power spectrum). To emphasize the fundamental importance of this result, recall that partially incoherent light is a system in which the "quasi-particles" are only weakly phase-correlated (with the extreme case being a fully incoherent system in which the "quasi-particles" are fully non-correlated). Yet this weakly-correlated system exhibits features characteristic of a phase-transition: above a well-defined threshold, it collapses and forms "clusters" (filaments). We also emphasize that, since modulation instability is a precursor of solitons, it is to some extent an even more universal phenomenon than solitons. In fact, MI appears in all systems supporting solitons [77] and also in systems in which solitons have not been identified as of yet. We have identified here MI in an incoherent system, which is fundamentally a system in which repulsion forces are much weaker than the attraction forces [1,5]. Since nature is full of nonlinear systems in which incoherent wave-packets exist (e.g., optics [78], plasma physics [79]), we expect that these systems will exhibit MI as well. We believe that this work lays the foundations for instabilities and pattern formation in any nonlinear incoherent system in nature. Furthermore, incoherent MI links to other related but qualitatively different phenomena, such as galaxy formation. From all of these arguments, one thing is obvious: there are many more new exciting features that are intimately related to incoherent modulation instability, and are yet unraveled calling for future research.

6. CONCLUSION AND FUTURE WORK

In this dissertation, we studied various aspects of instabilities associated with non-linear wave propagation. The systems we were interested in display a great richness of very diverse physical phenomena. During the research we came upon quite a few very interesting new physical systems. Still, the possibilities of exciting new research opened by the results presented in this dissertation are even much more plentiful.

We constructed and studied necklace beams, which are the first stable self-trapped shapes in Kerr media. As an avenue of further research, it would be interesting to study necklace beams in other non-linear media: their interactions, collisions, conserved quantities in the collision processes, transfer of information (via transfer of conserved quantities) through collisions, etc.

Further, we presented necklace beams carrying angular momentum, and also for the first time non-integer per-photon angular momentum. It would be very interesting to study these necklaces in other non-linear media. Furthermore, if a necklace is composed of circularly polarized light, each photon carries spin in addition to angular momentum. In this case, there should be non-linear materials where the transfer of polarization to angular momentum (and vice-versa), is possible. Moreover, studying interactions of such necklaces, and perhaps transfer of angular momentum and spin during such interactions should be very interesting; this would be particularly interesting if the necklaces in question are composed of a only a few (instead of a macroscopic number of), photons. The very high non-linear coefficients which are necessary to achieve something like this are available today in electromagnetically induced transparency materials [80].

We also presented a principle that allows one to generate fractals (and also exact fractals), in almost any soliton-supporting system in nature. However, at the point of writing this thesis, a necessary prerequisite for such fractal generation is an abrupt change in one of the physical parameters describing the system. In future, we plan to study physical systems where a smooth change in one of the physical parameters (for example light intensity due to absorption), leads to an abrupt change in the physical parameter that causes the required breakup. Of course, we are talking here about optically induced phase transitions.

The non-linear systems we study demonstrate a great richness of non-linear phenomena: modulation instability, solitons, chaos, and now, as have seen also fractals. All these phenomena appear in the same materials, but in different parameter regimes. Consequently, it should be educational to study what parameter phase spaces imply which non-linear phenomena, and how do these different regimes relate to each other.

Finally, we predicted the existence, and studied the properties of modulation instability in incoherent wave systems. This turns out to be a very rich physical system that opens many new avenues of research. One of the avenues is certainly extending our theory from (1+1)D to (2+1)D; the extra dimensionality should add even more richness to the system. Developing a statistical mechanics description of the system should also be very interesting. In addition, one might also want to enclose an incoherent MI system in a cavity, and study for the first time incoherent pattern formation.

REFERENCES

(1) M. Segev and G. I. Stegeman, Physics Today 51(8), 42 (1998).

(2) J. S. Russell, in "14th meeting of the British Association Reports", York, 1844.

(3) Callan, Harvey, and Strominger; *Supersymmetric String Solitons*, "Proceedings of the 1991 Trieste spring school on Quantum Field Theory", (World Scientific)

(4) E. Infeld and G. Rowlands, *Nonlinear Waves, Solitons and Chaos*, Chap. 5, Cambridge University Press, 1990.

(5) For detailed "semi-popular" review on the various kinds of optical spatial solitons, see M. Segev, Opt. and Quant. Elect. **30**, 503 (1998). For a detailed review on dark spatial solitons, which are not covered here, see Y. S. Kivshar and B. Luther-Davies, Phys. Rep. **298**, 81 (1998).

(6) G. A. Askar'yan, Sov. Phys. JETP **15**, 1088 (1962); R. Y. Chiao, E. Garmire and C. H. Townes, Phys. Rev. Lett. **13**, 479 (1964).

(7) P. L. Kelley, Phys. Rev. Lett. **15,** 1005 (1965).

(8) A new type of stable (2+1)D solitons in Kerr media was recently found in the form of Necklace-ring beams: see M. Soljačić, S. Sears and M. Segev, Phys. Rev. Lett. **81**, 4851 (1998).

(9) A. Barthelemy, S. Maneuf and C. Froehly, Opt. Comm. **55**, 201 (1985).

(10) J. S. Aitchison, A.M. Weiner, Y. Silberberg, M. K. Oliver, J. L. Jackel, D. E. Leaird, E. M. Vogel and P. W. Smith, Opt. Lett. **15**, 471 (1990).

(11) J. S. Aitchison, K. Al-Hemyari, C. N. Ironside, R. S. Grant and W. Sibbett, Electron. Lett., **28**, 1879 (1992); J. U. Kang, G. I. Stegeman, J. S. Aitchison and N. Akhmediev, Phys. Rev. Lett., **76**, 3699 (1996)

(12) U. Bartuch, U. Peschel, Th. Gabler, R. Waldhaus and H.-H. Horhold, Optics. Comm., **134**, 49 (1997)

(13) J. E. Bjorkholm and A. Ashkin, Phys. Rev. Lett. **32**, 129 (1974)

(14) G. Khitrova, H. M. Gibbs, Y. Kawamura, H. Iwamura, T. Ikegami, J. E. Sipe amd L. Ming, Phys. Rev. Let., **70**, 920 (1993)

(15) W. Torruellas, B. Lawrence and G.I. Stegeman, Elect. Lett., 32:2092-4 (1996)

(16) M. Segev, B. Crosignani, A. Yariv and B. Fischer, Phys. Rev. Lett. **68**, 923 (1992).

(17) G. Duree, J. L. Shultz, G. Salamo, M. Segev, A. Yariv, B. Crosignani, P. DiPorto, E. Sharp and R.R. Neurgaonkar, Phys. Rev. Lett. **71**, 533 (1993)

(18) For a review on photorefractive solitons, see M. Segev, B. Crosignani, P. DiPorto, M. Shih, Z. Chen, M. Mitchell, and G. Salamo, *Photorefractive spatial solitons*, Chapter 9 in the book *Beam Shaping and Control with Nonlinear Optics*, Editors: F. Kajzar and R. Reinisch, Publisher: Plenum Press, New York, 1998.

(19) M. Segev, G. C. Valley, B. Crosignani, P. DiPorto and A. Yariv, Phys. Rev. Lett. **73**, 3211 (1994); D. N. Christodoulides and M. I. Carvalho, J. Opt. Soc. Am. B**12**, 1628, (1995); M. Segev, M. Shih and G. C. Valley, J. Opt. Soc. Am. B **13**, 706 (1996)

(20) M. D. Iturbe-Castillo, P. A. Marquez-Aguilar, J. J. Sanchez-Mondragon, S. Stepanov and V. Vysloukh, Appl. Phys. Lett. **64**, 408 (1994)

(21) M. Shih, M. Segev, G. C. Valley, G. Salamo, B. Crosignani and P. DiPorto, Elect. Lett. **31**, 826 (1995); Opt. Lett. **21**, 324 (1996)

(22) D. Kip, M. Wesner, V. Shandarov and P. Moretti, Opt. Lett. **23**, 921 (1998); D. Kip, E. Kratzig, V. Shandarov and P. Moretti, Opt. Lett. **23**, 343 (1998).

(23) Y. N. Karamzin, A. P. Sukhorukov, Sov. Phys. JETP **41**, 414 (1976)

(24) W. E. Torruellas, Z. Wang, D. J. Hagan, E. W. Van Stryland, G. I. Stegeman, L. Torner and C. R. Menyuk, Phys. Rev. Lett. **74**, 5036 (1995); R. Schiek, Y. Baek and G. I. Stegeman, Phys. Rev. A **53**, 1138, (1996)

(25) R.A. Fuerst, M.T.G. Canva, D. Baboiu and G.I. Stegeman, Opt. Lett., **22**, 1748 (1997); P. Di Trapani, G. Valiulis, W. Chinaglia and A. Adreoni, Phys. Rev. Lett., **80**, 265 (1998)

(26) To be more precise, all nonlinearities are actually non-instantaneous, because even in the fastest nonlinear medium possible (say, a non-resonant electronic transition in atoms) the shortest response time is the dephasing time (or the life time, for real energy levels).

(27) M. Mitchell, Z. Chen, M. Shih and M. Segev, Phys. Rev. Lett. **77**, 490 (1996); Z. Chen, M. Mitchell, M. Segev, T. Coskun and D. N. Christodoulides, Science **280**, 889 (1998).

(28) M. Mitchell and M. Segev, Nature, **387**, 880 (1997)

(29) M. Soljačić and M. Segev, *Self-Trapping of "Necklace-Ring" Beams in Self-Focusing Kerr Media*, submitted for publication in Phys. Rev. E

(30) M. Soljačić and M. Segev, *Integer and Fractional Angular Momentum Borne on Self-Trapped Necklace-Ring Beams*, submitted for publication in Phys. Rev. Lett.

(31) Marin Soljačić, Mordechai Segev, and Curtis R. Menyuk. Phys. Rev. E Rapid Comm. Vol. **61**, 1048, (2000).

(32) Suzanne Sears, Marin Soljačić, Mordechai Segev, Dmitriy Krylov, and Keren Bergman, Phys. Rev. Lett. **84**, 1902, (2000).

(33) Marin Soljačić, Mordechai Segev, Tamer Coskun, Demetrios N. Christodoulides, and Ashvin Vishwanath. Phys. Rev. Lett. **84**, 467, (2000).

(34) A. Barthelemy, C. Froehly and M. Shalaby, SPIE **2041**, 104-113 (1993).

(35) See, e.g., N. N. Akhmediev, Opt. and Quant. Elect. **30**, 535 (1998) and references therein.

(36) V.E. Zakharov and A. M. Rubenchik, Sov. Phys. JETP **38,** 494 (1974).

(37) H. A. Haus, Appl. Phys. Lett. **8**, 128 (1966).

(38) A. Hasegawa and F. Tappert, Appl. Phys. Lett. **23**, 142 (1973); L. F. Mollenauer, R. H. Stolen and J. P. Gordon, Phys. Rev. Lett. **45**, 1095 (1980).

(39) V. V. Afanasjev, Phys. Rev. E **52**, 3153 (1995).

(40) Azimuthal modulation instability of uniform bright ring beams (carrying zero topological charge) in self-focusing Kerr media was demonstrated theoretically by Y. Chen and A. W. Snyder, Elect. Lett. 27, 565 (1992); Y. Chen, IEEE J. Quant. Elect. QE-26, 1236 (1991). To our knowledge, this instability has not yet been observed experimentally in Kerr media. Uniform bright ring beams with zero topological charge are azimuthally unstable also in saturable self-focusing media as shown theoretically by J. Atai, Y. Chen and J. M. Soto-Crespo, Phys. Rev. A **49**, R3170 (1994).

(41) Azimuthal modulation instability of bright ring beams that carry non-zero topological charge, in self-focusing (Kerr and non-Kerr) media was demonstrated theoretically by several groups, including V. I. Kruglov, Y. A. Logvin and V. M. Volkov, J. Mod. Opt. **39**, 2277 (1992); W. J. Firth and D. V. Skryabin, Phys. Rev. Lett. **79**, 2450 (1997); L. Torner and D. V. Petrov, Elect. Lett. **33**, 608 (1997); J. Opt. Soc. Am. B **14**, 2017 (1997), and others. The vortex-ring beam disintegrates into multiple **isolated** filaments. In Kerr media, the isolated filaments are of course unstable. In saturable self-focusing media, the filaments are stable and can interact with one another (if they are close enough to each other) or simply move outwards like free particles. Experimentally, disintegration of vortex-ring beams in saturable self-focusing media was observed by V. Tikhonenko, J. Christou, and B. Luther-Davies, Phys. Rev. Lett. **76**, 2698 (1996); J. Opt. Soc. Am. **12**, 2046 (1995) in atomic vapor and by Z. Chen, M. Shih, M. Segev, D. W. Wilson, R. E. Muller and P. D. Maker, Opt. Lett. **22**, 1751, (1997) in photorefractives. To our knowledge, the disintegration of vortex-ring beams in self-focusing Kerr media was not observed experimentally yet.

(42) D. J. Mitchell, A. W. Snyder, and L. Poladian, Phys. Rev. Lett. **77**, 271 (1996).

(43) L. D. Landau and E. M. Lifshitz, *Electrodynamics of Continuous Mediua*, 2rd Ed., Chap. XIII, pp. 382, (Publishers: Butterworth-Heinenann, Oxford, 1982).

(44) Interestingly, in our simulations, we never find a non-expanding necklace that remains stable forever; we were able to adjust and optimize the necklace parameters so that it is non-expanding and remains stable for a longer distance, but such fine-tuning is most probably beyond experimental relevance. What we show in Figure 2.6-7 is an example where the fine tuning is within reasonable experimental reach.

(45) Mathematically speaking, it has been long established that (2+1)D cylindrically-symmetric beams are unstable in media in which their propagation dynamics is represented by the scalar (2+1)D cubic NLSE, and undergo catastrophic collapse above a specific power threshold. See, e.g. [35]. In reality, however, when the beam becomes narrow enough (during its collapse), it can no longer be represented by a scalar equation. In the last few years several authors have argued that the vectorial nature of the propagation arrests the collapse. In this chapter we do not discuss such cases: we investigate paraxial beams only for which all the physics in contained in the scalar (2+1)D cubic self-focusing NLSE.

(46) G. A. Swartzlander and C. T. Law, Phys. Rev. Lett. **69**, 2503 (1992); B. Luther-Davies, R. Powels, and V. Tikhonenko, Opt. Lett. **19**, 1816 (1994); Z. Chen, M. Segev, D. W. Wilson, R. E. Muller and P. D. Maker, Phys. Rev. Lett. **78**, 2948 (1997).

(47) M. Shih, M. Segev and G. Salamo, Phys. Rev. Lett. **78**, 2551 (1997).

(48) Z. Musslimani, M. Segev, D. N. Christodoulides and M. Soljačić, Phys. Rev. Lett. **84**, 1164 (2000).

(49) J. P. Torres, J. M. Soto-Crespo, L. Torner, and D. V. Petrov, Opt. Comm. **149**, 77 (1998); G. Molina-Terriza, J. P. Torres, L. Torner, and J. M. Soto-Crespo, Opt. Comm. **158**, 170 (1998).

(50) M. Quiroga-Teixeiro and H. Michinel, J. Opt. Soc. Am. B **14**, 2004 (1997).

(51) R. A. Beth, Phys. Rev. **50**, 115 (1936); T. W. Hansch and A. L. Schawlow, Opt. Comm. **13**, 68 (1975); A. Ashkin, Science 210, 1081 (1980); H. He, M. E. J. Friese, N. R. Heckenberg, and H. Rubinsztein-Dunlop, Phys. Rev. Lett. **75**, 826 (1995).

(52) L. Allen, M. W. Beijersbergen, R. J. C. Spreeuw, and J. P. Woerdman, Phys. Rev. A **45**, 8185 (1992). These authors actually derived the angular momentum per-photon in a Laguerre-Gauss shaped beam only, and found that it is an integer multiple of $\hbar$. However, if one takes $u(r,\theta)=f(r)\exp(iM\theta)$ with an arbitrary $f(r)$, and use Eq. (6) in Allen's paper, and the expressions for physical linear, and physical angular momentum carried by light, it trivially follows that the ratio of the angular to the linear momentum is $M\lambda/2\pi$. Since the linear momentum per photon is h/λ, it follows that the angular momentum per photon is $M\hbar$.

(53) In fact, in self-defocusing Kerr media the only stable vortex solitons are those with $M=\pm1$. Multiply charged vortex solitons (for which M is still an integer different than ±1) are unstable, although the instability can be suppressed by saturation of the nonlinearity. See A. Dreischuh, G. G. Paulus, F. Zacher, F. Grasbon, H. Walther, Phys. Rev. E **60**, 6111 (1999).

(54) It is important to note that $f(r)$ goes at least as fast as r^2 close to the origin, so no singularities appear when this ψ is substituted into the NLSE.

(55) That is, the expectation value of the angular momentum of each photon, around the center of the necklace is the same, no matter where the photon is in the necklace.

(56) The diffraction length, L_D, equals 1 normalized unit. If the non-linearity is turned "off" in Eq. (3.1-1), then a gaussian beam of $\psi(x,z=0)=\exp(-x^2/2)$ expands its FWHM by a factor of $\sqrt{2}$ within $1L_D$.

(57) L. P. Kadanoff, Fractals: where's the physics? Phys. Today, **39**, pp. 6-7, 1986.

(58) P. S. Addison, Fractals and Chaos, Institute of Physics, Bristol, 1997.

(59) M. V. Berry and S. Klein, J. Mod. Opt. **43**, 2139 (1996).

(60) G. P. Karman and J. P. Woerdman, Opt. Lett. **23**, 1909 (1998).

(61) G. P. Agrawal, Chap. 2 in *Contemporary Nonlinear Optics*, G. P. Agrawal and R. W. Boyd Ed., Academic Press, San Diego, 1992.

(62) We use the term "soliton" in conjunction with self-trapped wave-packets, i.e., the broader definition of solitons that includes these in non-integrable systems, as spelled out first by J. S. Russell in 1834 and recently by Zakharov V. E., and Malomed B. A., in *Physical Encyclopedia,* Prokhorov A. M., Ed., Great Russian Encyclopedia, Moscow, 1994.

(63) Marin Soljačić, Suzanne Sears, Mordechai Segev, Dmitry Krylov, and Keren Bergman, Photonics Science News, **5**, Issue 1, (1999).

(64) P. Winternitz, *Partially integrable evolution equations in physics*, R. Conte and N. Boccara Ed., Kluwer, Dordrecht, 1990; A. M. Ablowitz and P. A. Clarkson, *Solitons, Nonlinear Evolution Equations, and Inverse Scattering*, Cambridge University Press, Cambridge, UK, 1991.

(65) The term "Soliton existence curve" was coined for photorefractive screening solitons [M. Segev, M. Shih and G. C. Valley, J. Opt. Soc. Am. B **13**, 706 (1996)], but it is universal and applies to all solitons.

(66) V. Tikhonenko, J. Christou, and B. Luther-Davies, Phys. Rev. Lett. **76**, 2698 (1996)

(67) E. DelRe, M. Tamburrini, M. Segev, A. Agranat and R. Della Pergola, Phys. Rev. Lett. **83**, 1954 (1999).

(68) V. I. Bespalov and V. I. Talanov, JETP Lett. **3**, 307 (1966); V. I. Karpman, JETP Lett. **6**, 277 (1967); G. P. Agrawal, Phys. Rev. Lett. **59**, 880 (1987); S. Wabnitz, Phys. Rev. A 38,

2018 (1988); For a review see G. P. Agrawal, *Nonlinear Fiber Optics,* Second Ed. (Academic Press, San Diego, 1995), Chap. 5 and references therein.

(69) E. M. Dianov et al., Opt. Lett. **14**, 1008 (1989); P. V. Mamyshev et al., J. Opt. Soc. Am. B **11**, 1254 (1994); M. D. Iturbe-Castillo et al., Opt. Lett. **20**, 1853 (1995); M. I. Carvalho, S. R. Singh, and D. N. Christodoulides, Opt. Comm. **126**, 167 (1996).

(70) D. N. Christodoulides et al., Phys. Rev. Lett. **78**, 646 (1997); ibid **80**, 2310 (1998).

(71) M. Mitchell et al., Phys. Rev. Lett. **79**, 4990 (1997); ibid **80**, 5113 (1998).

(72) A. W. Snyder and D. J. Mitchell, Phys. Rev. Lett. **80**, 1422 (1998).

(73) V. V. Shkunov and D. Z. Anderson, Phys. Rev. Lett. **81**, 2683 (1998).

(74) N. Akhmediev, W. Krolikowski and A. W. Snyder, Phys. Rev. Lett. **81**, 4632 (1998).

(75) A. Hasegawa and W. F. Brinkman, J. Quant. Elect. **16**, 694 (1980); K. Tai, A. Hasegawa and A. Tomita, Phys. Rev. Lett. **56**, 135 (1981).

(76) Detlef Kip et. al. to be submitted to Phys. Rev. Lett.

(77) e.g., G. B. Whitham, Proc. Roy. Soc. **283**, 238 (1965) and T. B. Benjamin and J. E. Feir, J. Fluid Mech. **27**, 417 (1967) for MI in fluids; T. Taniuti and H. Washimi, Phys. Rev. Lett. **21**, 209 (1968), and C. K. W. Tam, Phys. Fluids **12**, 1028 (1969), and A. Hasegawa, Phys. Rev. Lett. **24**, 1165 (1970) for MI in plasma physics.

(78) A. Hasegawa, Opt. Lett. **5**, 416 (1980).

(79) A. Hasegawa, Phys. Fluids **18**, 77 (1975); **20**, 2155 (1977).

(80) S. E. Harris, and L. V. Hau, Phys. Rev. Lett. **82**, 4611 (1999).

(81) D.Krylov, L.Leng, K.Bergman, J.C.Bronski, and J.N.Kutz, Opt. Lett. **24**, 1191 (1999).